Retrieval of Atmospheric Water Vapor Content in Polar Regions Using Spaceborne Microwave Radiometry

Bestimmung des atmosphärischen Wasserdampfgehaltes in Polargebieten mit Hilfe der passiven Mikrowellenradiometrie

---

Jungang Miao

Ber. Polarforsch. 289 (1998)
ISSN 0176 - 5027

Jungang Miao
Institut für Umweltphysik
Universität Bremen, FB 1
Kufsteiner Straße
D-28359 Bremen

email : jungang@diana.physik.uni-bremen.de

Die vorliegende Arbeit ist die inhaltlich unveränderte Fassung einer Dissertation, die im Mai 1998 dem Fachbereich Physik/Elektrotechnik der Universität Bremen vorgelegt wurde.

Contents

Acknowledgments

The works presented in this report were done at the Institute of Environmental Physics, University of Bremen, from 1994 to 1998. Through these years I have been always accompanied by friendly help and encouragement from many people, to whom I am deeply indebted. First of all, I would like to express my sincere gratitude to my supervisor, Prof. Dr. K. Künzi, for offering me the valuable opportunity to further my study in the fascinating area of microwave remote sensing; his deep solicitude both to my research and to my life is strongly impressed on my memory. My sincere gratitude goes also to our group head, Dr. Georg Heygster, whose honesty, patience and enthusiasm minimized the difficulties I encountered in Germany.

I would also like to acknowledge all the members in the Group of Geophysical Analysis of Satellite Image, in particular, Dr. Thomas Hunewinkel, Klaus-Peter Johnsen, Britta Klocke, Norbert Schlüter, Dr. Ralf Schmidt, Dr. Christian Thomas. I have got much benefit from their suggestions and comments during these years. I will never forget that Dr. Barbara A. Burns and Dr. Thorsten Markus, formerly colleagues of mine, gave me the initial help and guidance as I arrived at Bremen a few years ago. I would specially like to express my thanks to them.

Last but not least, I thank the University of Bremen for generously granting me a scholarship in the past three and a half years. Without this financial support this dissertation would not have been possible.

Abstract

The concern on the possibly adverse effects of global warming has made monitoring the Earth environment a high priority item. Satellites have been widely used since the 60's to measure atmospheric parameters from space. Over open oceans, the atmospheric water vapor content has been successfully measured using passive microwave radiometry. However, this measurement was limited to the non polar regions. The difficulties encountered in polar regions arise from the very low water vapor burden of the atmosphere and from the highly variable surface conditions of polar ice. It is the goal of this thesis to improve this situation by carefully investigating the information content of the Special Sensor Microwave/Water Vapor (SSM/T2), which is part of the United States Defense Meteorological Satellite Program (DMSP). SSM/T2 has three channels located on the wing of the strong water vapor absorption line at 183.31 GHz and is therefore very sensitive to water vapor. In addition, the center frequencies of these channels are close enough, so that the polar ice shows nearly the same emission properties at all these channels. On the contrary, these channels have quite different sensitivities to water vapor, therefore it appears possible to extract information on tropospheric water vapor.

After an introductory overview in Chapter 1 on satellite remote sensing of tropospheric water vapor, Chapter 2 describes the theoretical rationale of the proposed method in detail. A new quantity, the Ratio of Compensated Brightness Temperature Differences (RCBTD), is defined. Based on the general radiative transfer equation for a non-scattering atmosphere, the relation between the RCBTD and the Total Water Vapor (TWV) in the atmosphere is shown to be nearly independent of ground surface emission. This conclusion is confirmed by simulations performed using a radiative transfer model. This relationship is then used to retrieve the atmospheric water vapor content over Antarctica. For this purpose, the basic emission properties of Antarctic sea and land ice need to be considered. Since there are no *in situ* measurements in Antarctica at SSM/T2 frequencies, surface parameters of Antarctic ice are estimated in Chapter 3 based on data from spaceborne microwave and infrared sensors. The surface emissivities of Antarctic sea and land ice in austral winter are found to be within the range of $0.65 \cdots 0.90$, with an average of about 0.80 at frequencies near 150 GHz. In Chapter 4, an algorithm is developed based on radiosondes and validated using an independent set of radiosondes. In a next step, mean water vapor is determined using the RCBTD algorithm for 16 stations in Antarctica and found to agree reasonably well with the water vapor averages from corresponding radiosondes. At 9 of the 16 stations the relative differences between SSM/T2 and radiosondes are less than 20%. The effect of clouds has been estimated using an existing radiative transfer model which includes scattering. From this analysis it is concluded that water clouds do not appreciably influence the water vapor retrieval accuracy based on the RCBTD algorithm but ice clouds are more critical. Using this algorithm, it is now possible to determine water vapor distribution over the entire Antarctic continent on a daily basis from SSM/T2 data. Finally in the last chapter, features of the Antarctic water vapor distribution are analyzed based on the daily averaged TWV images retrieved from SSM/T2 data.

Chapter 1

Introduction

1.1 Water Vapor in the Atmosphere

The climate of the Earth is able to support life in large part because of the atmospheric greenhouse effect and the workings of the hydrological cycle. Water vapor, water in the gaseous phase, is a key element in both of these. In the hydrological cycle, the water vapor moves quickly through the atmosphere and redistributes energy associated with its evaporation and recondensation, and this movement is strongly coupled with precipitation and soil moisture, which have important practical implications. There are many greenhouse gases in the atmosphere, some naturally occurring and some resulting from industrial activities, and the most important one is water vapor. Water vapor is involved in an important climate feedback loop. As the temperature of the Earth's surface and atmosphere increases, the atmosphere is able to hold more water vapor. The additional water vapor, acting as a greenhouse gas, absorbs energy that would otherwise escape to space and so causes further warming. This basic picture is complicated by important interactions between water vapor, clouds, atmospheric motion, and radiation from both the Sun and the Earth.

Compared with its active role at the low and middle latitude, water vapor is relatively passive in the dynamics of the polar atmosphere, due to the low temperatures which prevails. However, there are some physical processes in which water vapor is very important. The surface latent heat fluxes over the Antarctic oceans appears to play a major role in the energetics of some mesoscale weather systems and water vapor exerts a major control on the regional energy budget through cloud formation and other radiative effects (*King and Turner*, 1997). The sea ice cover can have profound influences on the state of the atmosphere and ocean, primarily by altering the surface heat exchange. The sea ice coverage variability involves the interactions within the complete physical system— atmosphere-ocean-ice. In this system, the surface radiation budget is an important factor that is significantly modulated by the clouds, aerosols, and water vapor. In evaluating the surface radiation budget, the uncertainty in water vapor amount is one of the main error sources (*Key et al.*, 1997). Moreover, atmospheric water vapor is the source of all the ice in the continental ice sheets through precipitation. The fluctuation of precipitation over these ice sheets, especially over Antarctica, is a potentially important contributor to variations in global sea level (*Bromwich*, 1990). The transport of water vapor into and within the Antarctic atmosphere is essential to the precipitation over Antarctica, and therefore, to the mass balance of the Antarctic ice sheet. This study is hampered by the scarcity of measurements of water vapor in polar regions in both temporal and spatial scales (*Giovinetto et al.*, 1997; *Connolley and King*, 1993). It remains open, whether the ice sheets are growing or shrinking (*King and Turner*, 1997).

1.2 Remote Sensing of Tropospheric Water Vapor

Nowadays a multitude of systems exist for observing water vapor. Each has its own characteristics and advantages. Figure 1.1 shows some different types of observational systems.

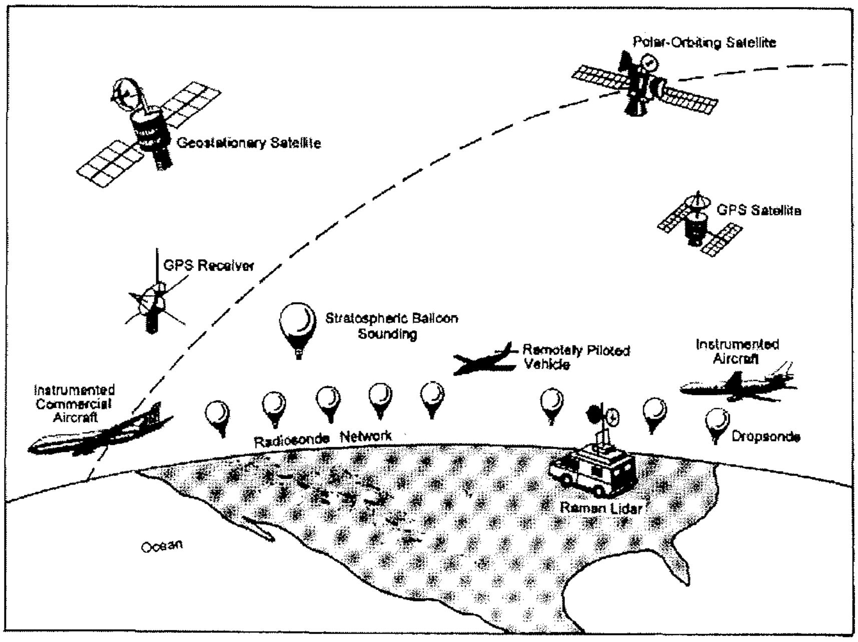

Figure 1.1: *Some different types of ground- or space-based systems for observing water vapor. Note, the ground-based microwave radiometer is not shown. (From AGU, 1995)*

Routine measurements of water vapor abundance are made by hygrometers on the ground and in radiosondes. These are direct *in situ* measurements that are quite accurate at relatively high temperature and vapor abundance. However, there are several shortcomings of these observations. (1) Current instrument sensitivity significantly reduces the reliability of measurements of water vapor abundance in the upper troposphere (with temperatures lower than −40° C) and consequently in a major part of polar regions. (2) Geographic coverage of radiosonde balloon launch sites is poor, particularly over oceans and at high latitudes. (3) Most sites launch only two balloons per day at synoptic reporting times, which provides neither a longitudinal consistent nor complete representation of diurnal variations of water vapor (*Rossow*, 1996). Instrumented aircraft can make measurements at almost any location and at any time desired, but they are only used for the special research missions; hence, their temporal coverage is limited.

Weather satellites, especially those in a sun-synchronous, low polar orbit and equipped with microwave radiometers, provide an important tool to remotely monitor the atmospheric water content with both good temporal and spatial coverage. The early activities of Russian scientists with the Cosmos satellites nearly three decades ago are among the first studies to utilize such measurements to infer information about the water content of the atmosphere (*Greenwald et al.*, 1993). Many other studies followed these pioneering efforts based on observations from different instruments on a variety of satellites including the Nimbus-E Microwave Spectrometer (NEMS) on the Nimbus-5 spacecraft (e.g. *Grody*, 1976; *Staelin et al.*, 1976; *Chang and Wilheit*, 1979), the Scanning Microwave Spectrometer (SCAMS) aboard the Nimbus-6 satellite (e.g. *Rosenkrantz et al.*, 1978), and the Special Multichannel Microwave Radiometer (SMMR) on the Nimbus-7 and Seasat satellites (e.g. *Prabhakhara et al.*, 1982; *Curry et al.*, 1990).

Nowadays, the widely used microwave instrument for atmospheric total water vapor (TWV) retrieval is the Special Sensor Microwave/Imager (SSM/I), which is aboard the Defense Meteorological Satellite Program (DMSP) satellites since June 1987. This instrument is a passive microwave radiometer and has seven channels measuring both vertically and horizontally polarized radiation at 19.35, 37, and 85.5 GHz and only vertically polarized radiation at 22.235 GHz. The latter is situated on the peak of a weak water vapor absorption line and therefore is the main source of information for retrieving water vapor. Many of the proposed algorithms for SSM/I made use of this 22.235 GHz channel, with the inclusion of other channels for the correction of the cloud liquid water influences and, to some extent, the influences of surface wind. The algorithm of *Liu et al.* [1992] is a physically based retrieval, in which the SSM/I measurements are matched to a radiative transfer model. The statistical algorithms are normally developed using multiple regressions. *Alishouse et al.* [1990] and *Schluessel and Emery* [1990] developed their algorithms using satellite measurements of SSM/I, while *Bauer and Schluessel* [1993] and *Simmer* [1994] used model-derived responses. Statistical algorithms have the advantage of simplicity, but they are inevitably characterized by the data set used. In applying them, the rain contaminated pixels must be screened out beforehand. In the cases of heavy clouds caution must be taken, although the cloud contaminated measurements or responses from model are indeed included in the development of these algorithms (*Fuhrhop and Ruprecht*, 1995). In general, the algorithms using the 22.235 GHz channel suffer from the fact that this channel begins to run into saturation when the total columnar water vapor is greater than 30 kg/m^2 (*Schluessel and Emery*, 1990). To lessen this effect, *Tjemkes et al.* [1991] developed an algorithm that used the 19.35 GHz channel only. This algorithm does a better job for moist atmospheres, but it systematically overestimates the TWV in the dry atmosphere and shows greater sensitivity to surface emissivity changes. Recently, neural networks are used for TWV retrieval and reported to do a better job than the regression algorithms (*Ruprecht and Jung*, 1997).

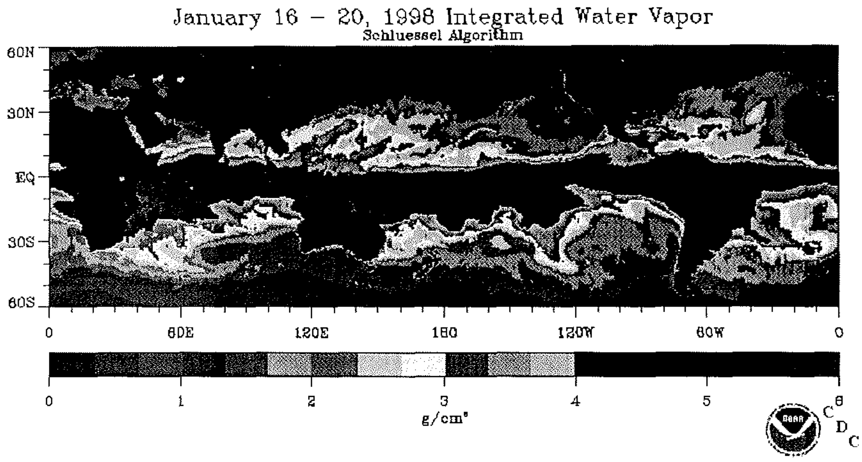

Figure 1.2: *An example of the global TWV image, retrieved using the Schluessel and Emery algorithm. (From the archive of satellite climate products of Satellite Climate Research, NOAA)*

In Figure 1.2 a global TWV image is shown, which is obtained from SSM/I measurements and used nowadays for climate research. It is noticed that the retrieval was done only over ice-free oceans at latitudes less than 60°. The reason is that the algorithms developed for SSM/I are exclusively for ice-free oceans, since at SSM/I frequencies the open ocean forms a cold and homogeneous background against which the atmospheric parameters can be easily distinguished. Over land and ice-covered ocean the large and highly variable surface emissivities make the TWV retrieval from SSM/I data a much more difficult job. Even over the ice-free circumpolar ocean the retrieval errors are expected to be much larger than over tropical and mid-latitude oceans, as a result of the low water vapor burden.

Although there are improvements in water vapor measurements becoming available to the community, however, none of these satellite systems does a thorough job in measuring the vertical profiles of water vapor from the ground surface up into the lower stratosphere over both ocean and land in clear and cloudy conditions with enough time and space resolution. The high-resolution infrared radiation sounder (HIRS) on board the NOAA-POES series satellites has provided an operational estimate of water vapor profiles since 1979, but the analysis has been done only for cloud-free conditions and both its accuracy (20-30%) and its vertical resolution (3 layers) are poor (*Chedin et al.*, 1993). The polar regions, with unique climate conditions, including widespread surface temperature inversions, long lasting cloud cover, and extended periods of darkness, present unique retrieval problems for HIRS (*TOVS*, 1995). Even though NOAA has generally operated two polar orbiters, the analyzed dataset does not provide measurements more frequently than about once per day (*Rossow*, 1996). Hence, satellite water vapor measurements by HIRS have only improved the geographic and not the temporal coverage.

In November of 1991 the Special Sensor Microwave/Water Vapor (SSM/T2) was launched aboard the DMSP satellite F-11. This was the first operational spaceborne passive microwave radiometer designed to work near the water vapor absorption line at 183.31 GHz. SSM/T2 has the potential to allow global monitoring of water vapor in the atmosphere under most meteorological conditions over land and ocean. In fact, studies on atmospheric water vapor retrieval using this strong absorption line began long before the flight of SMM/T2 (e.g. *Schaerer and Wilheit*, 1979; *Kakar*, 1983; *Wang et al.*, 1983). These studies include both numerical simulations and experimental observations with airborne instruments, and a number of retrieval algorithm have been proposed. The physical algorithms of *Wang and Chang* [1990] and of *Wilheit* [1990] were reported to be able to cope with cloudy situations; *Kuo et al.* [1994] claimed that their statistical and physical iterative scheme is more robust near isothermal and temperature inversion than others; *Cabrera-Mercader and Staelin* [1995] even tried to use neural network for humidity profile retrieval. But, none of these algorithms has shown so superior results that it could replace a simple statistical scheme for operational analyses of SSM/T2 data (*Aerojet*, 1987; *T. Reale, NESDIS, NOAA, Private Communication*, 1998). Recently, research has concentrated on algorithm validation through comparisons of retrieved results with other measurements, such as radiosonde and Raman lidar (*Wang et al.*, 1993; *Wang et al.*, 1995; *Wang et al.*, 1997a; *Wang et al.*, 1997b) and on improving the retrieval scheme through synergy with other sensors, *e.g.* AVHRR (*Wilheit and Hutchison*, 1997).

Like for infrared sounder, the polar regions are a severe challenge to the microwave sounder, too. The problems originate from the low, but highly variable, water vapor burden in the polar atmospheres. On the one hand, the low water vapor content renders a significant contribution of ground surface emissions to the radiance received by a spaceborne radiometer, which is difficult to remove due to the large spatial variation of the surface temperature and the frequency dependence of the emissivities of ice; on the other hand, its wide range of variation makes the responses of SSM/T2 channels to be nonlinear. When the atmospheric water vapor burden is low, the measured radiances generally increase with increasing water vapor content, whereas for an opaque atmosphere the measured radiance decreases by adding more water vapor in the atmosphere. For the three channels on the 183.31 GHz line, both thin and opaque atmospheres are within the natural variability in the polar regions, since the water vapor burden there ranges from a few decimal kg/m^2 to about 10 kg/m^2. Hence, a linear algorithm can not cope with this behavior and even a nonlinear algorithm could fail to converge if the first guess is far off (*Wilheit and Hutchison*, 1997).

To make up for the deficiency of satellite measurements of water vapor, a method to retrieve the total water vapor over ice-covered polar regions using the SSM/T2 is proposed here. The retrieval using this method is almost independent of the surface

Table 1.1: System Characteristics of SSM/T2

Channel	1	2	3	4	5
Center Frequency (GHz)	91.655 ± 1.25	150.0 ± 1.25	$f_c^* \pm 7$	$f_c \pm 3$	$f_c \pm 1$
IF Bandwidth (GHz)	1.5	1.5	1.5	1.0	0.5
NET (K)	0.6	0.6	0.6	0.6	0.8
Calibration Accuracy (K)	1.5	1.5	1.5	1.5	1.5
Antenna 3-db Beamwinth (°)	6.0	3.7	3.0	3.0	3.0
Resolution at Nadir (km)	88	54	48	48	48

$*$: f_c equals 183.310 GHz

emissivity and surface temperature changes, and is useful in the polar meteorological and climatological studies, for example, the precipitation variability over Antarctic plateau.

Before further discussing the method, we summarize the system characteristics of SSM/T2, which will be used as a background information in the following chapters.

1.3 System Characteristics of SSM/T2

The water vapor sounder, SSM/T2, is part of the DMSP Block 5D-2 satellite payload, first launched on F-11 in 1991. The followed spacecrafts F-12 (in orbit since August 1994) and F-14 (in orbit since April 1997) are also equipped with this instrument.

The SSM/T2 is a five channel, total power, microwave radiometer with three channels situated symmetrically about the 183.31 GHz water vapor resonance line and with two window channels, near 150 and 91 GHz, respectively. The numbering and center frequencies of SSM/T2 channels, as well as the related system characteristics are given in Table 1.1. All channels are designed as double sideband receivers. The in-flight calibration is performed by viewing an internal hot-load target ($\sim 300\,\mathrm{K}$) and the cosmic background radiation ($\sim 3\,\mathrm{K}$) four times during each scan period. The achieved nominal Noise Equivalent Delta Temperature (NET) and the maximum error of calibration for all channels are 0.6 K and 1.5 K per pixel respectively, except for channel 5, whose nominal NET is 0.8 K.

The SSM/T2 employs a single offset parabolic reflector with a 6.6 centimeter diameter projected aperture and a single multifrequency feedhorn to achieve a 3.3° beamwidth for the 183.31 GHz channels and larger beamwidths of approximately 3.7° and 6.0° for 150 and 91 GHz, respectively. To perform the cross-track scanning, the reflector rotates while the feedhorn remains fixed. This results in changing footprint sizes and rotating polarisation states (*Aerojet*, 1990), as shown in Figure 1.3(a). SSM/T2 performs 28 observations (pixels) per scan for each of the five channels, corresponding to the satellite scan angle of ±40.5°. The 3-dB contours (footprint) of the antenna beam projected on the Earth surface for 183.31 GHz channels are approximately 48×48 km^2 at nadir and 98×66 km^2 at the edge of scan. All

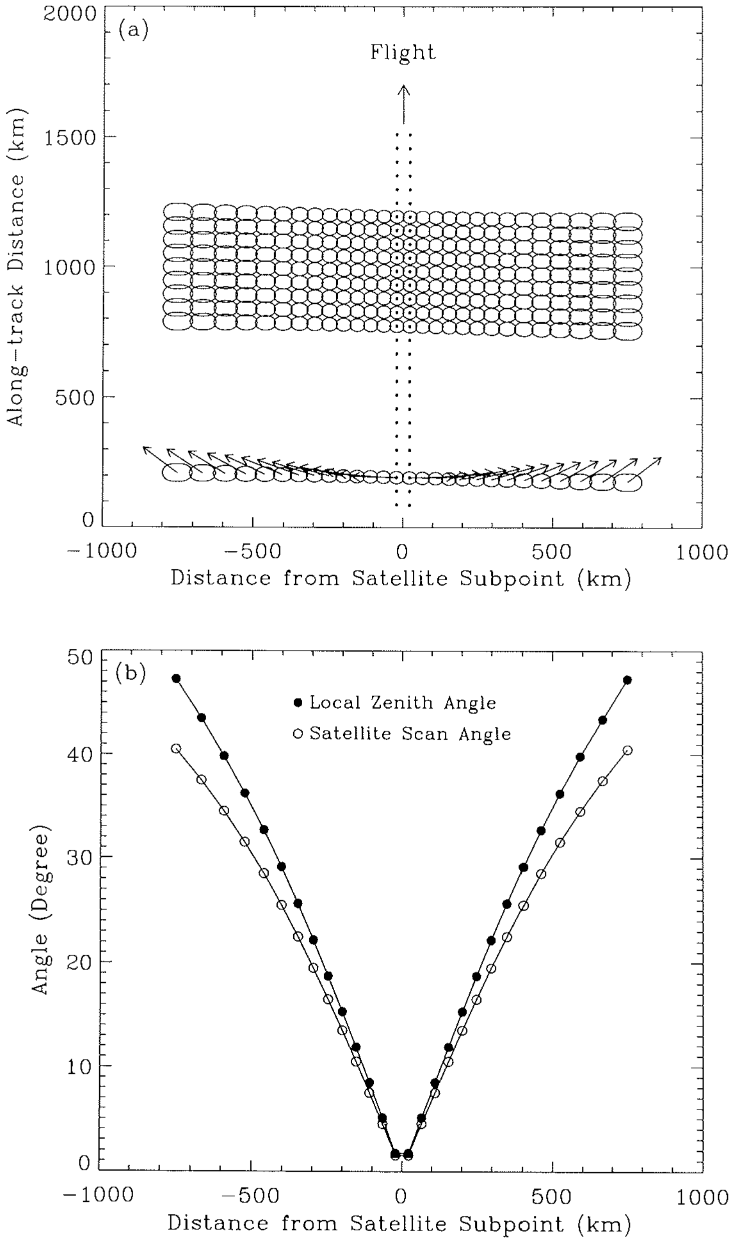

Figure 1.3: *(a) The footprints of SSM/T2 at its 183.31 GHz channels and the polarization directions (arrows) of the received radiances for each footprint, as projected on the Earth surface. (b) the satellite scan angle and the local zenith angle corresponding to each footprint.*

five channels have coincident centers. The total swath width for the SSM/T2 is approximately 1500 km.

At each beam position, all SSM/T2 channels receive the radiance at the same polarization state that changes as the antenna scans, as shown in Figure 1.3(a). If Θ represents the satellite scan angle and θ represents the local zenith angle (see Figure 1.3(b)), then the equivalent SSM/T2 surface emissivity ϵ_s is expressed as a linear combination of two orthogonal components, *i.e.*

$$\epsilon_s = \epsilon_v(\theta)\cos^2(\Theta) + \epsilon_h(\theta)\sin^2(\Theta) \tag{1.1}$$

where ϵ_v and ϵ_h represent the vertically and horizontally polarized surface emissivities, respectively (*Felde and Pickle*, 1995). This equation shows that the polarization is vertical, when SSM/T2 views the Earth surface in the nadir direction.

Chapter 2

Method of Total Water Vapor Retrieval

In this chapter, a method for total atmospheric water vapor retrieval using SSM/T2 is proposed. In order to better explain it, the physical backgrounds of remote sensing technique is reviewed at first. Then, the detailed derivation of the method is described based on the radiative transfer equation for non-scattering atmospheres; the method is then further demonstrated by model simulations. The influences of the atmospheric vertical structure on the retrieval accuracy of the proposed method are discussed qualitatively in the last section.

2.1 Backgrounds

2.1.1 The Interaction between the Atmosphere and Microwaves

The interaction between atmospheric constituents (gases, aerosols, and hydrometers) and electromagnetic waves is the physical basis to remotely sense atmospheric parameters. For the measurements of tropospheric water vapor with passive microwave radiometry, the absorption of oxygen (O_2) has to be considered, in addition to water vapor (H_2O). However, the effects of aerosols and other trace gases, e.g. CO, O_3, are usually negligible. Hydrometeors (liquid or frozen water particles either suspended or falling in the atmosphere) affect the propagation of microwaves by both absorbing and scattering of radiation. Detailed discussion of these mechanisms can be found in *e.g. Gasiewski* [1993].

Macroscopically, the atmosphere can be considered as an inhomogeneous, isotropic, linear and lossy dielectric. Its effect on the propagation of electromagnetic waves is characterized by the complex refractive index, n, with the definition of

$$n = \sqrt{\varepsilon_r} \tag{2.1}$$

where ε_r is the complex relative permittivity of the atmosphere and defined as

$$\varepsilon_r = \varepsilon/\varepsilon_0 = \varepsilon_r' + j\varepsilon_r'' \tag{2.2}$$

in which ε is the complex permittivity of the atmosphere; ε_0 is the permittivity of vacuum; ε_r' and ε_r'' are the real and imaginary parts of ε_r respectively. If a plane wave has traveled a distance d in the atmosphere, the electric field vector of the wave can be written as

$$\vec{E}(z) = \vec{E}(0)e^{jk_0dn} \tag{2.3}$$

where $\vec{E}(0)$ is the initial vector of the electric field, $k_0 = 2\pi f/c$ is the free space wave number, f is the frequency, and c is the speed of light in vacuum. If the complex form of n

$$n = n' + jn'' \tag{2.4}$$

is substituted into Eq.(2.3), we obtain

$$\vec{E}(z) = \vec{E}(0)e^{-k_0dn''}e^{jk_0dn'} \tag{2.5}$$

Usually, n' and n'' are frequency dependent; hence the atmosphere is both dispersive (through n') and absorptive (through n'') to electromagnetic waves. The quantity n' is very close to 1, and n'' is normally small but can be large near the absorption lines of water vapor and oxygen, as can be seen in Figure 2.1. Here, the specific attenuation α represents the attenuation the wave encountered in a unit length of propagations and is expressed as

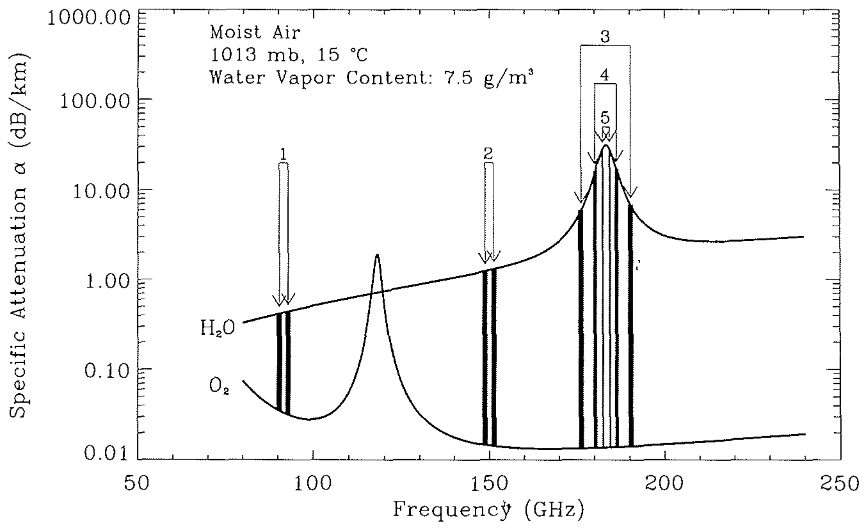

Figure 2.1: *The specific attenuation of air in the frequency range of 80–240 GHz, in which the main absorption lines are the one of water vapor at 183.31 GHz and the one of oxygen at 118.75 GHz. The shaded areas show the passbands of SSM/T2 channels, whose numbers are above the pairs of arrows. The specific attenuations are calculated using the CCIR model.*

$$\alpha = 8.68k_0n'' = 0.1820fn''. \tag{2.6}$$

In the above equation, α is in units of dB/km, where f is in Gigahertz and n'' is in parts per million.

In the microwave frequency range, *i.e.* 0.3–300 GHz, water vapor and oxygen have a number of pronounced absorption lines. In considering these absorptions, one has to take into account the fine structures of the molecules, which are related to the coupling between molecular spin and the rotation of the nuclei. The oxygen spectrum consists of a group of transitions, or absorption lines, near 60 GHz, together with a single isolated line at 118.75 GHz. These transitions arise due to the reorientation of the combined spin of two unpaired electrons, relative to the orientation of the axis of molecular rotation. In addition to these transitions are the non-resonant Debye absorption, which is important at frequencies less than about 10 GHz, and the pure rotational transitions of the oxygen molecule at frequencies higher than 300 GHz. The water vapor spectrum comprises only rotational transitions and consists of a weak line at 22.235 GHz, and a much stronger line at 183.31 GHz. A continuum absorption of water vapor exists in the microwave spectrum in addition, but up to now the physical process associated with it is still not completely clear (*Brussaard and Watson*, 1995; *Buehler*, 1996; *Bauer et al.*, 1998).

Generally, the line absorptions are described by

$$\alpha_{f_0}(f) = SF(f - f_0). \tag{2.7}$$

$\alpha_{f_0}(f)$ represents the specific attenuation at frequency f, due to the resonance at f_0, with line strength S and shape function F. The line strength S depends both on the properties of the molecule and the molecular states which in turn depends on the temperature and the gas density. Line shape F is significantly modified by molecular collisions, *i.e.* pressure broadening, and by molecular thermodynamic movements, *i.e.* Doppler broadening, and for oxygen also by the magnetic field of the Earth, *i.e.* Zeeman broadening. Two of the commonly used models for calculating the specific attenuation of air are the CCIR (International Radio Consultative Committee) model (*Gibbins*, 1986) and the microwave propagation model (MPM) of *Liebe* (1989). The CCIR model uses an approximation based on the Van Vleck–Weisskopf line shapes, with coefficients adjusted to fit the results of available measurements, and has the advantage of computational efficiency. MPM determines the absorption through a line-by-line calculation and enables the calculation at any temperature, pressure and humidity.

2.1.2 Radiative Transfer in the Atmosphere

As mentioned above, when electromagnetic waves propagates in the atmosphere, both dispersion and absorption occur; if there are scatterers in the atmosphere the polarization state of the wave may change. These effects are closely related to the temperature and the density of water vapor and oxygen in the atmosphere. If a wave travels through the whole atmosphere, the changes of its amplitude, phase and polarization contain information on the atmosphere itself. If these changes can be measured, it is possible to infer atmospheric parameters through an inversion procedure. In determining the changes of the parameters that describe electromagnetic waves, another important physical process must be considered, too. According to Kirchhof's law, if the atmosphere absorbs at a particular frequency, it must also emit at that frequency. The physical process including both extinction (absorption plus loss due to scattering) and emission is described by the radiative transfer theory.

By assuming local thermodynamic equilibrium of the atmosphere, the spectral intensity $I(\vec{r}, \vec{u}_s)$ of the radiation in direction $\vec{u}_s$ at position $\vec{r}$ is given by the differential radiative transfer equation (DRTE),

$$\frac{dI(\vec{r}, \vec{u}_s)}{ds} = -(\alpha_a + \alpha_s)I(\vec{r}, \vec{u}_s) + \alpha_a B_f(\vec{r}) + \frac{\alpha_s}{4\pi}\int_{4\pi} \Phi(\vec{u}_s, \vec{u}_i)I(\vec{r}, \vec{u}_i)d\Omega_i, \qquad (2.8)$$

where the spectral intensity $I(\vec{r}, \vec{u}_s)$ is proportional to the square of the amplitude of the electric field; α_a represents the specific attenuation of the atmosphere due to the absorption of both molecules of gas and the hydrometeors; and α_s represents the specific attenuation of the atmosphere due to scattering; $B_f(\vec{r})$ is the spectral intensity of the atmospheric emission at thermodynamic temperature $T(\vec{r})$ for one of two orthogonal polarization states. Hence, the first term on the right hand side of Eq.(2.8) represents the loss of the radiation due to atmospheric extinction; the second term, in contrast, represents the gain of the radiation owing to the atmospheric emission; the third term is an integration, which is performed over all directions in order to include all of the contributions of radiations propagating originally in other directions but scattered into direction $\vec{u}_s$. The scattering phase function $\Phi(\vec{u}_s, \vec{u}_i)$ describes the portion of energy scattered from direction $\vec{u}_i$ to direction $\vec{u}_s$. For brevity, only the copolarized component is given here. Obviously, DRTE describes the conservation of energy in the process of radiative transfer in the atmosphere.

For many applications, the spectral intensity of the atmospheric emission, B_f, can be approximated with the Rayleigh-Jeans equation,

$$B_f(\vec{r}) = \frac{kf^2}{c^2}T(\vec{r}). \qquad (2.9)$$

in which k is Boltzmann's constant. Note, B_f represents the energy flux emitted from unit projected area on a layer of the atmosphere, over unit solid angle and unit frequency bandwidth. The unit of B_f is then $\mathrm{W} \cdot \mathrm{m}^{-2} \cdot \mathrm{sr}^{-1} \cdot \mathrm{Hz}^{-1}$. Because of the linear relationship between B_f and T, it is convenient to express the spectral intensity I as an equivalent "brightness temperature"

$$T_b \equiv \frac{c^2}{kf^2}I. \qquad (2.10)$$

By substituting Eqs. (2.9) and (2.10) into Eq.(2.8), the differential radiative transfer equation relating the brightness temperature T_b with the thermodynamic temperature T can be obtained as

$$\frac{dT_b(\vec{r}, \vec{u}_s)}{ds} = -(\alpha_a + \alpha_s)T_b(\vec{r}, \vec{u}_s) + \alpha_a T(\vec{r}) + \frac{\alpha_s}{4\pi}\int_{4\pi} \Phi(\vec{u}_s, \vec{u}_i)T_b(\vec{r}, \vec{u}_i)d\Omega_i. \qquad (2.11)$$

The solution of this radiative transfer equation is very involved in general and becomes even more involved when the depolarization effect is also included. Hence, numerical methods and simplifying assumptions are commonly used in practice.

A number of numerical techniques, *e.g.* Monte Carlo method, discrete ordinate method and the method of successive order of scattering (SOS), have been proposed and thereby a few module for one dimensional radiative transfer in plane parallel atmospheres have been developed (*Fuhrhop et al.*, 1997). The program package MWMOD (MicroWave MODel), developed by *Simmer* [1994], utilizes the SOS method. Using MWMOD, both brightness temperatures and weighting functions can be calculated for the spaceborne geometry with measured or artificial atmospheric profiles; clouds can be parameterized through humidity profile analysis or specified according to requirements (See Appendix).

2.2 The RCBTD Method for Total Water Vapor

2.2.1 A Simplified Integral Radiative Transfer Equation

In developing inversion algorithms, simple, nevertheless accurate enough, form of the radiative transfer equations are commonly used to interpret the radiometric measurements. Such equations can be obtained when some simplifying assumptions are made. The effects of refraction and reflection among atmospheric layers, along with the effect of the Earth curvature, are normally ignored at microwave frequencies, when the local zenith angle θ is not larger than 80° (*Brussaard and Watson*, 1995). This condition is satisfied by most spaceborne sensors. By further supposing that there are no strong scatterers like raindrops and precipitation-sized ice particles in the air, *i.e.* $\alpha_s = 0$, then Eq.(2.11) can be solved in a closed-form solution,

$$T_b(f,\theta) = T_u(f,\theta) + T_e(f,\theta)e^{-\tau_0(f)\sec\theta} + (1-\epsilon_s(f,\theta))T_d(f,\theta)e^{-\tau_0(f)\sec\theta}. \tag{2.12}$$

T_b is the brightness temperature measured by the spaceborne radiometer at the top of the atmosphere; T_u and T_d are the upwelling and downwelling radiation of the atmosphere, respectively; T_e is the ground surface emission; ϵ_s is the surface emissivity and τ_0 is the total atmospheric opacity in the nadir direction; f and θ are the frequency and the local zenith angle, respectively. T_u, T_d and T_e are expressed by the following equations,

$$\begin{aligned}
T_u(f,\theta) &= \sec\theta\int_0^H T(z)\alpha_a(f;z)e^{-\int_z^H \alpha_a(f;z)\sec\theta dz}dz && (2.13)\\
T_d(f,\theta) &= \sec\theta\int_0^H T(z)\alpha_a(f;z)e^{-\int_0^z \alpha_a(f;z)\sec\theta dz}dz + T_c e^{-\tau_0(f)\sec\theta} && (2.14)\\
T_e(f,\theta) &= \epsilon_s(f,\theta)T_s. && (2.15)
\end{aligned}$$

In the above equations, H represents the top height of the atmosphere; $\alpha_a(f;z)$ is the specific attenuation due to the atmospheric absorption at frequency f and height z; T_s is the surface skin temperature and T_c is the cosmic background brightness temperature with a value of about 3 K. Eq. (2.12) is usually called the simplified integral radiative transfer equation.

This integral radiative transfer equation can be changed into a more convenient form, if the integral expressions of $T_u(f,\theta)$ and $T_d(f,\theta)$ were carried out using the method of integration by parts (*Grody*, 1976; *Guissard and Sobieski*, 1994). The form of *Guissard and Sobieski* [1994] is used here for further discussion, which is similar to the equation for an atmosphere with constant temperature above a smooth surface, but includes corrections for the atmospheric temperature profile,

$$T_b(\theta) = m_p T_s - (T_0 - T_c)(1 - \epsilon_s)e^{-2\tau_0 \sec\theta} \tag{2.16}$$

T_0 represents the air temperature just above the ground surface; the quantity m_p is of the order of unity and given by

$$m_p = 1 + [(1 - \epsilon_s e^{-\tau_0 \sec\theta})\frac{T_0 - T_s}{T_s} - \frac{I_p}{T_s}]. \tag{2.17}$$

The terms within the square brackets in the above equation are correction terms, which account for both the surface effect, *i.e.* the discrepancy between the surface skin temperature T_s and the ground level air temperature T_0, and the atmospheric effect, *i.e.* the nonuniform vertical distribution of the air temperature. I_p, the atmospheric correction term, comprises two parts,

$$I_p = I_1 + (1 - \epsilon_s)I_2 e^{-2\tau_0 \sec\theta}, \tag{2.18}$$

in which I_1 represents the correction to the upwelling emissions of the atmosphere and $I_2 e^{-\tau_0 \sec\theta}$ represents the correction to the atmospheric downwelling emissions. They are calculated using the following equations:

$$\begin{aligned} I_1 &= -\int_0^\infty [1 - e^{-\tau(z,\infty)\sec\theta}]\frac{dT(z)}{dz}dz \qquad (2.19) \\ I_2 e^{-\tau_0 \sec\theta} &= -\int_0^\infty e^{-\tau(0,z)}[1 - e^{-\tau(z,\infty)\sec\theta}]\frac{dT(z)}{dz}dz. \qquad (2.20) \end{aligned}$$

$\tau(z_1, z_2)$ is the atmospheric opacity between two levels z_1 and z_2 at the nadir direction and defined as

$$\tau(z_1, z_2) = \int_{z_1}^{z_2} \alpha_a(z)dz. \tag{2.21}$$

Eq. (2.16) can be easily changed into the form for an atmosphere with constant temperature T_0 and $T_0 = T_s$,

$$T_{0,b}(\theta) = T_0 - (T_0 - T_c)(1 - \varepsilon_s)e^{-2\tau_0 \sec\theta} \tag{2.22}$$

In this case the quantity I_p reduces to zero and m_p reduces to unity. Eq. (2.22) is an approximate expression of Eq. (2.16) and it is very useful in interpreting the measurements when the atmosphere is moderately transparent at the used frequencies, *e.g.*, at the window channels of SSM/I.

2.2.2 The Expression of Brightness Temperature Difference

If the surface emissivities at two channels of a radiometer can be taken as equal, using Eqs. (2.16) and (2.22), the brightness temperature difference (BTD) between these two channels can be expressed explicitly.

For clarity and simplicity, the case of transparent atmosphere is considered at first, using Eq. (2.22). If the two channels are located on the wing of the water vapor line centered at 183.31 GHz, the atmospheric absorptions corresponding to these two channels will be sufficiently different. Suppose the atmosphere has total opacities at nadir direction of $\tau_{0,i}$ and $\tau_{0,j}$ for the two channels with numbers of i and j, respectively. The BTD between the two channels, $\Delta T_{0,ij}$, is then given by

$$\begin{aligned} \Delta T_{0,ij} &= T_{0,i} - T_{0,j} \\ &= (T_0 - T_c)(1 - \epsilon_s)(e^{-2\tau_{0,j}\sec\theta} - e^{-2\tau_{0,i}\sec\theta}). \end{aligned} \tag{2.23}$$

In cloud-free conditions, the total opacity of the atmosphere is just due to the absorptions of water vapor and oxygen. The oxygen absorptions at the SSM/T2 frequencies are sufficiently small; and they are in the same order of magnitude. This part of the atmospheric absorption is neglected in the following discussions. Now only the water vapor absorption needs to be considered in calculating $\tau_{0,i}$ and $\tau_{0,j}$. The total opacities should be evaluated with Eq. (2.21) and the integration should be carried out from the ground surface to the top of the atmosphere. Because the water vapor absorption is a function of both temperature and pressure, the relation between total opacity and total water vapor is nonlinear. Nevertheless, the relation between them is usually assumed to be linear, in a first order approximation; and a so-called mass absorption coefficient of water vapor is defined (*Westwater*, 1993). Let $\kappa_{v,i}$ represent the mass absorption coefficient of water vapor at channel i, the total opacity of channel i, $\tau_{0,i}$, is then expressed as a product of $\kappa_{v,i}$ and W,

$$\tau_{0,i} = \kappa_{v,i} W. \tag{2.24}$$

$\kappa_{v,i}$ is calculated using the following equation,

$$\kappa_{v,i} = \frac{1}{W} \int_0^H \alpha_{v,i}(z) dz \tag{2.25}$$

in which $\alpha_{v,i}(z)$ is the specific attenuation of water vapor at height z. The total water vapor W is evidently given by

$$W = \int_0^H \rho_v(z) dz \tag{2.26}$$

where $\rho_v(z)$ is the water vapor density at height z.

On the right hand side of Eq. (2.23) there is a term which is a summation of two exponential functions. In order to facilitate the following analysis, an approximation is used here to change the form of this term from summation into a product, which is given in the following general form,

$$e^{-2a_1 x} - e^{-2a_2 x} \approx A_1 x e^{-(A_2 x^2 + A_3 x)}. \tag{2.27}$$

The coefficients A_1, A_2 and A_3 in the approximation are calculated from the coefficients of a_1 and a_2, using the following equations

$$A_1 = 2(a_2 - a_1) \tag{2.28}$$

$$A_2 = -(a_2 - a_1)^2/6 \tag{2.29}$$

$$A_3 = a_2 + a_1, \tag{2.30}$$

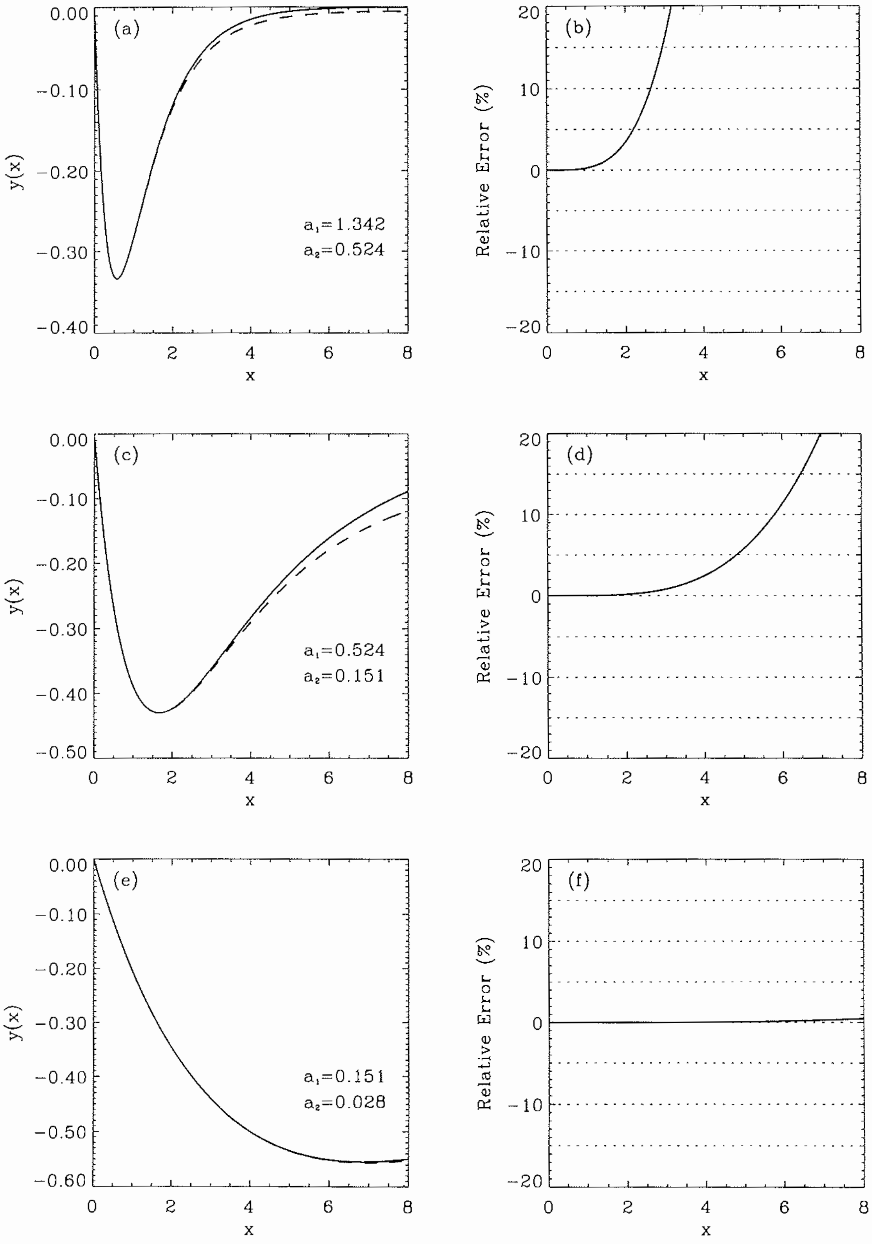

Figure 2.2: *Comparisons of function* $y(x) = e^{-2a_1 x} - e^{-2a_2 x}$ *(solid lines) and its approximation* $A_1 x e^{-(A_2 x^2 + A_3 x)}$ *(dashed lines), for three groups of a and b.*

which are derived by comparing the Taylor expansion, up to 3rd order, on the right hand side with that on the left hand side of Eq. (2.27). In Figure 2.2 the two functions are compared for three pairs of a_1 and a_2. This approximation has maximum errors of less than a few percent for x in the range of $0\cdots 2$ for group one (Figure 2.2(a) and (b)), in the range of $0\cdots 5$ for group two (Figure 2.2(c) and (d)), and in the whole range of $0\cdots 8$ for group three (Figure 2.2(e) and (f)). By using this approximations and the expression of total opacity in Eq. (2.24), the expression of BTD, $\Delta T_{0,ij}$, in Eq. (2.23) becomes

$$\Delta T_{0,ij} \approx 2(T_0 - T_c)(1-\epsilon_s)(\kappa_{v,i} - \kappa_{v,j})(W \sec\theta) e^{-(\kappa_{v,j}+\kappa_{v,i})(W \sec\theta) + \frac{(\kappa_{v,j}-\kappa_{v,i})^2}{6}(W \sec\theta)^2}. \tag{2.31}$$

As the atmosphere is moderately opaque at the used frequencies, the BTD, ΔT_{ij}, has to be calculated using the exact expression of T_b in Eq.(2.16). However, it can be proved that ΔT_{ij} has the following relationship with $\Delta T_{0,ij}$,

$$\Delta T_{ij} = T_i - T_j = \Delta T_{0,ij} + b_{ij}. \tag{2.32}$$

In the above equation, b_{ij} represents the bias when the brightness temperatures are calculated using the approximate expression of Eq.(2.22), instead of using the exact one of Eq.(2.16).

The bias b_{ij} is an important quantity. By combining Eqs. (2.16), (2.23) and (2.32) together, the expression of b_{ij} can be obtained,

$$b_{ij} = I_{p,i} - I_{p,j} + \epsilon_s(T_0 - T_s)(e^{-\tau_{0,j}\sec\theta} - e^{-\tau_{0,i}\sec\theta}). \tag{2.33}$$

Here, $I_{p,i}$ and $I_{p,j}$ are the atmospheric correction terms at channels i and j, respectively, which are given by,

$$\begin{aligned} I_{p,i} &= I_{1,i} + (1-\epsilon_s) I_{2,i} e^{-2\tau_{0,i}\sec\theta} && (2.34) \\ I_{p,j} &= I_{1,j} + (1-\epsilon_s) I_{2,j} e^{-2\tau_{0,j}\sec\theta}. && (2.35) \end{aligned}$$

In the above expression of $I_{p,i}$ ($I_{p,j}$), the second term in the right hand side represents the correction for the downwelling atmospheric radiation and it is much smaller than $I_{1,i}$ ($I_{1,j}$), the correction for the upwelling atmospheric radiation. This term will be ignored henceforth. It is noticed that there is a term in the expression of b_{ij}, which contains the difference between the surface air temperature T_0 and the surface skin temperature T_s. Since the continuity of temperature across the air-ice interface is normally maintained, T_s is equal to T_0. Under these conditions, the expression of b_{ij} in Eq. (2.23) is simplified to

$$b_{ij} \approx \int_0^H [e^{-\tau_{0,i}(z,H)\sec\theta} - e^{-\tau_{0,j}(z,H)\sec\theta}] \frac{dT(z)}{dz} dz. \tag{2.36}$$

It can be seen that b_{ij} is mainly determined by the vertical structure of temperature and water vapor.

2.2.3 The Ratio of Compensated BTD (RCBTD)

If there are three channels available on the flank of the water vapor absorption line at 183.31 GHz and the surface emissivity at these three channels can also be taken as equal, useful results can be derived from the BTDs between adjacent channels.

First of all, the case of a transparent atmosphere is considered, using the expression of BTD in Eq. (2.31). Let $\Delta T_{0,ij}$ and $\Delta T_{0,jk}$ represent the BTDs between channels i and j and between channels j and k, respectively. The ratio between $\Delta T_{0,ij}$ and $\Delta T_{0,jk}$ is then defined as a new quantity, which is represented by η_0 and has the following expression,

$$\begin{aligned}\eta_0 &= \frac{\Delta T_{0,ij}}{\Delta T_{0,jk}} \\ &= \frac{\kappa_{v,i} - \kappa_{v,j}}{\kappa_{v,j} - \kappa_{v,k}} e^{(\kappa_{v,k}-\kappa_{v,i})(W \sec\theta)+\frac{(\kappa_{v,j}-\kappa_{v,i})^2-(\kappa_{v,k}-\kappa_{v,j})^2}{6}(W \sec\theta)^2}. \qquad (2.37)\end{aligned}$$

By taking logarithms at both sides, the above equation becomes

$$\ln \eta_0 = c_0 + c_1(W \sec\theta) + c_2(W \sec\theta)^2, \qquad (2.38)$$

where coefficients c_0, c_1 and c_2 are given by

$$\begin{aligned} c_0 &= ln(\frac{\kappa_{v,i} - \kappa_{v,j}}{\kappa_{v,j} - \kappa_{v,k}}) & (2.39) \\ c_1 &= \kappa_{v,k} - \kappa_{v,i} & (2.40) \\ c_2 &= \frac{(\kappa_{v,j} - \kappa_{v,i})^2 - (\kappa_{v,k} - \kappa_{v,j})^2}{6}. & (2.41)\end{aligned}$$

For a moderately opaque atmosphere, the ratio of BTDs is defined as

$$\eta = \frac{\Delta T_{ij}}{\Delta T_{jk}} \qquad (2.42)$$

and the relationship between η and W is not as simple as in Eq. (2.38), due to the existence of a non-zero bias between ΔT_{ij} and $\Delta T_{0,ij}$, as shown in Eq. (2.32). In order to obtain a useful result for opaque cases, the definition of η must be modified. The modified η is represented by η_c and has the form of,

$$\eta_c = \frac{\Delta T_{ij} - b_{ij}}{\Delta T_{jk} - b_{jk}}. \qquad (2.43)$$

η_c is called Ratio of "Compensated" Brightness Temperature Differences (RCBTD). By noting the relationship between ΔT_{ij} and $\Delta T_{0,ij}$, it is immediately recognized that η_c has the same form as η_0 and it equals η_0 as the atmosphere becomes fully transparent, since in this case the biases b_{ij} and b_{jk} are zero. In this way, the relationship between η_c and W becomes as simple as that in Eq.(2.38). Further, if the three channels are selected in such a way that

$$\kappa_{v,j} - \kappa_{v,i} = \kappa_{v,k} - \kappa_{v,j} \qquad (2.44)$$

then,

$$c_0 = c_2 = 0. \tag{2.45}$$

As a result, the relationship between total water vapor W and $\ln \eta_c$ becomes a linear one.

$$\ln \eta_c = (\kappa_{v,k} - \kappa_{v,i})(W \sec \theta). \tag{2.46}$$

It is very interesting to note that the surface emissivity ϵ_s and surface skin temperature T_s vanished in both Eq. (2.38) and Eq. (2.46). This means, if the biases b_{ij} and b_{jk} can be reasonably well determined, the total atmospheric water vapor can be inferred from the measurements of the three channels, without any auxiliary information on the surface emissivity and surface skin temperature. This is the basic idea of the proposed RCBTD method. Obviously, the biases b_{ij} and b_{jk} are key elements in the RCBTD method.

2.2.4 The Relationship between RCBTD and TWV

In order to further study the relationship between RCBTD and TWV, simulations were done using the MWMOD module. For simplicity, the brightness temperatures of SSM/T2 channels were simulated at their center frequencies and with artificially created profiles of the atmosphere.

The temperature and water vapor profiles used are shown in Figure 2.3. The temperature in the troposphere is assumed to decrease linearly with height from the surface up to the tropopause at 9 km with a fixed lapse rate of 6.0 K/km; above the tropopause, the temperature is assumed to be constant. The error induced by this unrealistic temperature distribution is expected to be small, since the water vapor amount in the atmosphere above the tropopause is negligible compared with that in the troposphere. The water vapor profile is assumed to depend on pressure,

$$q(p) = q_s(\frac{p}{p_s})^\gamma \tag{2.47}$$

in which $q(p)$ stands for the specific humidity at pressure p; q_s is the surface specific humidity; γ is the power coefficient, which controls the vertical distribution of water vapor. As γ increases, water vapor is increasingly concentrated near the surface for a given amount of total water vapor. In view of the statistics given by *Simmer* [1994], γ takes the values of 1, 2 and 3 in this simulation. The surface pressure p_s is fixed at 1000 mb for all situations.

In Figure 2.4(a) a part of the simulated brightness temperatures at SSM/T2 channels is shown, as a function of the total atmospheric water vapor W. When W is small, the measured brightness temperature generally increases linearly with W. This feature has been used by *Wang and Wilheit* [1989] to retrieve the total water vapor in dry atmospheres over open ocean. As the auxiliary information, the ocean surface temperature and emissivity are needed in their retrieval scheme, in order to estimate the ocean surface emission. With the increase of W, the relation between T_b and W becomes nonlinear and finally the measured T_b runs into saturation. The nearer the channel is located to the center of the absorption line, the more sensitive

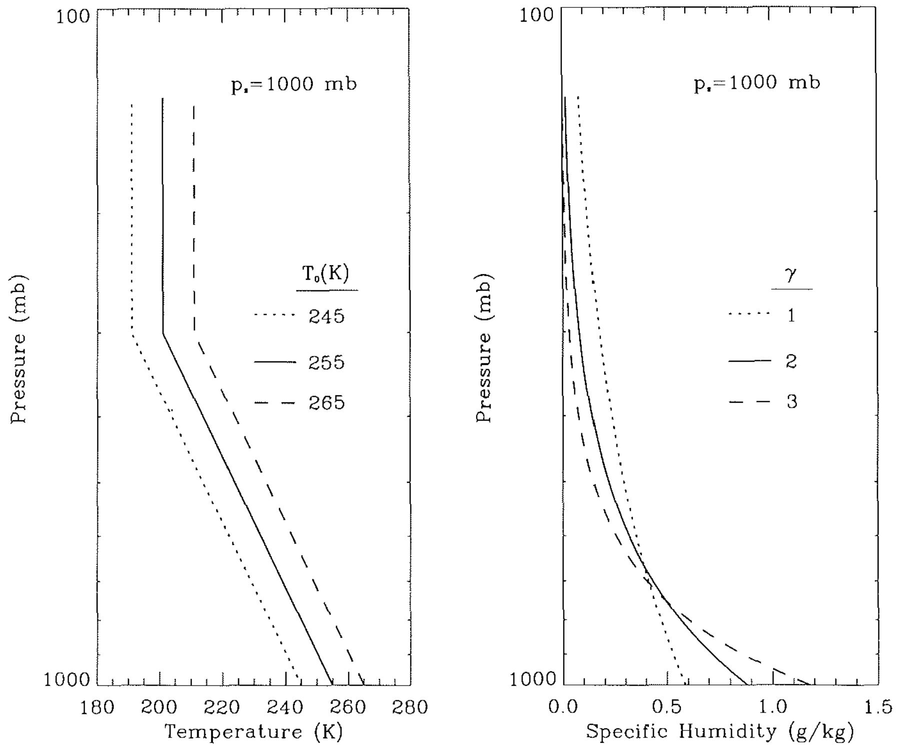

Figure 2.3: *The artificial profiles of temperature and humidity used in simulations. The humidity profiles are examples for total water vapor* $W = 3.0\ kg/m^2$.

it is and the sooner it reaches saturation. The saturation point $W_{s,i}$ of channel i is defined here as the value of W, at which the following conditions

$$\begin{array}{ll} T_{i-1} - T_i = 0 & \text{when } W = W_{s,i} \\ T_{i-1} - T_i > 0 & \text{when } W > W_{s,i} \end{array}$$

are satisfied. According to this definition, points A and B in Figure 2.4(b) are saturation points of channels 5 and 4, respectively. When the atmosphere contains water vapor above the saturation point of a channel, this channel "sees" no longer through the atmosphere. In this case, the measured T_b at this channel contains no information on the water vapor content in the lower layers of the atmosphere; therefore, this channel is not suitable for retrieving the total amount of the atmospheric water vapor. The saturation point defined here is used later as a criterion to indicate which channels are used in the retrieval. It must be pointed out that the thus defined saturation point changes with both the surface emissivity and the vertical structure of the atmosphere, since the brightness temperature difference between two channels, $T_{i-1} - T_i$, is a function of these two factors.

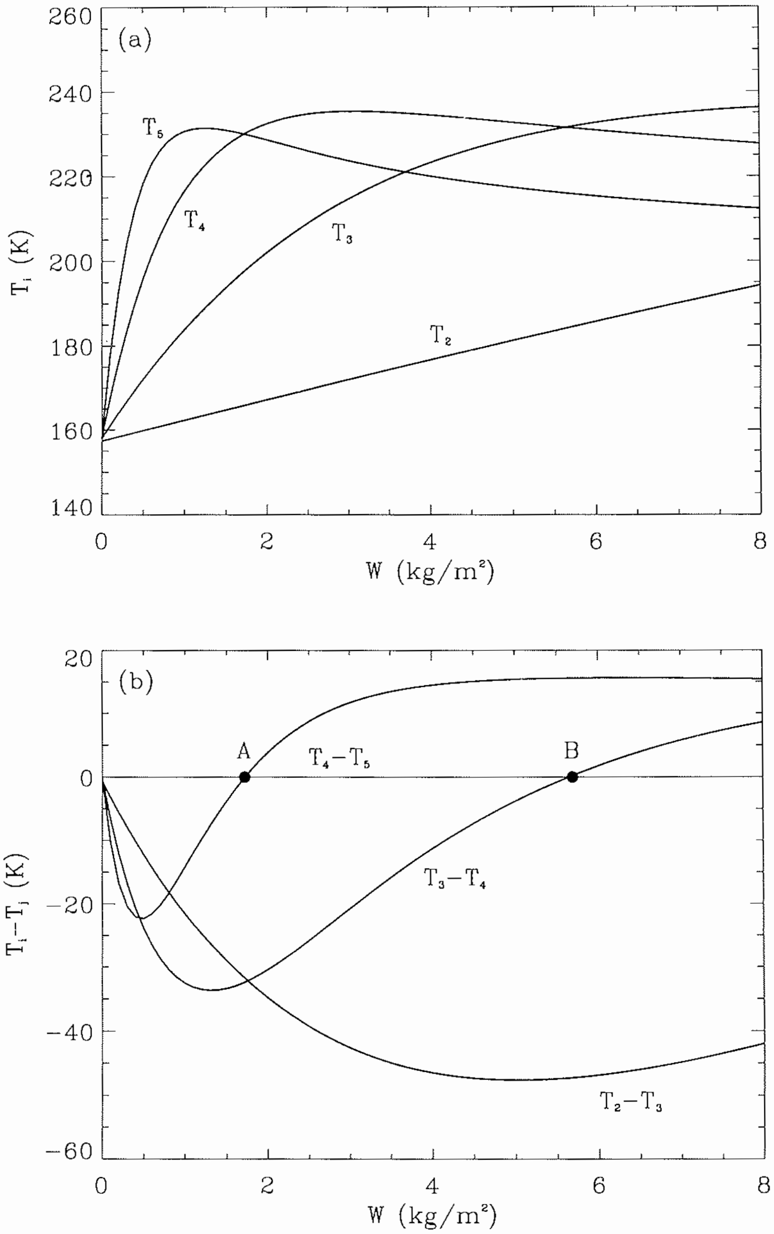

Figure 2.4: *Simulated results when* $\gamma = 2$, $T_0 = T_s = 255$ *K and* $\epsilon_s = 0.6$. *(a) The brightness temperatures at channels 2 to 5 of SSM/T2. (b) The brightness temperature differences between two neighboring channels.*

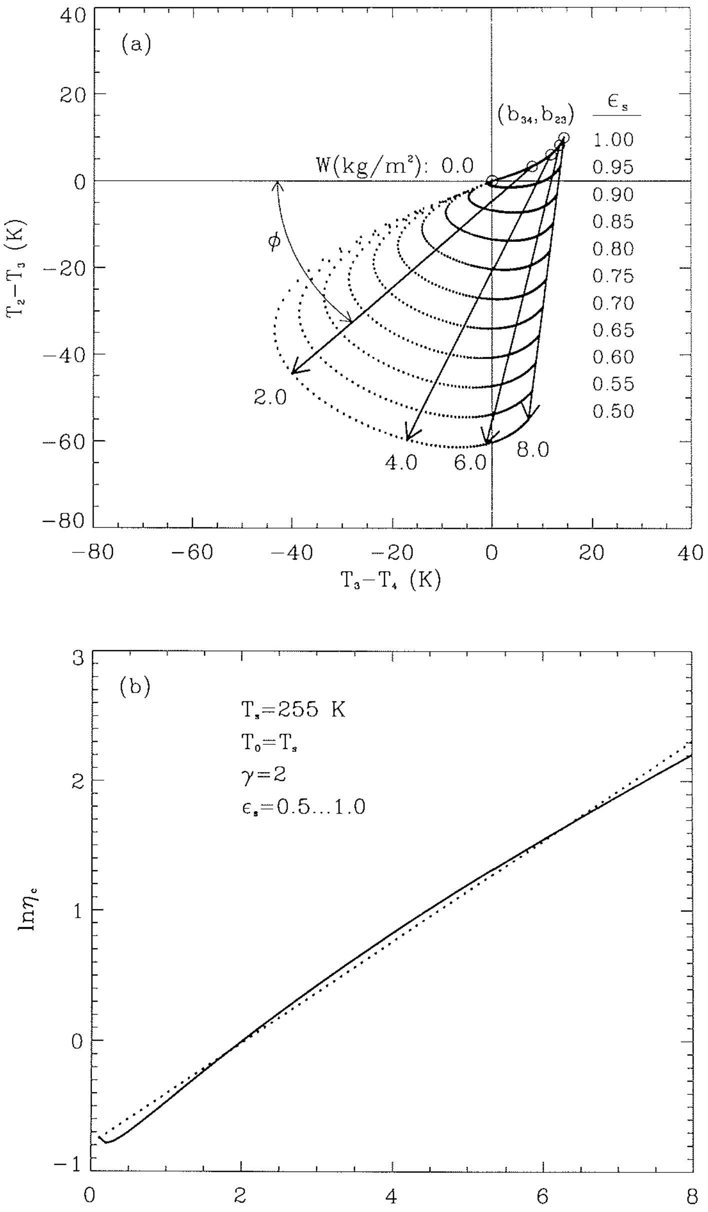

Figure 2.5: *RCBTD versus TWV in the plane of BTDs: (a) The trajectories of* ($T_3 - T_4$,$T_2 - T_3$) *as* W *increases from 0 to 8 kg/m*^{2} *in steps of 0.1 kg/m*^{2} *(dotted lines) and* ϵ_s *decreases from 1.0 to 0.5 in steps of 0.05 (solid lines). The open circles represent the positions of biases* (b_{34}, b_{23}) *at different values of* W*. (b) The relationship between* W *and* $\ln \eta_c$*, the linear part of which is shown by the dotted line.*

Figure 2.5(a) shows the effects of the total water vapor and the surface emissivities on the brightness temperature differences when the vertical structure of atmospheric temperature and humidity is fixed. Here, the simulated results at the channels 2, 3 and 4 of SSM/T2 are exemplarily used. Each point in the plane of BTD's $T_3 - T_4$ and $T_2 - T_3$ corresponds to a definite value of W and a definite value of ϵ_s. As W and ϵ_s change, the trajectories of $(T_3 - T_4, T_2 - T_3)$ are almost orthogonal with one another in a certain range of W. As a result, the effect of water vapor can be isolated from that of the surface emissivity in the plane of the brightness temperature differences between neighboring channels of SSM/T2. In Figure 2.5(a) some vectors are also exemplarily shown. The start points of these vectors are located at (b_{34}, b_{23}), which are biases corresponding to their W, while the end points of them are exemplarily shown at $(T_3 - T_4, T_2 - T_3)$ corresponding to $\epsilon_s = 0.5$. Clearly, the angles between the abscissa and these vectors can be evaluated using the following equation,

$$\tan\phi = \frac{T_2 - T_3 - b_{23}}{T_3 - T_4 - b_{34}}. \tag{2.48}$$

Comparing this equation with the definition of RCBTD η_c in Eq. (2.43), it is immediately realized that

$$\tan\phi = \eta_c. \tag{2.49}$$

Because η_c is independent of the surface emissivity ϵ_s, the angle ϕ must be independent of ϵ_s, too. This means, for a fixed W, all points of $(T_3 - T_4, T_2 - T_3)$ are located in the same line no matter what value the surface emissivities ϵ_s takes. Therefore, to retrieve total water vapor W, one just needs to calculate the angle ϕ. The relationship between $\tan\phi$, *i.e.* η_c, and W is shown in Figure 2.5(b). Evidently, the curve is in the form of a 2nd-order polynomial, as described by Eq.(2.38). Now it is concluded that the model simulation confirms the theoretical analyses in Section 2.2.3.

2.3 Influence of the Atmospheric Vertical Structure

The preceding analyses and simulations were confined only to cases of fixed temperature and humidity profiles of the atmosphere. In reality, however, the atmospheric vertical structure is subject to great variation both spatially and temporally. This variation will influence the retrieval of the total water vapor in the atmosphere using RCBTD, since the temperature and pressure dependency of water vapor absorption has influences on the relationship between the total water vapor and the RCBTD through the mass absorption coefficients contained in Eq. (2.38) and on the compensation of the biases b_{ij} and b_{jk}.

2.3.1 The Mass Absorption Coefficients

As demonstrated in Section 2.2.3, the relationship between $\ln\eta_c$ and the total water vapor W is in the form of a 2nd-order polynomial (see Eq. (2.38)), if the biases b_{ij}

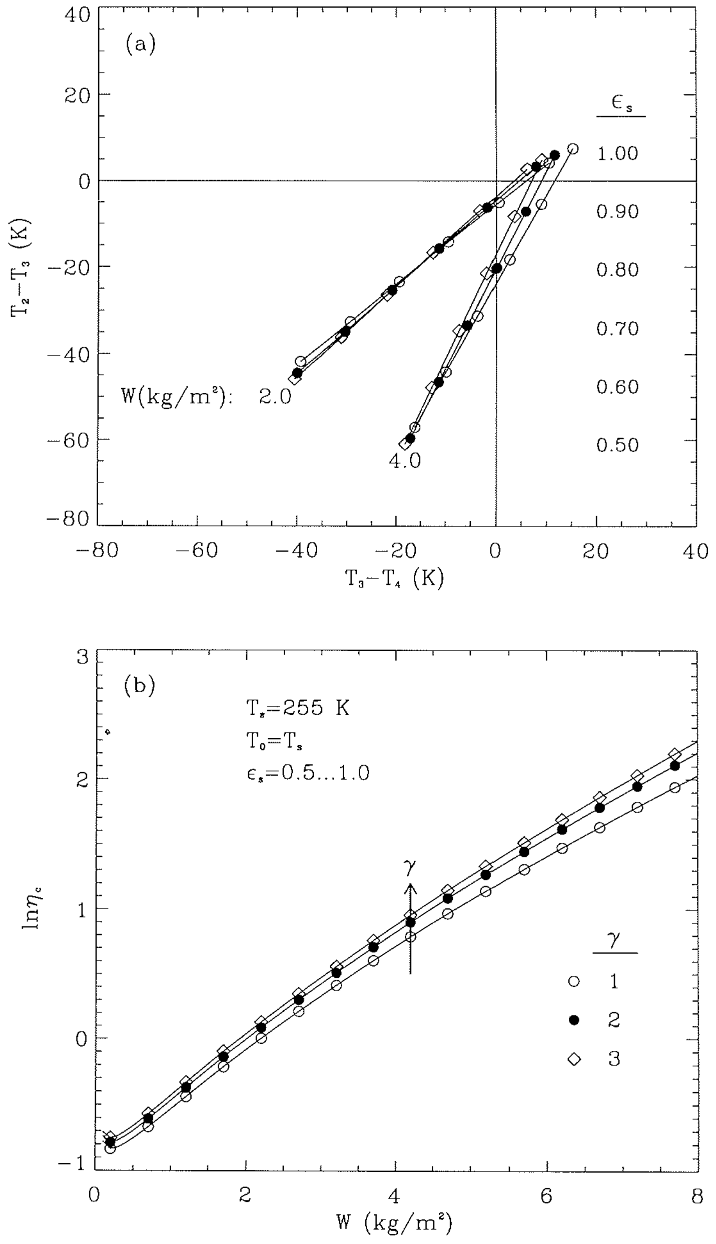

Figure 2.6: *The influence of the vertical distribution of water vapor on the relationship between RCBTD* η_c *and total water vapor* W. *(a) The movement of point* (T_3-T_4, T_2-T_3) *with* γ *on the plane of brightness temperature differences. (b)* $\ln \eta_c$ *versus* W *for cases of different* γ. *The arrow shows the direction of increasing* γ.

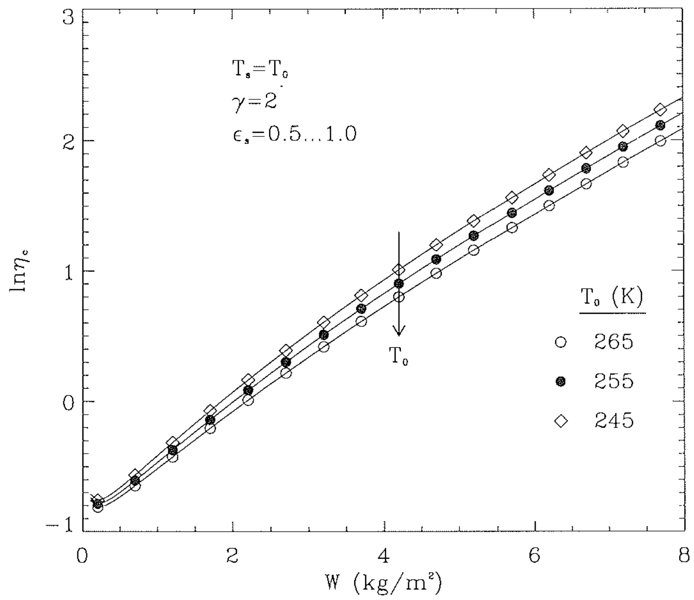

Figure 2.7: *The influence of air temperature on the relationship RCBTD* η_c *and total water vapor* W*. The arrow shows the direction of increasing air temperature.*

and b_{jk} were perfectly compensated; and the coefficients c_0, c_1 and c_2 in Eq. (2.38) would depend only on the mass absorption coefficients of water vapor, $\kappa_{v,i}$, $\kappa_{v,j}$ and $\kappa_{v,k}$, as given by Eqs.(2.39)-(2.42). According to the definition in Eq. (2.25), the mass absorption coefficient of water vapor is equal to the total absorption of the water vapor at all levels of the atmosphere divided by the total amount of water vapor. The temperature dependency of water vapor absorption is a complex function of frequency, especially near the center of the absorption lines (*Gibbins*, 1986). The work of *Westwater* [1993] at frequencies of 20.6, 31.65 and 90.0 GHz showed that the variations of the mass absorption coefficients at these frequencies are at most 15% in a time scale of one month, for typical mid-latitude clear conditions with the total water vapor in the range of 5–20 kg/m^2. Up to now, no similar work at frequencies above 100 GHz is reported in the available literatures. In order to observe the effect of the atmospheric structure on the RCBTD η_c, simulations were done and the results are presented here.

The simulated results shown in Figure 2.6(a) are obtained when the vertical structure of water vapor changes and the temperature and pressure profiles are fixed. For clarity, just the results with W of 2.0 and 4.0 kg/m^2 are shown. Although the points ($T_3 - T_4, T_2 - T_3$) for a fixed γ are still located on a line as the surface emissivity ϵ_s changes, the slopes of lines with different γ are different. In Figure 2.6(b), the relationships between $\ln \eta_c$ and W for different γ are shown. The influences of water

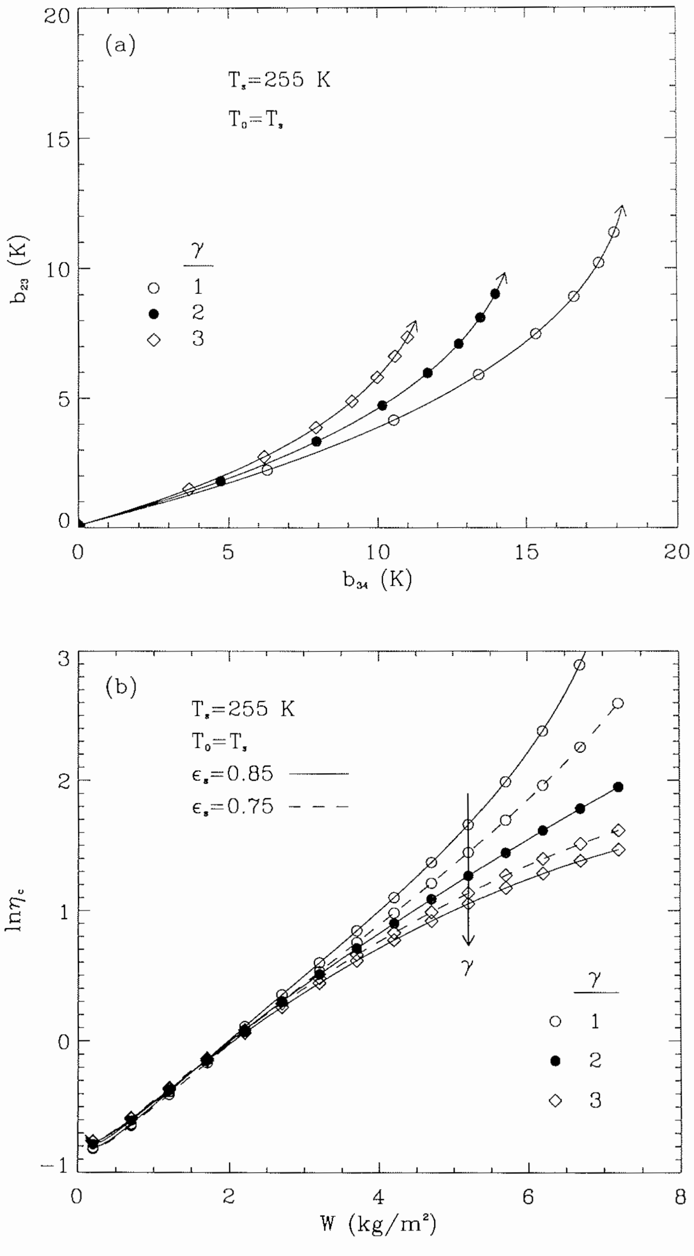

Figure 2.8: *(a) Biases* b_{34} *versus* b_{23}*. The arrows show the directions of increasing* W*, with the step of 1 kg/*m^2*. (b)* $\ln \eta_c$ *versus total water vapor* W*, when the biases are compensated using the values corresponding to* $\gamma = 2$*. The arrow shows the direction of increasing* γ*.*

vapor vertical distributions in the atmosphere are significant. Similar effects are also observed in Figure 2.7, when the air temperature changes while the profiles of water vapor and pressure are fixed.

2.3.2 The Biases

The effects of the atmospheric vertical structure on the retrieval of total water vapor using RCBTD can also be observed in the biases, b_{ij} and b_{jk}. As shown in Eq. (2.36), the biases are mainly determined by the vertical structure of the atmosphere. Figure 2.8(a) shows the biases b_{34} and b_{23} as a function of γ and W for a fixed temperature profile. As expected, the biases changes nonlinearly with γ and W, and the vertical structure of water vapor plays an increasingly important role with the increase of total water vapor W. Because of this nonlinear dependency of the biases on the total amount of the atmospheric water vapor and on its vertical structure, a perfect compensation of the biases in calculating RCBTD with Eq. (2.43) is difficult in reality. The effect of the imperfect compensation of the biases in calculating RCBTD is exemplarily shown in Figure 2.8(b). Here, all of the RCBTD η_c are calculated using the biases corresponding to $\gamma = 2$. Significant divergence appears when the total water vapor W is large. The effects of the surface emissivity, which would have vanished if the biases were perfectly compensated, show up again in this case.

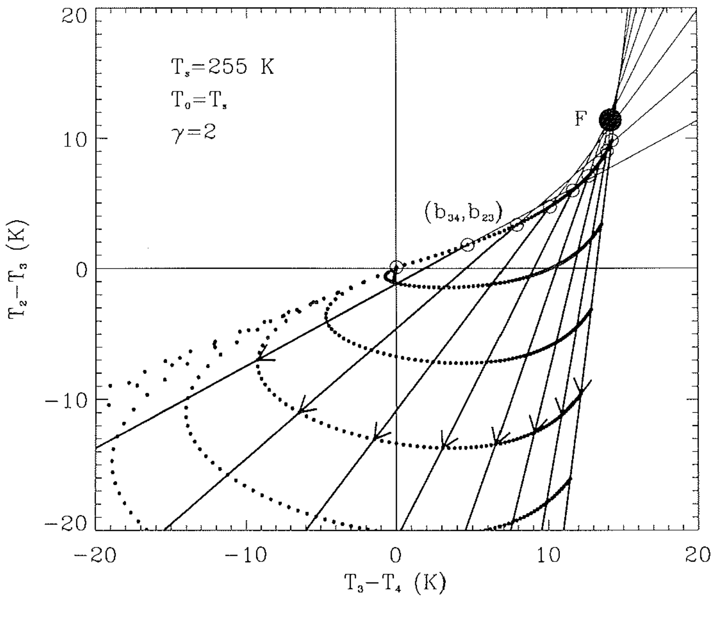

Figure 2.9: *A part of Figure 2.5(a). The extended lines (thin lines) intersect with each other at nearly the same point F.*

The difficulty in compensating the biases can be reduced. First, the retrieval of the total water vapor using the RCBTD is performed regionally and seasonally. In this way, the variation of the vertical structure of the atmosphere is limited to a tolerable extent. Second, in constructing the algorithm, the work is done for certain ranges of the ground surface emissivity and the total amount of atmospheric water vapor, so that the divergence is limited to a small extent. At last, the problem due to the dependency of the biases on the total water vapor amount in the atmosphere can be solved, if the following fact is noted. In Figure 2.9 a part of Figure 2.5(a) is reproduced in a larger scale. By extending the lines with constant W in the direction of increasing ϵ_s, the lines intersect with each other at nearly the same point F. As proved in Section 2.3.3, RCBTD η_c is equal to $\tan\phi$. ϕ is the angle between the abscissa and the line determined by points with constant W. If all the lines intersect at one point, only the coordinates of this intersection is needed in calculating $\tan\phi$, *i.e* RCBTD η_c. In practice, the temperature and humidity profiles measured with radiosondes can be used to estimate the optimal position of this intersection.

Chapter 3

Surface Temperature and Emissivity of Ice

In order to develop an algorithm for the retrieval of total water vapor in Antarctica using the RCBTD method, the climatological and meterological conditions in this region should be understood. After an abbreviated overview of the physical environment in the Antarctica, algorithms for ice surface temperature using infrared sensors are discussed in detail. Since there is a general lack of knowledge about the emission properties of ice at frequencies above 100 GHz, satellite measurements are used here to retrieve the surface emissivities of both land and sea ice. Therefore, a simple approach is proposed to estimate the range of surface emissivities without coincident measurements of the atmospheric profiles.

3.1 The Physical Environment in Antarctica

Antarctica comprises the area of the Earth south of 60° S and includes the ice covered continent, isolated islands and a large part of the Southern Ocean. The continent itself makes up about 10% of the land surface of the Earth with the combined area of the ice sheets and ice shelves being about 18×10^6 km^2. It lies entirely within the Antarctic Circle, except for the northern part of the Antarctic Peninsula and the region south of the Indian Ocean (see Figure 3.1).

The vast majority of the surface of the Antarctic continent is covered with ice, which is formed through precipitation of snow that has built up and has been compressed over thousands of years. The Antarctic ice sheet is on average about 2,500 m thick with maximum values reaching 4,700 m. Due to this thick ice mass Antarctica is, on average, the highest continent in the world. The most part of East Antarctica is covered with a terrestrial ice sheet that rests on land which would be above sea level if the ice were removed; the West Antarctica, in contrast, is mainly covered with marine ice sheet resting on rock as much as 2,000 m below sea level. The ice that builds up in the interior of the Antarctic gradually flows down to the edge of the continent in ice streams. When the ice streams reach the edge of the continent they either form floating ice shelves or the ice breaks up, forming

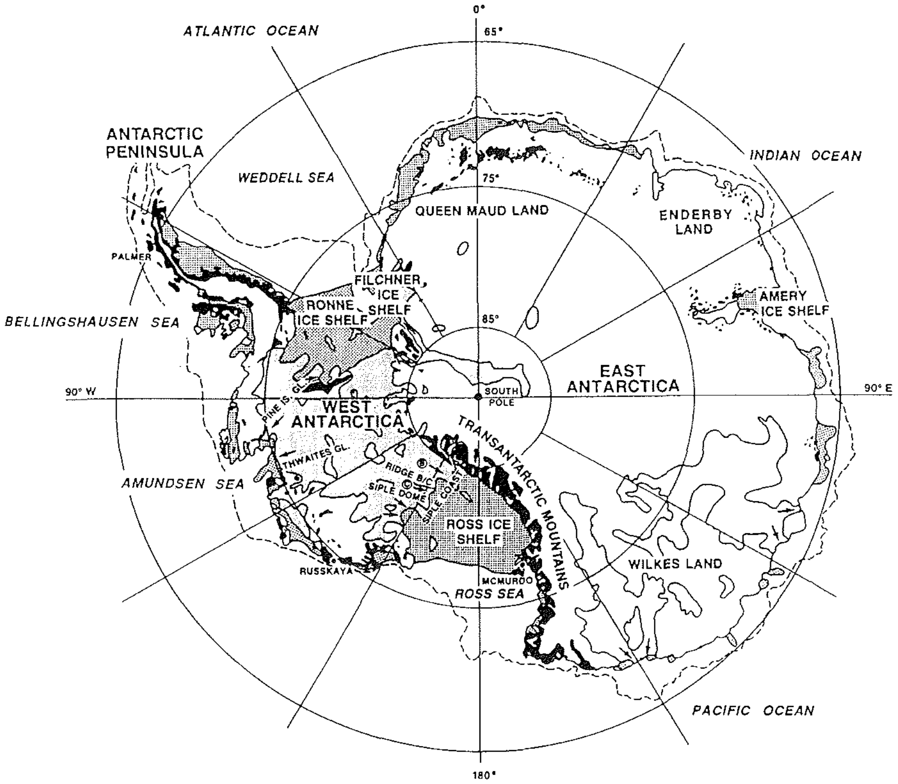

Figure 3.1: *Map of Antarctica. Light shaded areas represent portions of the ice sheet grounded on bedrock more than 500m below sea level, and represents a large proportion of the marine ice sheet. Arrows indicate the major ice streams. Heavily shaded regions are ice shelves, and solid areas represent the approximate distribution of exposed rock. The dashed line represents the edge of the continental shelf. (From Massom [1991])*

the tabular icebergs. The largest ice shelves are the Ross Ice Shelf and the the Filchner-Ronne Shelf. Most ice shelves are 100–500 m thick.

In most time of the year, the Antarctic continent is enclosed by a belt of sea ice that, at its maximum extent, reaches 60° S around most of the continent and close to 55° S to the north of the Weddell Sea. Sea ice is formed from the freezing of sea water. If sea ice would freeze extremely slowly, pure ice would result because of rejection of all salts during the freezing process. However, the freezing rate is normally too rapid to allow pure ice to form, thus brine is trapped in the lattice structure of the ice. Both meltwater percolation and gravity expedite brine drainage. Typical sea ice salinities are 10–15 parts per thousand (ppt) for newly formed sea ice, 5–8 ppt for 1–2 m thick first-year ice and 0.1–3.0 ppt for multiyear sea ice (*Hall and Martinec*, 1985). It is found that most of the Antarctic sea ice is first-year ice and relatively thin, but multi-year sea ice has also been observed in the western part of the Weddell Sea and along the coast of West Antarctica. Normally, the Antarctic sea ice is covered with snow; but its regional and seasonal variability in terms of its structure and thickness distribution is not well known. *In situ* observations during expeditions to the Weddell Sea in the time period from 1986 to 1992 obtained the following results: (1) the mean snow thickness over the first-year ice in the central and eastern Weddell Sea amounted 0.16 m, while that over the second-year ice in the northwestern Weddell Sea was 0.53 m; (2) the mean density of the snow in the Weddell Sea was 290 kg/m^3 (*Eicken et al.*, 1994). Since the ice is constantly driven by winds and ocean currents, the sea ice zone is highly dynamic. As a result, leads, which are ice-free regions between ice floes, are commonly created within the pack ice.

Antarctica is the coldest, windiest and driest continent on the Earth. The surface air is intensely chilled by radiative cooling as heat is lost from the ice surface to space. On the dome-shaped ice cap, the temperature decreases with the distance from the coast, since the elevation of the continental interior increases in general with the latitude. In most coastal regions the mean annual temperature is around -12°C, at 1,000 m -20°C, and in the highest parts near 4,000 m it falls to -60°C (see Figure 3.2). In the vertical structure of the atmospheric temperature profiles there is a temperature increase from the ice surface to about 700–1000 m above the ice surface. This phenomenon is known as the surface temperature inversion. Although the inversion is strongest in the interior of the continent in the winter, when the cooling of the surface is highest, significant inversions occur for much of the year even in the coastal region. The inversion strength, which is defined as the difference between the surface temperature and the highest temperature observed in the lower troposphere, can reach 25°C in winter at the interior of East Antarctica, as shown in Figure 3.3. Additionally, the katabatic wind regime is also one of the most remarkable features of Antarctic climatology, which is mostly caused by the strong radiative cooling of the ice sheet. The gravity driven flow moves very slowly downwards from high elevation areas of the ice cap, accelerating as it moves towards the coast. The configuration of the ice topography provides an extensive elevated source of cold air and lower lying glacial basins which cause strong confluence of airflows. As the katabatic winds move towards the coast the very cold, very dense and high velocity airflow is confined to a layer about 600 m thick, with the fastest winds at a height of about 200 m above the ice surface. Antarctic air is extremely dry. Air in the upper levels of the atmosphere circulates towards Antarctica from more northern latitudes. By the time the air descends over the polar central plateau to approach the boundary layer of the atmosphere, most of the moisture has been removed. The annual precipitation of snow, averaged across the continent, is about 100 mm of water equivalent. In some locations as little as 20 mm is recorded. Because of the low temperatures, however, there is little or no melt. The knowledge of the spacial distribution and seasonal variation of the precipitation over the Antarctic continent is essential to our understanding of the stability and mass balance of the Antarctic ice sheet, and consequently, essential to the prediction of global sea level changes.

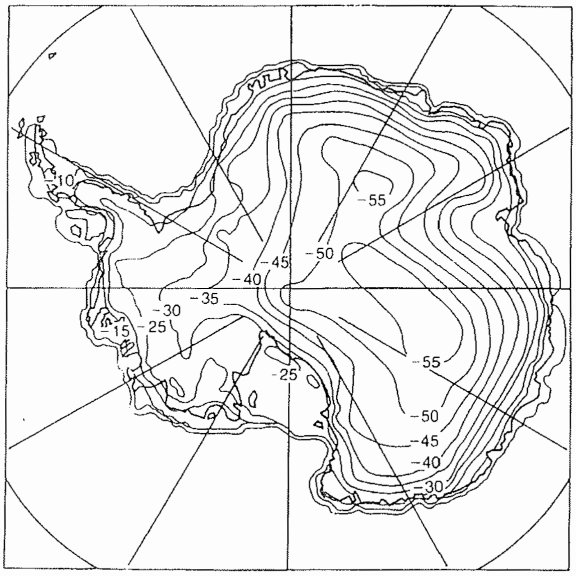

Figure 3.2: *Annual mean surface temperatures (in °C) over Antarctica, deduced from 10 m snow temperature measurements. (From King and Turner, 1997)*

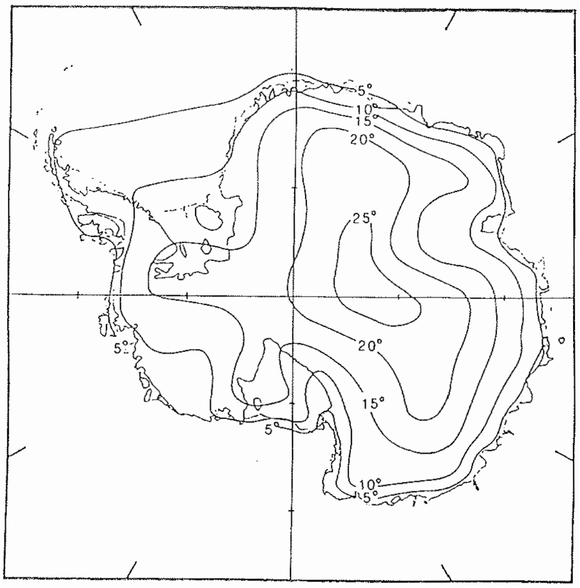

Figure 3.3: *Isolines of the average strength of the surface temperature inversion in the winter. (From Schwederfeger, 1984)*

3.2 Surface Temperature of Ice from Infrared Sensors

3.2.1 Physics Related to Infrared Sensors

Due to the hostile environment in Antarctica, the direct measurements of ice surface temperatures are sparse. Hence, the observations made from the polar orbiting satellites are valuable supplements. To measure the ground surface temperature from satellite, infrared sensors are commonly used, since the peak of the emission spectrum of the terrestrial surfaces is located near $10\,\mu$m wavelength and the atmosphere is moderately transparent to radiation in the thermal infrared range. The penetration depth of infrared radiation in geophysical materials (soil, ice, water, snow *etc.*) is very small (of the order of microns), while their emissivities are generally high. Consequently, the measured radiation in the infrared range is mainly emitted from the ground surface.

To interpret the measurements from infrared sensors, Planck's Law is used. The radiance B_λ of a blackbody with the physical temperature T is described by the Planck function,

$$B_\lambda(T) = \frac{2\hbar c^2}{\lambda^5}\frac{1}{e^{\hbar c/(\lambda k T)} - 1}, \tag{3.1}$$

where $\hbar$ is Planck's constant; and k is Boltzmann's constant. The radiance B_λ represents the radiant flux per unit solid angle in a given direction, per unit projected area in that direction, within unit range of wavelength. B_λ has thus the unit of W·m^{-3}·sr^{-1}. Generally, the radiant flux, L, received by a spaceborne radiometer at local zenith angle θ is directly related to the radiance of the Earth surface in that direction (*Robinson*, 1985). By ignoring the effect of the intervening atmosphere, L is simply given by

$$L = \epsilon(\theta, \lambda) B_\lambda(T), \tag{3.2}$$

where $\epsilon(\theta, \lambda)$ is the surface emissivity at local zenith angle θ and wavelength λ. In practice, however, a radiometer receives radiation only over a certain range of wavelength and local zenith angles, which are determined by the receiver passband and the antenna beamwidth, respectively. Consequently, the radiant flux L measured by a radiometer is an integration over wavelength and local zenith angle. For simplicity, however, Eq. (3.2) is still used, but with a modification that $\epsilon(\theta, \lambda)$ is replaced by $\bar{\epsilon}$, an average emissivity of the surface within the wavelength range determined by the passband of the receiver and within the range of the local zenith angle determined by the antenna beamwidth.

Since Antarctic ice is usually covered by snow, its emission in the infrared range is determined by the emission property of snow. The emissivity of snow in the infrared range of interest is quite insensitive to surface parameters, including density, grain size, thickness, liquid water content, and impurity content, but it has an angular and spectral dependency (*Massom and Comiso*, 1994). The directional emissivities of snow at the thermal channels (channels 4 and 5) of the Advanced Very High Resolution Radiometer (AVHRR) on board the NOAA series satellite, have been modeled by *Key and Haefliger* [1992], and their results are shown in Figure 3.4.

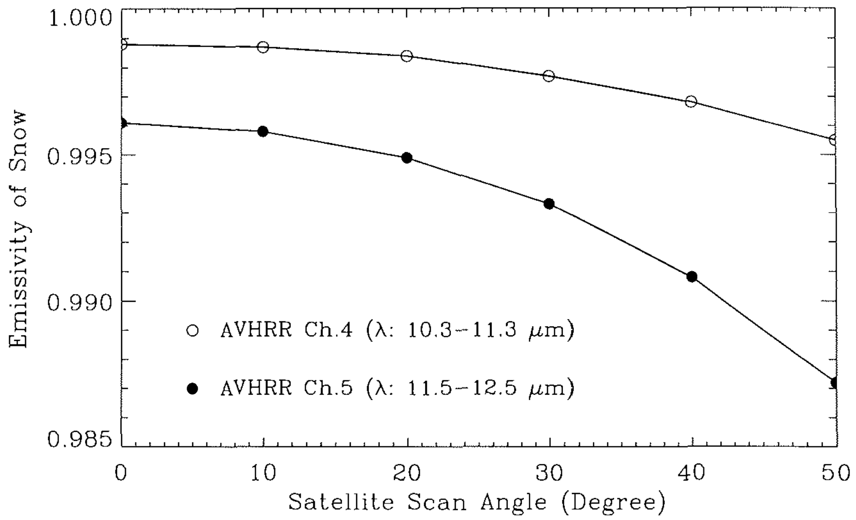

Figure 3.4: *The modeled directional emissivities of snow at channels 4 and 5 of NOAA AVHRR. (Data from Key and Haefliger [1992])*

They also found that these emissivities do not change significantly over the range of temperatures encountered in polar regions and therefore these values are applicable to the snow type encountered through all seasons of the year.

3.2.2 Surface Temperature of Sea Ice from OLS Data: An Algorithm

Much work has been done in retrieving the ice surface temperature using AVHRR (*Maslanik and Key*, 1993; *Yu et al.*, 1995). AVHRR has five channels, covering the range of the electromagnetic spectrum from visible to thermal infrared. Using the so-called "split-window" technique, the effects of atmospheric water vapor absorption can be corrected, based on the fact that atmospheric transmission is greater at channel 4 than at channel 5. In analyzing the data of SSM/T2, it is desirable to use the images of the Operational Linescan System (OLS), because OLS is on board the same spacecraft with the microwave sensor and therefore provides coincident measurements. In comparison with AVHRR, OLS has the disadvantages of fewer channels and wider bandwidth. OLS has only two channels, one in the visible band (0.4–1.1 μm) and one in the infrared (IR) band (10.5–12.6 μm). Hence, the algorithms of AVHRR cannot be directly used in processing OLS images and there is a need to develop dedicated algorithms for OLS.

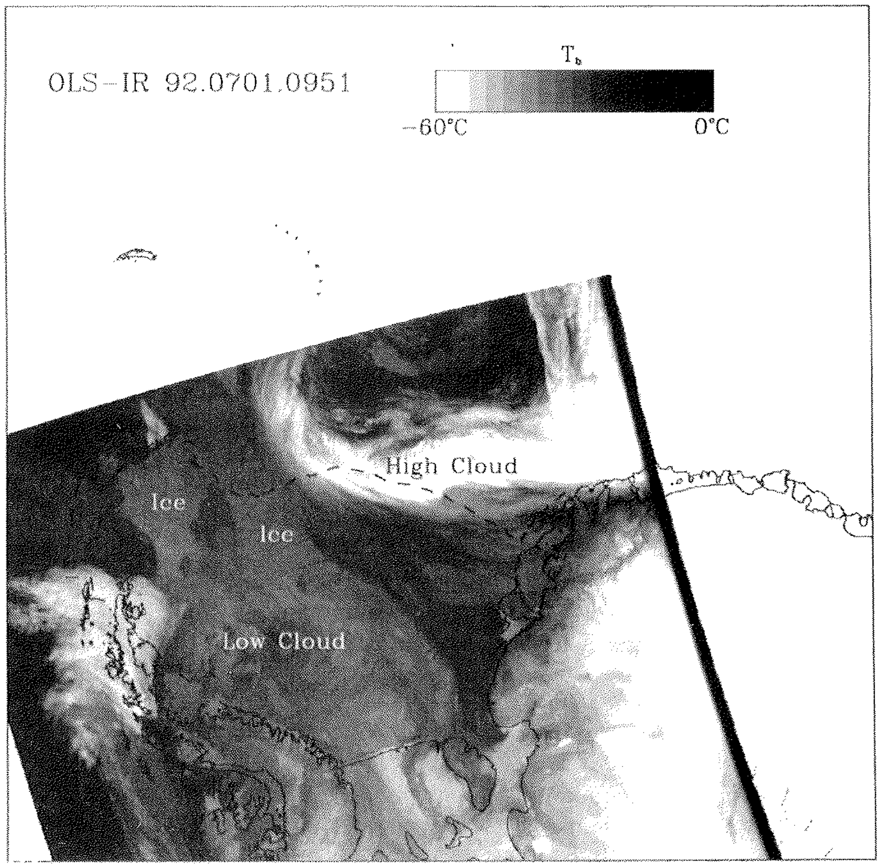

Figure 3.5: *OLS IR image over the Weddell Sea, Antarctica. Clouds and sea ice surface are classified through visual inspection. The dashed curve through the Weddell Sea represents the expedition route of R/V Polarstern in July 1992.*

3.2.2.1 Cloud Masking

To retrieve the surface temperature using visible and infrared images, clouds have to be detected and masked out at first. In polar regions the similar reflectances of clouds and snow/ice surfaces make the separation difficult by using visible channels. It is even more difficult in the long polar night, when only the infrared images are available. Due to the prevailing temperature inversion, unambiguous classification of clouds and ice surfaces is impossible using the simple threshold technique. In order to solve these problems, *Schlueter and Markus* [1996] have used neural networks to classify OLS infrared images through texture analysis, based on the statistical characteristics of segments. To use this technique, the neural networks must be trained using classified images, which are obtained commonly through visual inspection. The human eye, combined with human experience, is a powerful tool. Visual inspection is based on the fact that sea ice surface temperature is usually warmer

Table 3.1: Average Emissivities of Snow and Water at OLS IR Channel

Averaged over	$\bar{\epsilon}_s$ (Snow)	$\bar{\epsilon}_w$ (Water)
λ: 10.5–12.6 μm; θ: 0–55°	0.9954	0.9850

than −50°C and it looks rougher than cloud tops due to the existence of re-frozen leads, ice ridges and open water pools. One of the problems for the visual inspection is the influence of thin clouds, which can not be easily detected due to their low opacity and may cause an error of a few Kelvin. Figure 3.5 shows an example of thus classified OLS infrared images.

3.2.2.2 The Expression of the Surface Temperature of Sea Ice

In cloud-free cases the radiance measured by OLS represents the integrated radiances of all the surfaces within the field of view, which is a mixture of ice and open water. Usually, the measured radiance of OLS is expressed as the effective brightness temperature T_b, *i.e.* the temperature of a black body, at which it has the same radiance as the measured one. In general, the surfaces of ice and water have different temperatures. The surface temperature of sea water is assumed here to be at its freezing point, *i.e.* −1.8°C. If the ice concentration within the OLS pixel is C_{ice}, the total radiant flux L received by OLS can be written as

$$\begin{aligned} L &= B_\lambda(T_b) \\ &= C_{ice}\bar{\epsilon}_s B_\lambda(T_{ice}) + (1 - C_{ice})\bar{\epsilon}_w B_\lambda(T_w), \end{aligned} \tag{3.3}$$

in which T_{ice} is the surface temperature of ice, T_w is the surface temperature of sea water; $\bar{\epsilon}_s$ and $\bar{\epsilon}_w$ are the emissivities of snow and water at the OLS IR channel, respectively. Both DMSP and NOAA satellites are sun-synchronous orbiters at an altitude lower than 1,000 km; the sensors AVHRR and OLS both observe the Earth by cross-track scanning with nearly same swath width of 3,000 km (*Kramer*, 1996). Since the bandwidth of the infrared channel of OLS covers the combined spectral range of channels 4 and 5 of AVHRR, the emissivity of snow at the OLS IR channel, is taken as the average of the emissivities at channels 4 and 5 of AVHRR. Sea water has a smaller emissivity than snow. Here, the value given by *Comiso* [1994] is adopted. The emissivities used for snow and sea water at the IR channel of OLS are shown in Table 3.1.

By solving Equation (3.3), the ice surface temperature T_{ice} can be obtained. In order to get a simple expression for T_{ice}, the Planck function B_λ in Eq. (3.1) is replaced by an approximate expression. It is found that, for the wavelength range and temperatures considered, B_λ can be approximated by a power law of temperature,

$$B_\lambda(T) \propto T^m, \tag{3.4}$$

and that m can be taken as constant (*Price*, 1989). Using this approximation, T_{ice} is simply given by

$$T_{ice} = \left(\frac{T_b^m - (1 - C_{ice})\bar{\epsilon}_w T_w^m}{C_{ice}\bar{\epsilon}_s}\right)^{\frac{1}{m}}. \tag{3.5}$$

For the IR channel of OLS and for the temperature range encountered in polar regions, m takes the value of 5.0. Thus, using the brightness temperature measured by the IR channel of OLS and the ice concentration obtained from SSM/I measurements, the surface temperature of sea ice can be calculated using Eq. (3.5).

3.2.2.3 Correction of the Atmospheric Effect

In the above discussion, the effect of the clear atmosphere was ignored. Although the polar atmosphere is reasonably transparent at thermal infrared wavelengths, it has some effects on the measured T_b and this effect is not constant in the whole Antarctic region. In regions near sea ice edges or in areas with low ice concentrations, the water vapor content in the atmosphere is much higher than over the compact pack ice or the continental ice sheet. Furthermore, the surface temperature inversion in regions near sea ice edges is also weaker; accordingly, the average atmospheric temperature can be considerably lower than the ice surface temperature. In this case, the error of measured T_b can be large. In addition, the imperfect calibration of the radiometer is also a source of error. To minimize the retrieval error, a correction is derived by comparing the surface temperature of ice from *in situ* measurements with those retrieved using Eq. (3.5).

The *in situ* measurements were made during the expedition of the research vessel R/V Polarstern across the Weddell Sea in July of 1992 (see Fig. 3.5). The measured temperatures were not the surface skin temperatures of snow, instead, the standard 2-meter air temperatures. The surface skin temperatures are obtained here by subtracting 1.4°C from the standard 2-meter air temperatures, to account for the statistical cold bias of the snow surface relative to the 2-meter air (*Schwederfeger*, 1984; *Yu et al.*, 1995). During the expedition the standard 2-meter air temperatures were measured every 3 hours, with over 150 measurements. In the same time period there were 41 OLS images available, but only 10 images under clear sky conditions.

In order to make the comparison meaningful, a reasonable amount of data is needed. For this purpose, available data of AVHRR channel 4 in July 1992 are used to infer the T_b of OLS IR channel, when the OLS image was not available. The relationship between the AVHRR T_b and the OLS T_b is obtained through a linear regression of the nearly coincident measurements of AVHRR and OLS. The time differences of the compared data of AVHRR and OLS are less than 1 hour and are projected onto the same grid with a spatial resolution of 5 km. Figure 3.6 compares the coincident measurements of AVHRR and OLS. It is evident that the AVHRR channel 4 gives in general higher brightness temperatures than the OLS IR channel. This is consistent with the larger emissivity of snow and the higher transmittance of the atmosphere at AVHRR channel 4 than at the OLS IR channel. The linear equation describing the relationship between T_b from AVHRR and T_b from OLS is

$$T_b(\mathrm{OLS}) = 27.15 + 0.88 T_b(\mathrm{AVHRR\ Ch.4})\ (\mathrm{K}). \tag{3.6}$$

By including the AVHRR data, the number of intercomparisons between spaceborne and ground based measurements is expanded to 28, and most measurements were done at regions with high ice concentrations, as shown in Figure 3.7(a). The surface temperatures of sea ice, which are calculated using OLS data, are averages

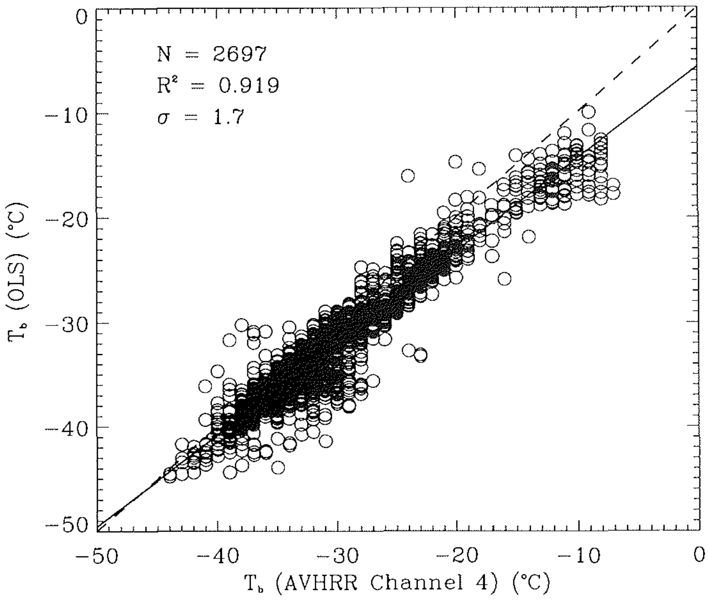

Figure 3.6: *Coincident observations of OLS and of AVHRR. N is the number of samples, R is the correlation coefficient, and σ is the root-mean-square residual.*

within an area of 45 × 45 km^2 surrounding positions of the *in situ* measurements. Referring to Figure 3.7(b), the calculated surface temperatures are in general lower than the *in situ* measured values, especially in warm regions. One of the reasons is the absorption and emission of water vapor. The larger scatter in Figure 3.7(b) at higher temperatures may be related to the larger error of ice concentration determination using SSM/I. Through linear regression, the relationship between measured and calculated ice surface temperatures is obtained as

$$T_{ice}(\text{Measured}) = -25.91 + 1.12 T_{ice}(\text{OLS}) \text{ (K)}. \tag{3.7}$$

3.2.2.4 Procedures in retrieving the Surface Temperature of Sea Ice

In summary, the retrieval of surface temperatures of sea ice using the IR channel of OLS is done by the following procedures:

- determining the ice concentration from SSM/I measurements,
- calculating the ice surface temperatures using OLS data with Eq. (3.5),
- correcting the atmospheric effects using Eq. (3.7).

This retrieval can also be done graphically in Figure 3.8, if the ice concentration and the OLS thermal infrared brightness temperature are given.

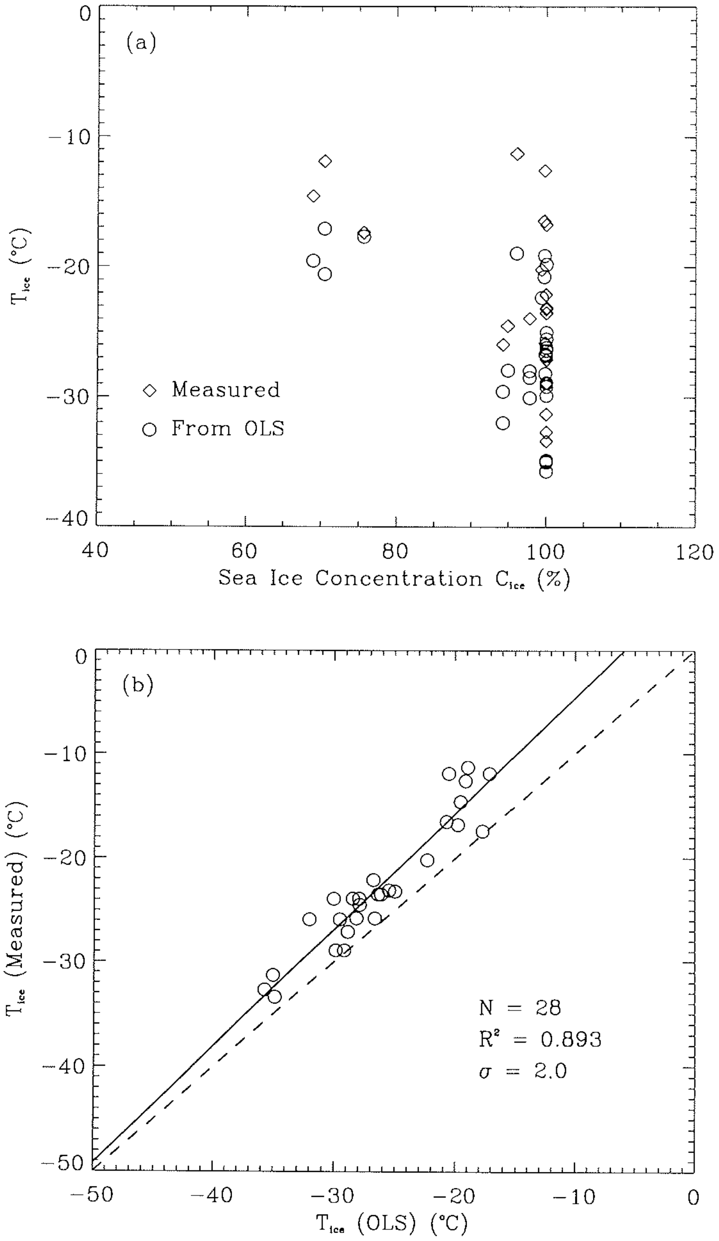

Figure 3.7: *(a) Measured and calculated (using Eq. 3.5) surface temperatures of sea ice versus ice concentration. (b) The relationship between the measured versus calculated ice surface temperatures in the Weddell Sea in July 1992.*

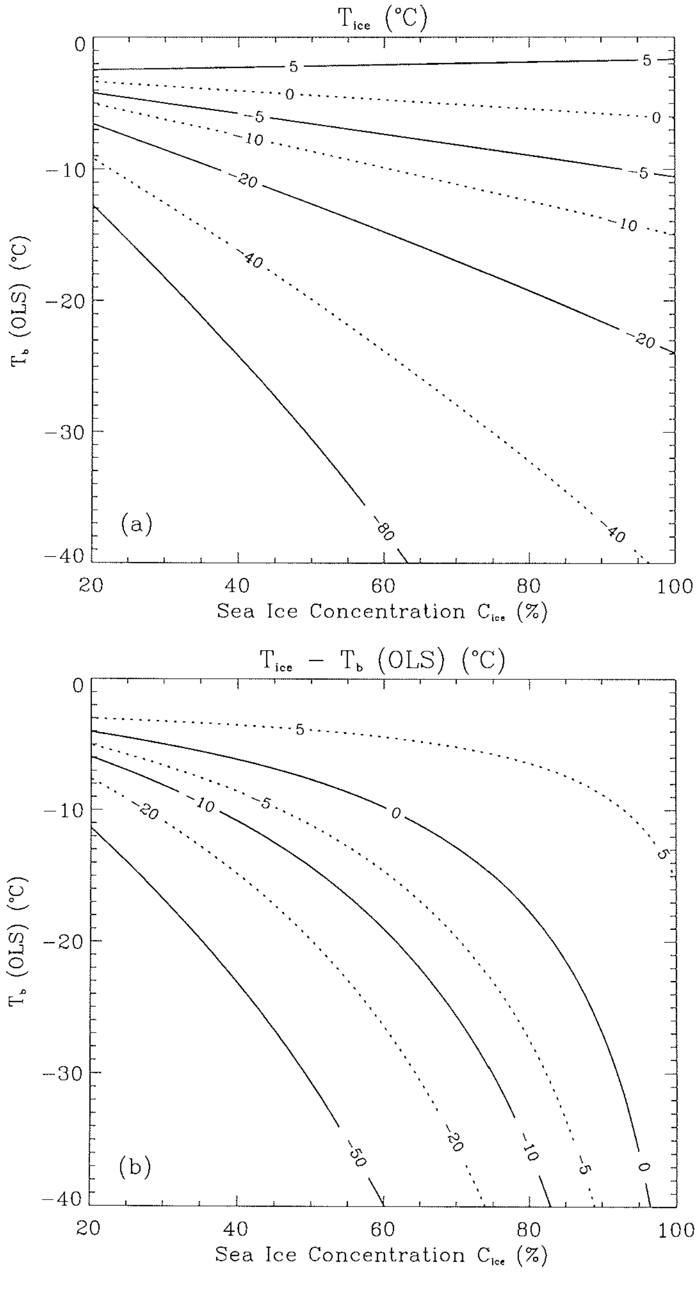

Figure 3.8: *Graphical retrieval of ice surface temperature. (a)* T_{ice} *and (b)* $T_{ice} - T_b(OLS)$ *as a function of* C_{ice} *and* $T_b(OLS)$.

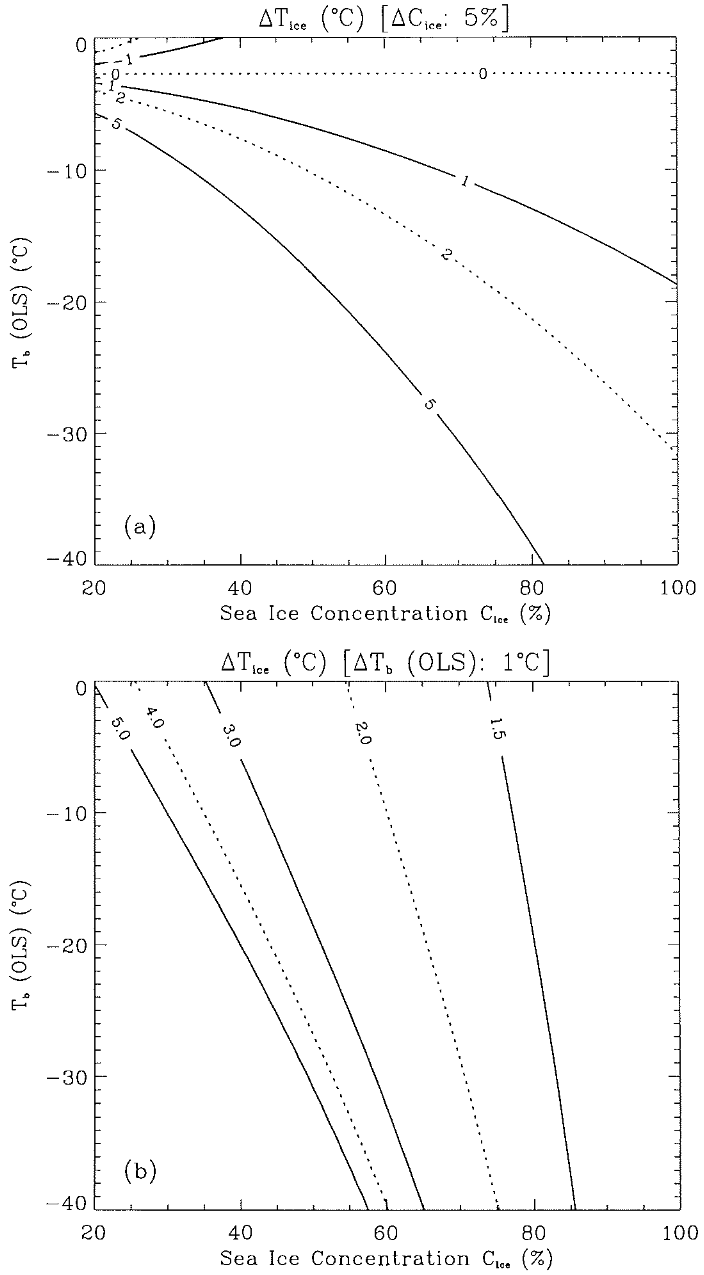

Figure 3.9: *The error of* T_{ice} *as a function of* C_{ice} *and* $T_b(OLS)$*, if (a)* C_{ice} *is determined with an error of 5% and (b)* $T_b(OLS)$ *is determined with an error of* $1.0\,K$*.*

3.2.2.5 Error Analysis

The accuracy of retrieving the surface temperature of sea ice following the procedure described above is determined by many factors, but mainly by the accuracies of the OLS measurements and the SSM/I determination of ice concentration. Figure 3.9 shows how errors from these two sources influence the accuracy of T_{ice}. Generally, the retrieval error is small in regions with high ice concentration, and for the same uncertainties in ice concentration determination and in OLS measurements, the retrieval deteriorates as the ice concentration and the surface temperature becomes low.

The influence of the atmosphere is another important error source. The effectiveness of Eq. (3.7) in correcting the atmospheric effects depends on whether the data set used to derive the coefficients is representative. Referring to Figure 3.7(a), it is not fully convincing to argue that the data set used here is fully representative. However, this correction formula can be demonstrated to be reasonable.

The sea ice surface temperature algorithms using AVHRR, given by *Massom and Comiso* [1994], can be regarded as an algorithm for regions of 100% ice coverage, since the resolution of AVHRR is much higher than that of SSM/I. This algorithm is designed for the Arctic and uses AVHRR channels 4 and 5,

$$T_{ice} = T4 + [1.246 - 8.717(T4 - T5)(\sec\theta - 1.0)] \text{ (K)}, \tag{3.8}$$

where $T4$ and $T5$ represent the brightness temperatures for channels 4 and 5, respectively, and θ is the local zenith angle. The term in the square brackets represents the correction due to the atmospheric absorption and ranges from 0 to 1.4 K, with an average of 0.7 K (*Massom and Comiso*, 1994). The algorithm developed in this section for OLS can be changed into an algorithm for AVHRR, by making use of the relationship (Eq. (3.6)) between brightness temperatures of the OLS IR channel and the AVHRR channel 4. If the ice concentration with the pixel is 100%, the algorithm for AVHRR channel 4 is simply written as

$$T_{ice} = 3.28 + 0.99T4 \text{ (K)}. \tag{3.9}$$

In comparing this equation with Eq. (3.8), it is found that the maximum difference between the two equations is 0.35 K for T_{ice} in the range of -50°–0°C. Note that, in comparing the Eqs. (3.8) and (3.9), the term in the square brackets of Eq. (3.8) is replaced by its average of 0.7 K.

3.2.3 Surface Temperature of Land Ice: Comiso's Formula

The retrieval of ice surface temperatures from infrared data over the continental ice sheet is simplified by its homogeneous snow coverage. The retrieval is also expected to be more accurate than over sea ice due to the very low water vapor content in the continental atmosphere. For convenience, the algorithm of *Comiso* [1994] is adopted. He analyzed the thermal infrared data of the Temperature Humidity Infrared Radiometer (THIR) on board the NIMBUS-7 satellite. NIMBUS-7 was also in a sun-synchronous polar orbit at an altitude of 955 km, which is close to the DMSP orbit; and THIR had a swath width of 3,000 km (*Kramer*, 1996). Because the thermal infrared channel of THIR worked in nearly same wavelength band (10.5–12.5 μm) as the OLS IR channel, the correction formula derived for the THIR can be directly used for OLS.

Comiso calculated the ice surface temperature using the equation,

$$T_{ice}(\mathrm{THIR}) = T_b(\mathrm{THIR})/(\bar{\epsilon}_s)^{1/4}, \tag{3.10}$$

in which $T_b(\mathrm{THIR})$ represents the brightness temperature at the thermal infrared channel of THIR and $\bar{\epsilon}_s$ is the snow emissivity with a value of 0.997. He compared the ice surface temperatures calculated using the above equation with those measured at Antarctic stations (see Figure 3.10). The station data include measurements in both austral summer (January) and winter (July). He found that the THIR and station temperatures were generally in agreement to within 3 K through out the year, with a correlation coefficient R of 0.997 and a standard deviation of 2.1 K. A linear regression of the data set provided the relationship,

$$\bar{T}_{ice}(\mathrm{Station}) = 14.2 + 0.946 T_{ice}(\mathrm{THIR})\ (\mathrm{K}). \tag{3.11}$$

$T_{ice}(\mathrm{THIR})$ is the ice surface temperature calculated using Eq. (3.10). It should be pointed out that (1) the station data were the 1–3m surface air temperatures instead of the skin temperature of the ice surface and (2) the comparison were done just between the monthly means of both measurements. According to *Comiso* [1994],

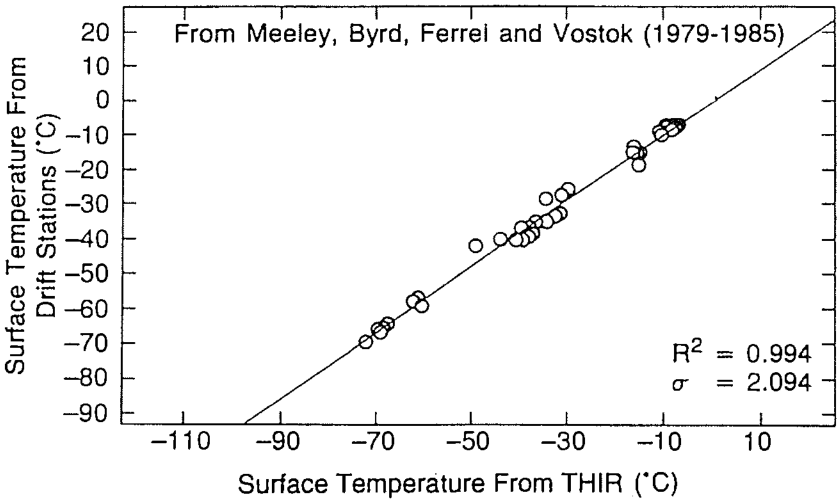

Figure 3.10: *Comparison of the monthly mean surface temperatures over the Antarctic ice sheet, measured at stations and retrieved from THIR data. (From Comiso [1994])*

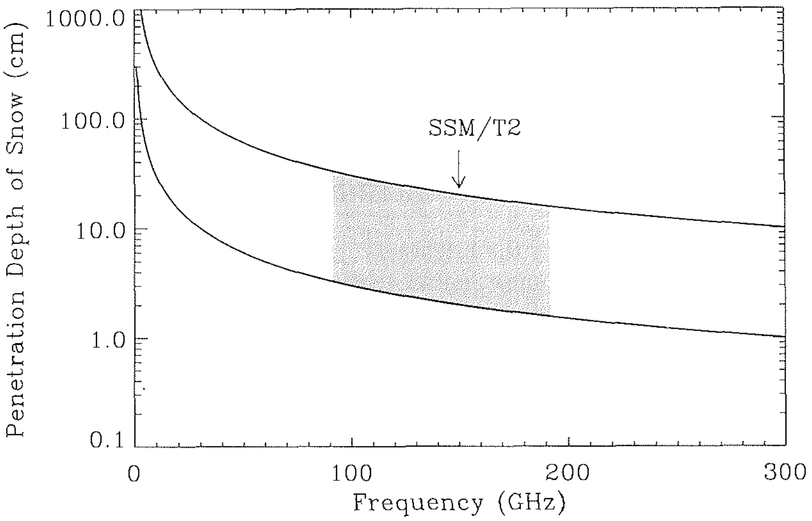

Figure 3.11: *The approximate range of the penetration depth of snow as a function of Frequency. The shaded area represents the ranges at SSM/T2 frequencies.*

the ice surface temperatures and the 1–3m surface air temperatures agree to within 1.0 K over the Antarctic continent. Considering the relatively stable water vapor content in the atmosphere over the Antarctic ice sheet, Eq. (3.11) shows the average effects of the atmospheric absorption and the surface emissivity variation on the retrieval of ice surface temperatures and is assumed to be valid for correcting these effects in the instantaneous measurements of OLS.

3.3 Emissivity of Ice at SSM/T2 Frequencies

3.3.1 The Microwave Emission from Snow Covered Ice

Snow covered ice (including both sea ice and land ice) is a bulk emitting medium at microwave frequencies below 300 GHz. According to *Hall and Martinec* [1985], the microwave emission of a snow cover can emanate from a depth of 10 to 100 times the length of the wavelength, depending upon the density, the liquid water content and the grain size of the snow. Figure 3.11 shows the approximate range of the penetration depth of snow at frequencies below 300 GHz. The penetration depth corresponds to a depth of the snow, over which radiation intensity reduces to e^{-2} ($\approx$14%) of its original value, and therefore, the radiation of the snow cover can be regarded just from its top layer with a thickness of the penetration depth. At the SSM/T2 frequencies the penetration depth of snow ranges from a few centimeter to a few decimeter, which falls in the range of the snow cover depth commonly encountered in the Antarctic oceans. The penetration depth of sea ice is much smaller than that of snow, less than one centimeter at frequencies above 100 GHz (*Ulaby et al.*, 1981), because the ice has a much higher density than snow and contains brine, which is a good absorber for microwaves. Therefore, the radiation of snow covered sea ice contains contributions from both the snow cover and the surface layer of ice, as shown in Figure 3.12. Normally, the temperature at the snow surface (T_s) and at the snow-ice interface (T_I) are different. This temperature difference is due to the heat transfer through ice and snow, which is in turn determined by the physical properties of ice and snow as well as by the meterological conditions at the surface. The *in situ* observations in the winter Weddell Sea has revealed that the snow surface temperature is always lower than the snow-ice interface temperature and the temperature gradient within the snow cover could be up to 1.5 K/cm, and this temperature gradient depends mainly on the snow surface temperature, the colder the snow surface, the larger the gradient (*Comiso et al.*, 1989).

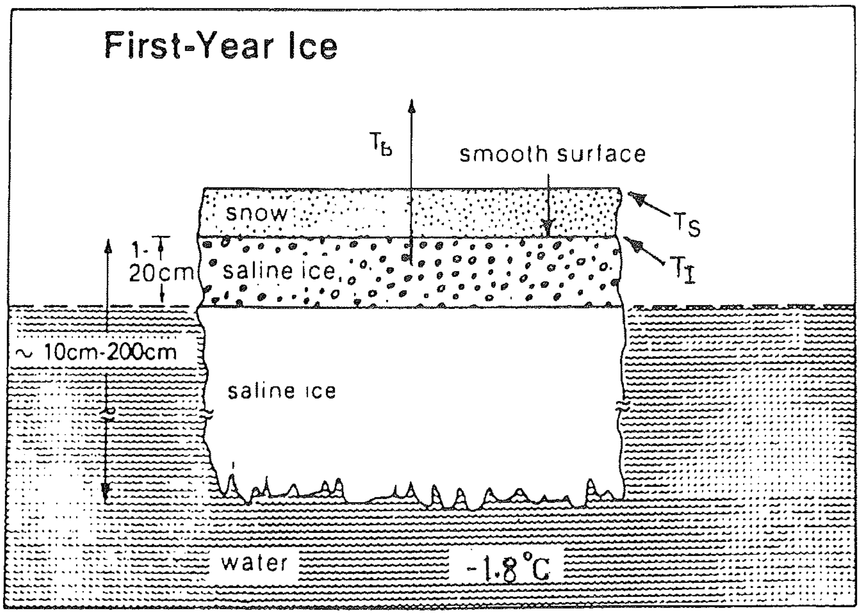

Figure 3.12: *The schematic diagram of the physical structure of first-year ice.*

Due to this nonuniform temperature distribution within the emitting layer, the effective emitting temperature of sea ice at microwave frequencies is in general different from the snow surface temperature. If the ice surface temperatures derived from measurements of infrared sensors are used to calculate the emissivities, the estimated values will overestimate the effective emissivities of sea ice. Over the Antarctic continent, however, the temperature gradient within the snow cover is much smaller (less than 0.1 K/cm (*Zwally*, 1977)), owing to the totally different physical conditions of the ice sheet. Hence, the land ice can be regarded as a grey body with constant temperature at the SSM/T2 frequencies. The effective emissivity of land ice can be exactly estimated using the surface temperatures from infrared measurements.

Many authors have investigated the emission properties of ice in polar regions. *Comiso et al.* [1989], *Grenfell et al.* [1994] and *Johnsen et al.* [1997] did *in situ* radiometric measurements directly above the ice surface; *Troy et al.* [1981] observed the polar ice using radiometers on board airplanes. Using satellite data, *Chang et al.* [1976] and *Comiso* [1983] have retrieved the surface emissivities of land and sea ice, respectively. But, these investigations were primarily done at frequencies below 40 GHz, although some observations at frequencies as high as 90 GHz were taken. Recently, measurements at frequencies up to 157 GHz over the Baltic sea ice and snow sites were done using airborne radiometers and valuable results were obtained (*Hewison and English*, 1998). Nevertheless, there is a general shortage of observations of ice emissivities at frequencies higher than 100 GHz, especially in Antarctica.

3.3.2 Methodology

Usually, the ground surface emissivity ϵ_s is retrieved by solving the integral radiative transfer equation (Eq. 2.12), when coincident measurements of the profiles of atmospheric temperature and humidity and the brightness temperature T_b at the top of the atmosphere are available. However, the sparse *in situ* measurements of the atmosphere in Antarctica often limited the use of this direct method. Since the range of surface emissivities of ice is needed in developing the algorithm for retrieving the total water vapor using the RCBTD method, a simple approach is proposed here to estimate the emissivities of ice, without coincident measurements of atmospheric profiles. This simple approach is also based on the integral radiative transfer equation, however, in a simplified form.

3.3.2.1 A Simple Expression of T_b

At first, the total transmissivity of the atmosphere at frequency f and local zenith angle θ, $\Upsilon(f,\theta)$, is defined

$$\Upsilon(f,\theta) = e^{-\int_0^H \alpha_a(f;z)\sec\theta dz}, \qquad 0 < \Upsilon < 1. \tag{3.12}$$

By substituting the expressions of the upwelling atmospheric radiation T_u (Eq. (2.13)), the downwelling atmospheric radiation T_d (Eq. (2.14)) and the surface emission T_e (Eq. (2.15)) into Eq. (2.12) and ignoring the contribution of the cosmic background, T_b has the form,

$$\begin{aligned} T_b(f,\theta) &= \epsilon(f,\theta)T_s\Upsilon(f,\theta) \\ &\quad +(1-\epsilon_s(f,\theta))\Upsilon(f,\theta)\int_0^H \alpha_a(f;z)T(z)e^{-\int_0^z \alpha_a(f;z)\sec\theta dz}\sec\theta dz \\ &\quad +\int_0^H \alpha_a(f;z)T(z)e^{-\int_z^H \alpha_a(f;z)\sec\theta dz}\sec\theta dz. \end{aligned} \tag{3.13}$$

On the right hand side of Eq. (3.13), the first term is the contribution of the ground surface emission and the next two terms are the contributions of atmospheric emission. By combining the atmospheric contributions together, T_b consists of two terms, the surface term and the atmospheric term. The atmospheric term in T_b can be further transformed into an integration, in which the integrand is a product of the temperature profile $T(z)$ and the so-called "temperature weighting function" $W_T(f, \theta; z)$. T_b is then expressed as

$$T_b(f, \theta) = \epsilon(f, \theta) T_s \Upsilon + \int_0^H W_T(f, \theta; z) T(z) dz. \tag{3.14}$$

$W_T(f, \theta; z)$ is given by

$$\begin{aligned} W_T(f, \theta; z) \; = \; & [(1 - \epsilon_s(f, \theta)) \Upsilon(f, \theta) \alpha_a(f; z) e^{-\int_0^z \alpha_a(f;z) \sec\theta dz} \\ & + \alpha_a(f; z) e^{-\int_z^H \alpha_a(f;z) \sec\theta dz}] \sec\theta. \end{aligned} \tag{3.15}$$

The atmospheric term in Eq. (3.14) can be further simplified to a product of integrated quantities. For this purpose, we define a quantity, the "equivalent temperature of the atmosphere", T_a,

$$T_a = \frac{\int_0^H W_T(f, \theta; z) T(z) dz}{\int_0^H W_T(f, \theta; z) dz}. \tag{3.16}$$

If we further define the quantity $W_a(f, \theta)$

$$W_a(f, \theta) \; = \; \int_0^H W_T(f, \theta; z) dz \tag{3.17}$$

as the atmospheric weight, the expression of T_b then has the following simple form,

$$T_b(f, \theta) \; = \; \Upsilon \epsilon_s(f, \theta) T_s + W_a(f, \theta) T_a. \tag{3.18}$$

Clearly, the surface weight is equal to the atmospheric transmissivity Υ.

If the integration in Eq. (3.17) is performed by using the expression of the temperature weighting function $W_T(f, \theta; z)$ in Eq. (3.15), it is found that the atmospheric weight W_a has the following simple algebraic form,

$$W_a \; = \; (1 - \Upsilon) + (1 - \epsilon_s)(1 - \Upsilon)\Upsilon. \tag{3.19}$$

In performing this integration, the condition

$$\alpha_a(f; H) = 0 \tag{3.20}$$

has been considered, which means that the atmospheric absorption becomes zero at the top of the atmosphere. For clarity, the arguments f and θ are omitted in Eq. (3.19). Taking the simple algebraic form of W_a, the expression of T_b becomes

$$T_b = \Upsilon \epsilon_s T_s + [(1 - \Upsilon) + (1 - \epsilon_s)(1 - \Upsilon)\Upsilon] T_a. \tag{3.21}$$

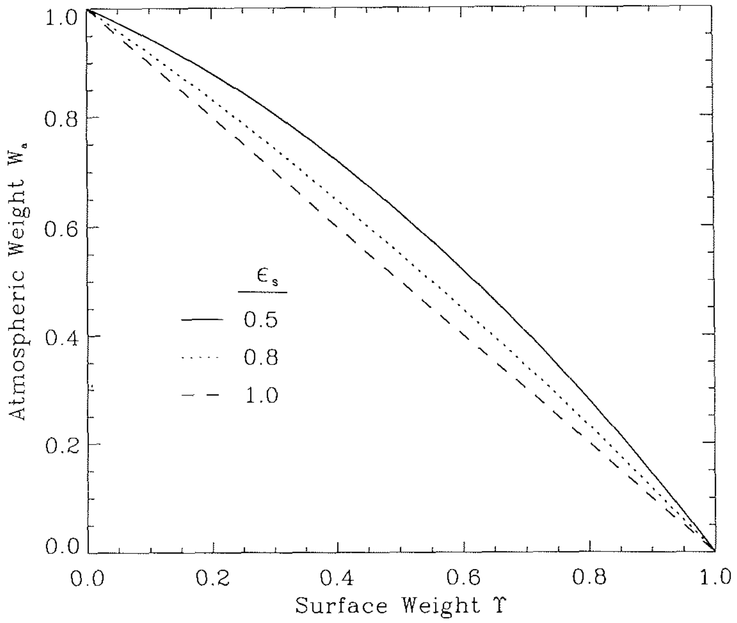

Figure 3.13: *The relationship between the surface weight* Υ *and the atmospheric weight* W_a *for non-scattering atmospheres.*

An interesting relation exists between the surface weight and the atmospheric weight W_a, *i.e.*

$$\Upsilon + W_a = 1 + (1 - \epsilon_s)(1 - \Upsilon)\Upsilon. \tag{3.22}$$

This relationship is also graphically shown in Figure 3.13. Clearly, the sum of Υ and W_a is very close to 1, since the second term on the right hand side of Eq. (3.22) is small for the emissivities of commonly encountered surfaces. This relationship reveals an important fact for satellite radiometry. When the atmospheric absorption increases due to the increase of water vapor content in the atmosphere or liquid water content in clouds, the atmospheric transmissivity Υ will decrease; consequently, the contribution of the surface emission in the measured T_b will decrease. However, the reduced surface contribution in T_b tends to be compensated by almost the same proportion of the atmospheric emission. As a result, the final change of T_b depends directly on the contrast (the difference) between the surface emission $\epsilon_s T_s$ and the equivalent atmospheric temperature T_a. If T_a is very close to $\epsilon_s T_s$, changing the atmospheric absorption has very little effect on the measured T_b; this means, variations of the atmospheric parameter cannot be observed in the measured T_b. Therefore, a sufficiently large contrast between the surface emission $\epsilon_s T_s$ and the equivalent atmospheric temperature T_a is the prerequisite to measure the atmospheric parameters using satellite radiometry. Since both the ground surface emissivity and the equivalent atmospheric temperature are functions of frequency, the operating frequencies of a radiometer must be carefully selected.

3.3.2.2 The Atmospheric Transmissivity Υ and the Equivalent Atmospheric Temperature T_a

The simple expression of T_b in Eq. (3.21) is used to estimate the surface emissivity of ice. Algebraic manipulation of this equation to solve for the surface emissivity yields

$$\epsilon_s = \frac{\frac{T_b}{T_s} - \frac{T_a}{T_s}(1 - \Upsilon^2)}{\Upsilon[1 - \frac{T_a}{T_s}(1 - \Upsilon)]}. \tag{3.23}$$

In this equation, T_b is obtained directly from the measurements of SSM/T2 and T_s can be retrieved from OLS data in cases of clear sky. The quantities Υ and T_a, however, need to be estimated. Υ depends on the absorption of gas in the atmosphere, at SSM/T2 frequencies, mainly water vapor. If the temperature dependency of water vapor absorption is ignored, Υ is directly related to W, the total water vapor in the atmosphere. The equivalent atmospheric temperature T_a, in contrast, depends mainly on the vertical structure of temperature and water vapor in the atmosphere (see Eq. (3.16)). Referring to Eq. (3.23), only the ranges of Υ and $\frac{T_a}{T_s}$ are needed in order to estimate the range of the surface emissivities. If the minima and maxima of Υ and $\frac{T_a}{T_s}$ in a region for a given season can be estimated, the range of surface emissivity is determined by the corresponding minimum and maximum of ϵ_s in Eq. (3.23),

$$(\epsilon_s)_{\min} = \epsilon_s|_{(\Upsilon_{\min},(\frac{T_a}{T_s})_{\max})} \tag{3.24}$$

$$(\epsilon_s)_{\max} = \epsilon_s|_{(\Upsilon_{\max},(\frac{T_a}{T_s})_{\min})}. \tag{3.25}$$

To estimate the ranges of Υ and $\frac{T_a}{T_s}$ in Antarctic winter, model simulations were done using typical atmospheric profiles measured with radiosondes at representative locations. Figure 3.14 shows the atmospheric profiles used in this simulation, which are expected to represent the typical conditions of the atmosphere in austral winter at the continental interior, at the coast, and over the sea ice covered oceans. In doing the simulation the relative humidity at all levels in the troposphere is assumed to be same, changing from 0% to 100% in steps of 10%. The simulated results of Υ as a function of the total water vapor W are shown in Figure 3.15. Here, only the results at the three lower channels of SSM/T2 are shown. Due to the strong absorption of water vapor for the 183.31 GHz channels of SSM/T2, the atmospheric transmissivity at these channels decreases rapidly with increasing total water vapor. For example, for $4.0\,\mathrm{kg/m^2}$ of total water vapor the transmissivity is only about 0.5 for the 183.31±7 GHz channel. In contrast, the transmissivity is at least 0.8 for the two window channels of SSM/T2, even for total water vapor up to $8.0\,\mathrm{kg/m^2}$. Because water vapor is the main absorber at SSM/T2 frequencies, Υ is approximated as a simple function of the total water vapor W,

$$\Upsilon = e^{-\tau_d - \kappa_v W}, \tag{3.26}$$

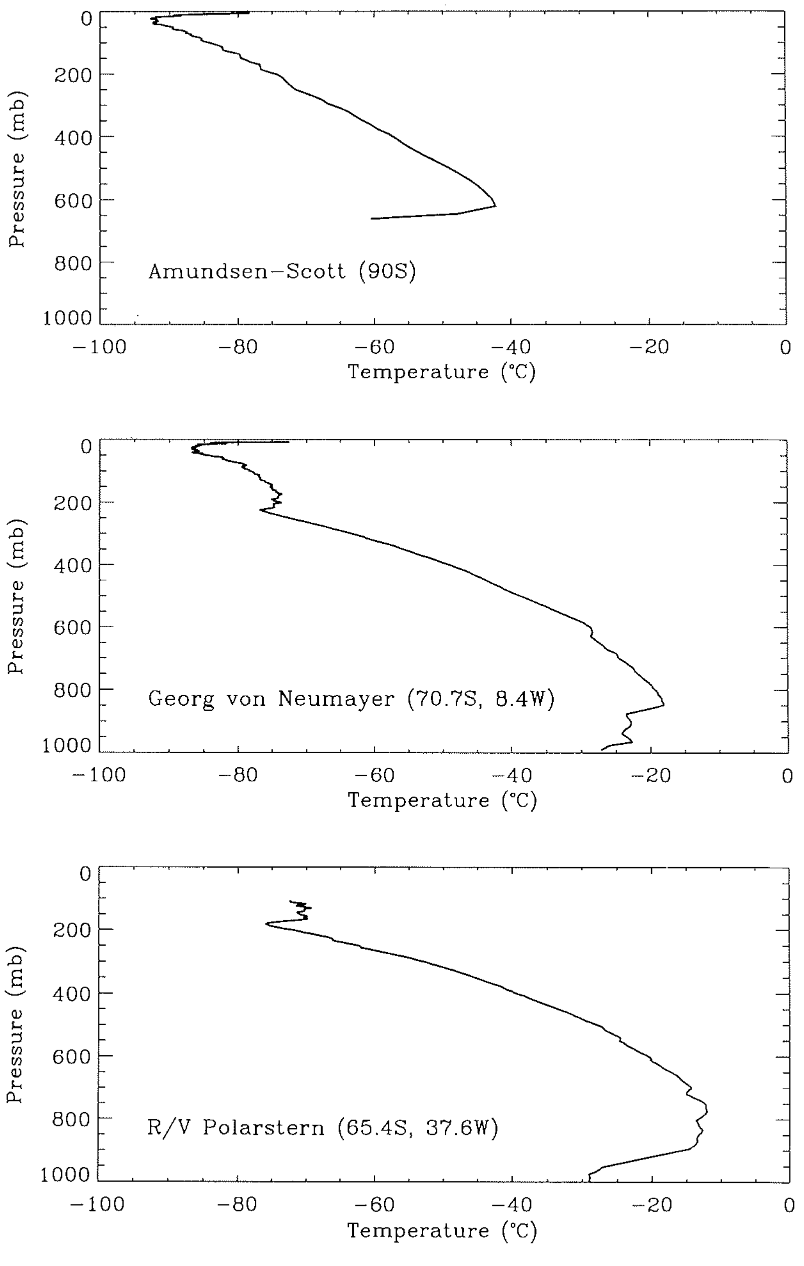

Figure 3.14: *The temperature profiles used for estimating the ranges of* Υ *and* $\frac{T_a}{T_s}$ *in the Antarctic winter. All of the profiles are measured with radiosonde.*

Table 3.2: τ_d and κ_v for SSM/T2 channels in the Antarctic winter

Channel Number	1	2	3	4	5
τ_d	0.008	0.016	0.019	0.035	0.066
κ_v	0.009	0.027	0.156	0.525	1.249

where κ_v is the mass absorption coefficient of water vapor defined in Chapter 2 and τ_d stands for the total absorption of all the other gases except water vapor in the atmosphere. Using the simulated results of Υ, κ_v and τ_d can be determined with regression procedures, and the corresponding values at the five channels of SSM/T2 are given in Table 3.2. At the same time, the ratio of $\frac{T_a}{T_s}$ are also obtained from the simulation and they are shown in Figure 3.16.

In view of the significant difference in climatology over the Antarctic continent and over the circumpolar oceans, they are treated separately. Using Eq. (3.26), Υ can be immediately calculated if the total water vapor W is given. Over the continental ice sheet in austral winter, the total water vapor in the atmosphere is assumed to be not more than 1.0 kg/m^2; but, the ratio $\frac{T_a}{T_s}$ could be large due to strong surface temperature inversions and it is assumed to be in the range of $1.0 \cdots 1.2$, in view of the simulated results in Figure 3.16. The atmosphere over sea ice generally contains more water vapor due to its evidently higher air temperatures.

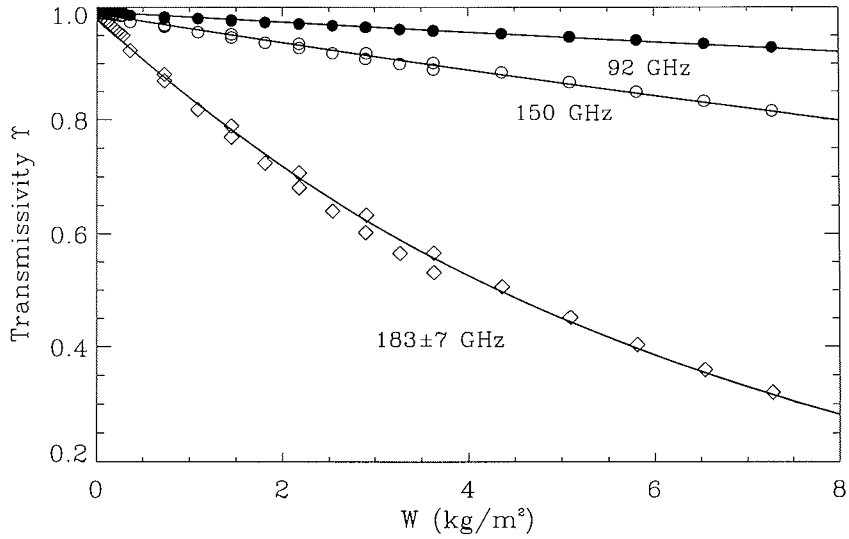

Figure 3.15: *The atmospheric transmissivity Υ at the three lower frequency channels of SSM/T2 versus total water vapor W. The symbols represent the simulated results based on radiosonde data, while the solid lines represent the fits using Eq. (3.26).*

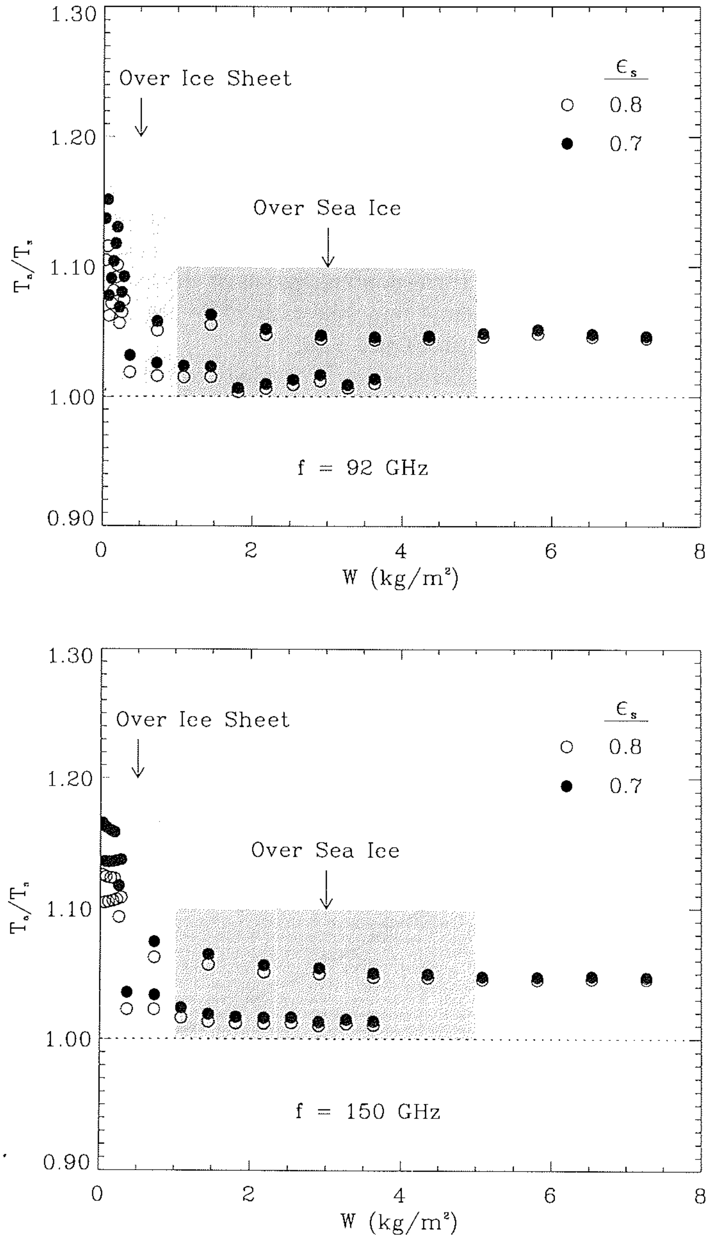

Figure 3.16: *Simulated* $\frac{T_a}{T_s}$ *versus total water vapor* W *at 92 GHz (top) and 150 GHz (bottom). The shaded areas represent the estimated ranges of* W *and* $\frac{T_a}{T_s}$ *in the Antarctic winter.*

Table 3.3: Estimated ranges of W and $\frac{T_a}{T_s}$ in the Antarctic winter

Region	W (kg/m^2)	$\frac{T_a}{T_s}$
Over Ice Sheet	$0.0 \cdots 1.0$	$1.0 \cdots 1.2$
Over Sea Ice	$1.0 \cdots 5.0$	$1.0 \cdots 1.1$

Hence, W over sea ice is assumed to be in the range of $1.0 \cdots 5.0\,\mathrm{kg/m^2}$ for clear sky conditions. The ratio $\frac{T_a}{T_s}$ in sea ice covered regions, in contrast, is expected to be smaller than that over the continent, since the surface temperature inversion is weaker. The simulated results of $\frac{T_a}{T_s}$ shown in Figure 3.16 give a rough guide-line in estimating the range of $\frac{T_a}{T_s}$. Normally, most of the water vapor is constrained within the lower and warm layer of the atmosphere. Due to the prevailing surface temperature inversion in Antarctica, especially in winter, the equivalent temperature of the atmosphere is expected to be higher than the surface temperature. The rough range of $\frac{T_a}{T_s}$ over sea ice is assumed to be within the range of $1.0 \cdots 1.1$. In summary, the estimated ranges of W and $\frac{T_a}{T_s}$ in austral winter are given in Table 3.3. These values will be used to estimate the range of surface emissivity of ice using satellite data.

3.3.2.3 The Relationship between Surface Emissivity ϵ_s and Ratio $\frac{T_b}{T_s}$

As stated above, given the ranges of Υ and $\frac{T_a}{T_s}$, the range of the surface emissivity ϵ_s can be immediately determined using Eqs. (3.23), (3.24) and (3.25) for a given value of $\frac{T_b}{T_s}$. Because $\frac{T_a}{T_s}$ is assumed to be larger than 1 in the Antarctic winter, $\frac{T_b}{T_s}$ always overestimates the surface emissivity ϵ_s. Figures 3.17 shows the range of ϵ_s of both land and sea ice at the two window channels of SSM/T2 for a given value of $\frac{T_b}{T_s}$. Clearly, the more sensitive a channel is to water vapor, the larger the uncertainty in the estimate of ϵ_s at this channel will be. $\frac{T_b}{T_s}$ gives the best estimate of ϵ_s at 92 GHz over the Antarctic continent and the worst estimate at 150 GHz over sea ice regions. The error in estimating ϵ_s of sea ice using $\frac{T_b}{T_s}$ at the 150 GHz channel can be larger than 0.1 (see Fig. 3.17). If the measurements at the 183.31 GHz channels are used, much larger uncertainties are expected. These large uncertainties make the estimation meaningless. Therefore, just the two window channels of SSM/T2 are used in the following discussions.

3.3.3 Results from Satellite Data

In general, the surface emissivity of ice is a function of both the satellite viewing angle and the polarization state. As stated in Chapter 1, both the viewing angle and the polarization state of SSM/T2 changes during a scan. Therefore, the equivalent surface emissivity for SSM/T2 changes with the beam position, which should be considered when estimating the surface emissivity. However, the surface emissivities of the terrestrial surfaces at two orthogonal polarizations change differently with the viewing angle. Figure 3.18 shows the theoretical emissivities of calm ocean surfaces as a function of the local zenith angle θ, at vertically polarized (V) and horizontally

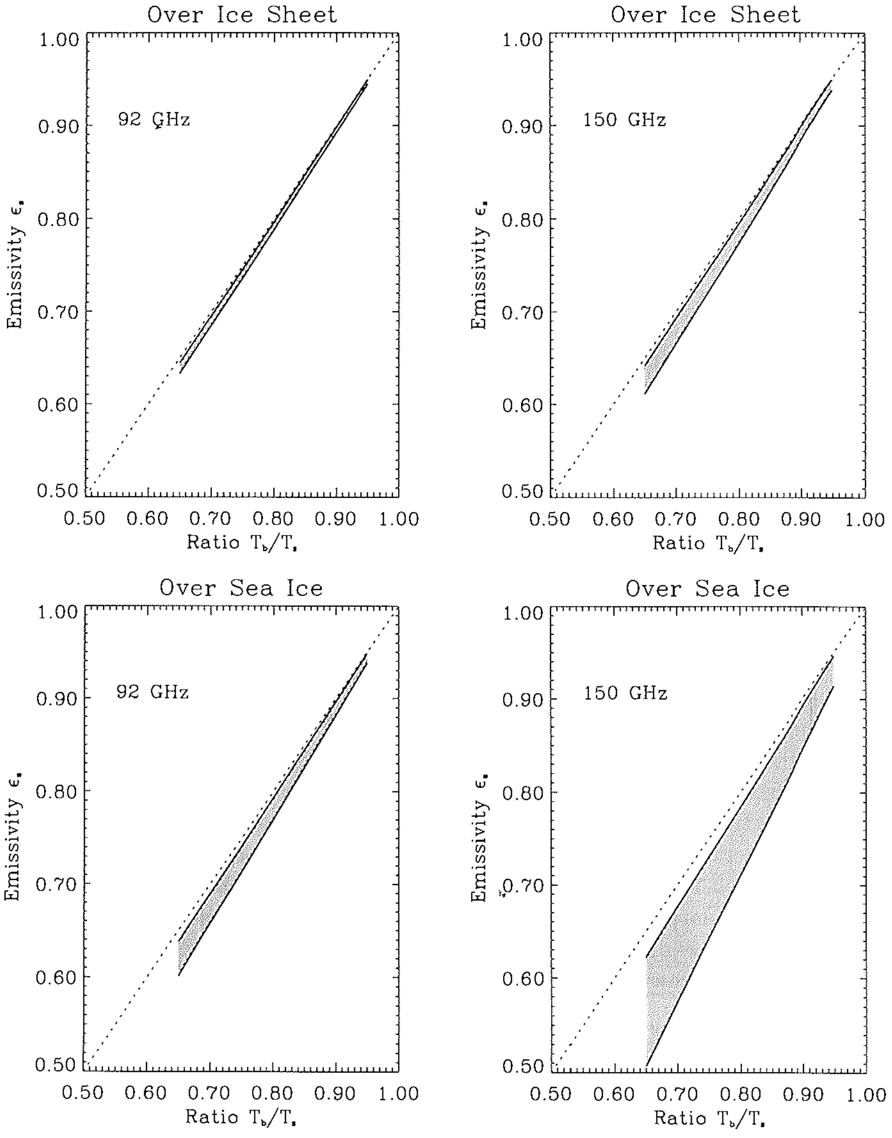

Figure 3.17: *The range of* ϵ_s *at a definite value of* $\frac{T_b}{T_s}$ *at frequencies of 92 GHz (left) and 150 GHz (right) over the ice sheet (top) and over sea ice (bottom).*

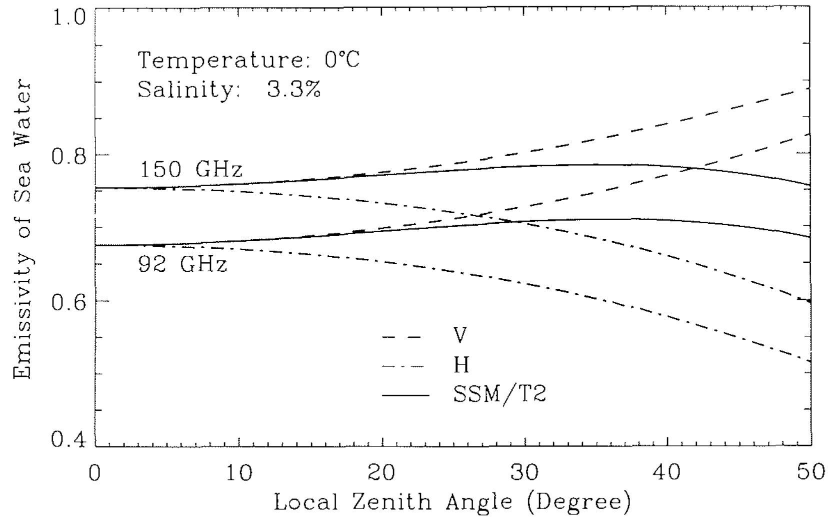

Figure 3.18: *The theoretical emissivity of calm ocean surfaces, calculated using the Fresnel formula for specular surfaces and the dielectric constant of sea water given by Klein and Swift [1977].*

polarized directions. The difference between ϵ_s at the two polarizations tends to increase rapidly with increasing local zenith angle θ. However, the equivalent emissivity of SSM/T2 changes much smaller with θ, due to the mixed polarization of SSM/T2 receiver (see also Fig. 3.18 and Fig. 1.3). Based on this fact, the viewing angle dependency of the equivalent SSM/T2 emissivities of ice are not considered in the following discussions.

The coincident measurements of SSM/T2 and OLS at 25 and 26 of July 1995 are used for the following analysis. There is a total of 29 overpasses of spacecraft F12 in these two days. Since the swath width of OLS is large, about 3,000 km, two consecutive images of OLS in polar regions overlap one another significantly. In addition, the period of the DMSP satellites is about 101 minutes. Hence, when these images are shown consecutively, the movement of clouds can be clearly observed and cloud-free regions are better recognized than with only one image. Over the two days, most parts of Antarctica were covered by clouds, especially in the coastal regions. Over sea ice, cloud-free patches were observed in the center Weddell Sea, the Amundsen Sea and the Ross Sea. Over the Antarctic plateau, part of Queen Maud land and part of Wilkes land were recognized as cloud-free. An example of the coincident images of OLS and SSM/T2 is shown in Figure 3.19, in which the rectangles represent regions recognized as cloud-free. The SSM/T2 pixels within these rectangles will be selected to estimate the surface emissivities of ice. In calculating $\frac{T_b}{T_s}$, T_b is directly taken from the SSM/T2 measurements and T_s is retrieved from OLS measurements using the algorithms described in Section 3.2. The sea ice

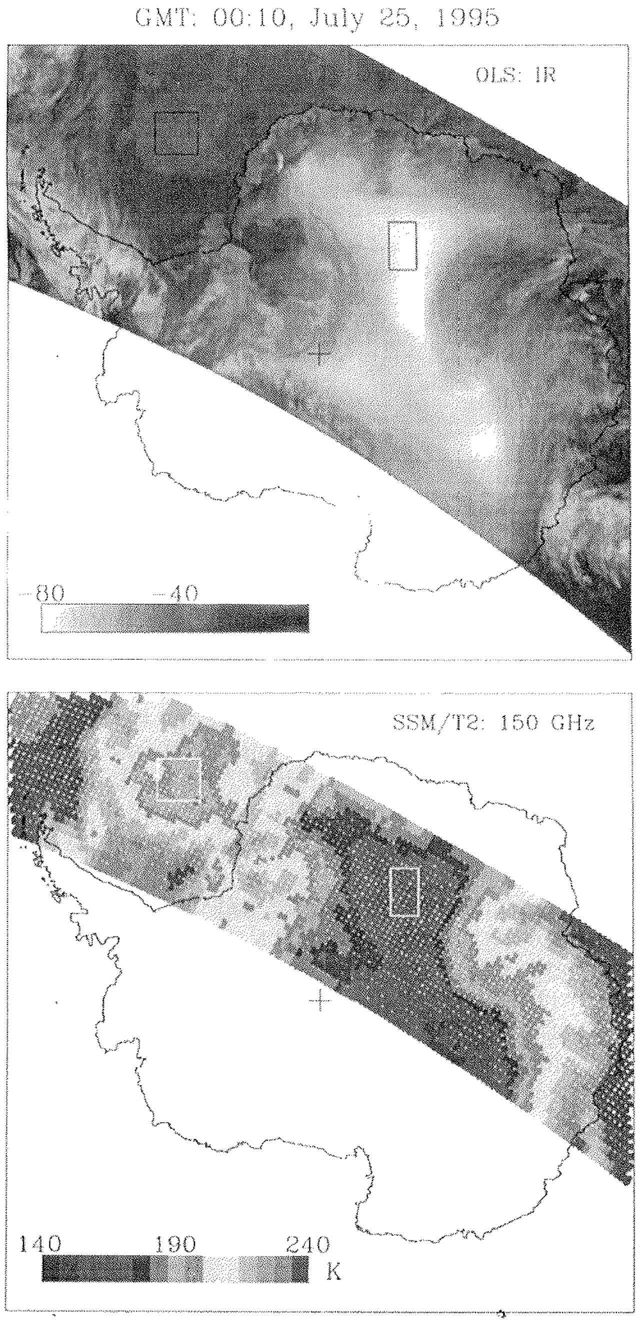

Figure 3.19: *An example of the coincident measurements of SSM/T2 and OLS, used for ice emissivity estimations. The rectangles represent the selected cloud-free regions.*

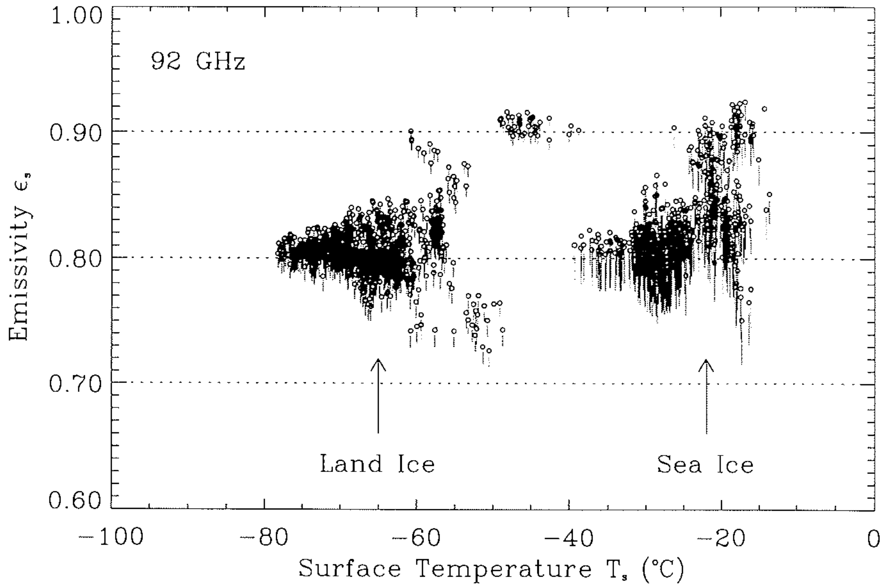

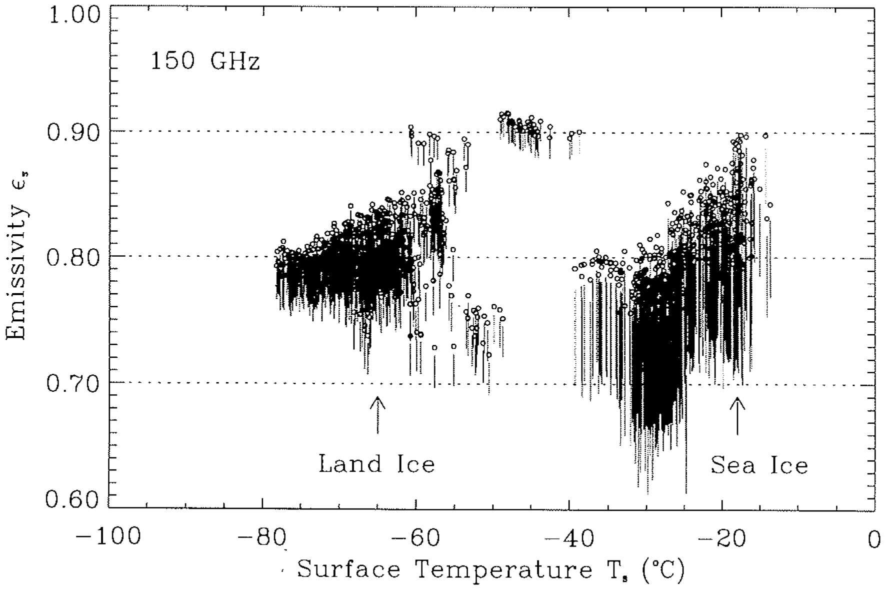

Figure 3.20: *Estimated emissivities of land ice and sea ice at 92 GHz (top) and at 150 GHz (bottom). The small open circles represent the values of* $\frac{T_b}{T_s}$*; the dotted lines below the circles represent the corresponding range of the surface emissivity* ϵ_s.

concentration in sea ice regions was obtained from the coincident SSM/I measurements. It was found that, in most of the selected regions, the ice concentration was higher than 95%. Since OLS has a much higher resolution (5 km) than SSM/T2, the surface temperatures used to calculate $\frac{T_b}{T_s}$ were averages over the SSM/T2 footprints.

The final results of the estimation of ice surface emissivities using satellite data are shown in Figure 3.20. The emissivities of both land and sea ice at 92 and 150 GHz are within the range of $0.65 \cdots 0.90$. At 150 GHz, the emissivities of both types of ice are lower than at the 92 GHz. The decrease of the ice surface emissivity with increasing frequency is usually explained by volume scattering of snow that covers the ice. However, the large difference between the surface emissivities at 92 GHz and 150 GHz for sea ice cases may be also related to the large temperature gradient within the snow cover of sea ice. Since the loss of radiation due to the volume scattering and the absorption of the snow cover generally increases with increasing frequency, a larger portion of the radiation received by a spaceborne radiometer originates from the top layer of the snow cover at the higher frequency. Since the top layer of the snow cover is always colder than the bottom layer for sea ice cases, as pointed by *Comiso et al.* [1989], the effective emitting temperature of the snow covered sea ice at 150 GHz is lower than at 92 GHz; consequently, lower surface emission and smaller surface emissivity.

Chapter 4

Algorithm for the Antarctic Region

Based on the knowledge of surface emissivity of ice as discussed in Chapter 3, an algorithm is described in this chapter using the RCBTD method to retrieve the atmospheric water vapor content in Antarctica. To determine the coefficients used in the algorithm, a linear regression procedure is used based on the data set of total water vapor obtained from radiosonde soundings, and the corresponding brightness temperatures at SSM/T2 frequencies calculated using a radiative transfer model. The sensitivity of the algorithm to errors in the SSM/T2 measurements is analyzed and the algorithm is validated using independent radiosonde soundings. The effects of clouds on the retrieval are examined through model simulations in the last section of this chapter.

4.1 Data Set of Radiosonde Soundings

The vertical distribution of temperature, pressure and humidity in the polar atmosphere up to an altitude of about 30 km are routinely measured by radiosondes, once or twice per day, at Antarctic stations; most of these stations are located along the Antarctic coast. Over the vast circum-polar oceans, the upper-air data are mainly obtained from occasional soundings of radiosondes launched from research vessels or ships supplying the Antarctic bases.

The available upper-air data in this study contain three groups of soundings. The first group consists of soundings made in the Weddell Sea during June and July in 1992 from the research vessel R/V Polarstern during its expedition "Winter Weddell Gyre Study" (WWGS) across the Weddell Sea. During the two months radiosondes were launched four times a day producing a total to 156 usable soundings. The second group is composed of soundings launched in June and July from 1990 to 1994 at the Antarctic station Georg von Neumayer (8.4°W, 70.7°S). This group contains 294 soundings. The soundings in the third group were made at the Amundsen-Scott station at the South Pole (90°S) in 1993, using NOAA ozonesondes. Because there were initially only 9 soundings in the third group, which were launched in the period June and July, the soundings from March to October are include to expand

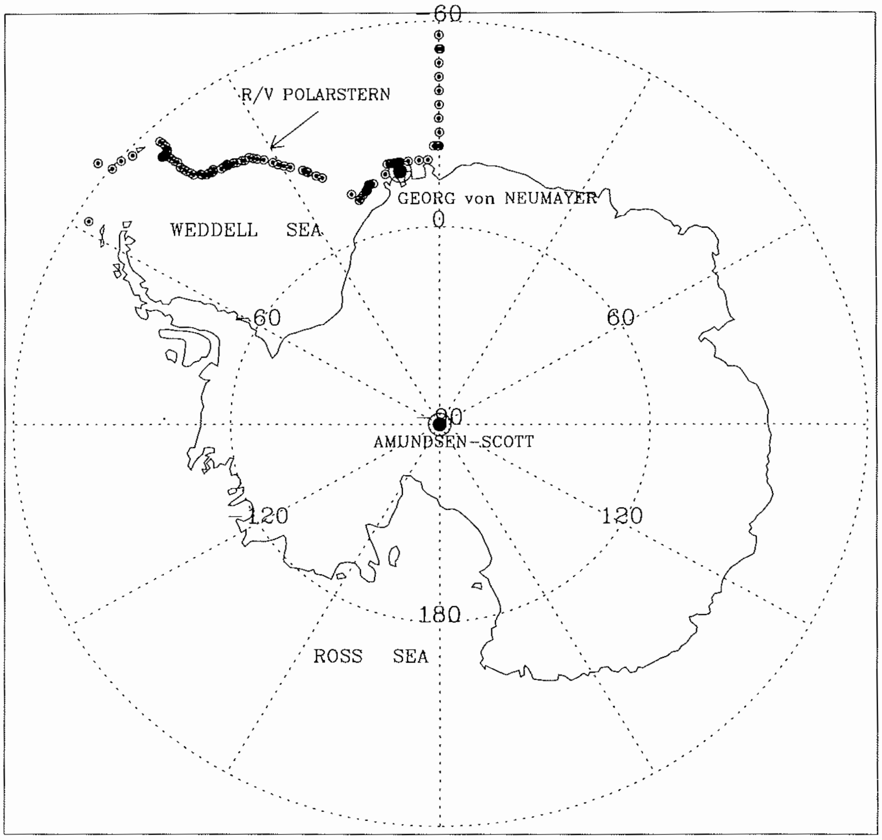

Figure 4.1: *The locations of the available radiosonde soundings in the Antarctica.*

the number of usable soundings at the South Pole to 52. The locations of these three groups of soundings are shown in Figure 4.1. The total of 502 available soundings, measured in the sea ice covered ocean, the Antarctic coast and the continental interior, should reflect the typical conditions of the Antarctic atmosphere in the austral winter, with the exception of the soundings at the South Pole, which also contain some soundings made in the austral spring and fall.

To develop the algorithm, the data set is divided into two groups: regression group and test group. Each group has 251 soundings with equal numbers of soundings from the mentioned three sources. The regression group is used to construct the algorithm and the test group is used to validate it. The histograms of the total water vapor, the surface air temperature and the surface pressure of the atmospheres corresponding to the regression and test groups of soundings are shown in Figure 4.2. The atmosphere over the Antarctic plateau differs distinctly from the atmospheres over the coast and over the ocean by its low surface pressure and

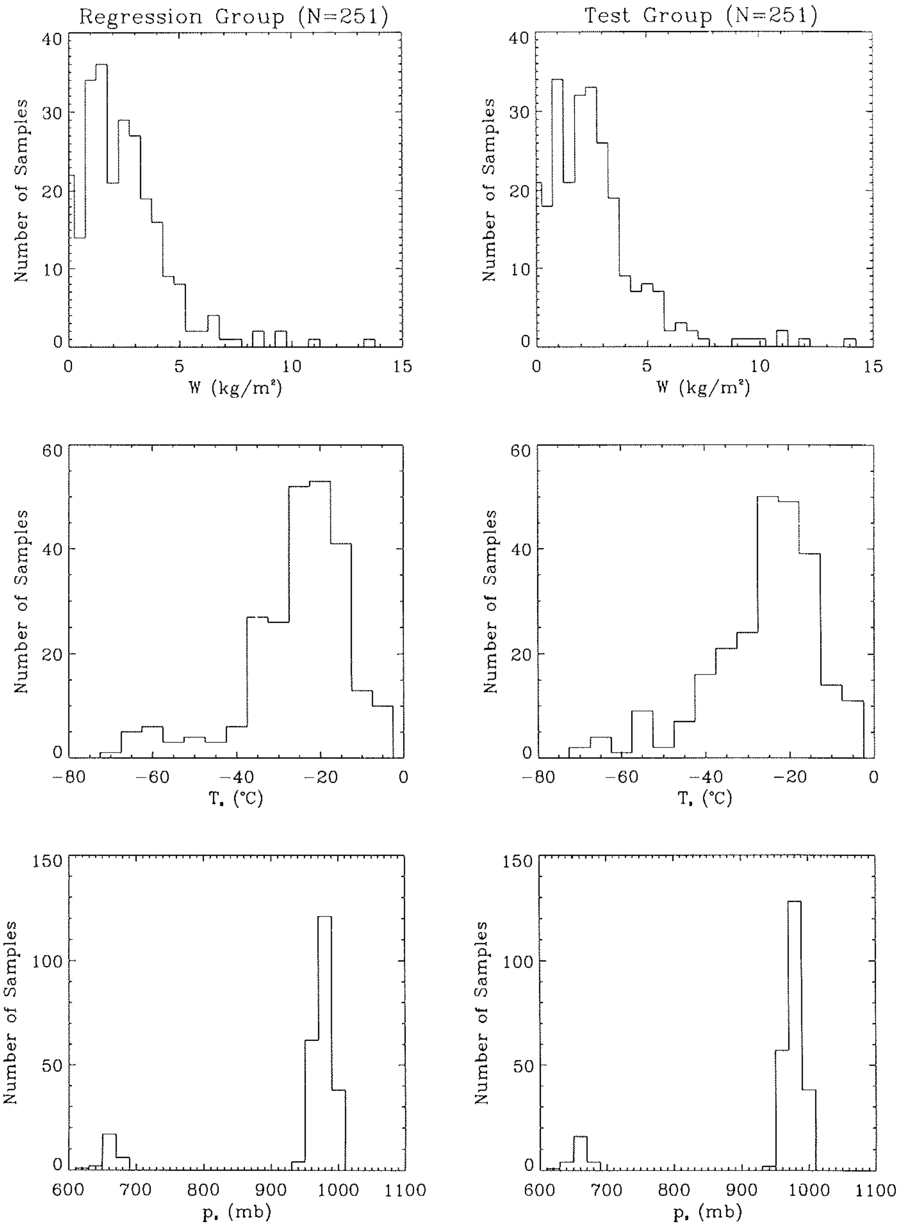

Figure 4.2: *The histograms of total water vapor in the atmosphere, surface air temperature and surface pressure used for the regression group (left) and the test group (right).*

low surface air temperature. The atmosphere there is very dry; mostly it contains less than 5.0 kg/m^2 water vapor. Given the temperature and humidity profiles, the total water vapor W is calculated using Eq. (2.26), which is an integration of water vapor density from the ground surface to the top of the atmosphere along a zenith path. The water vapor density ρ_v is calculated using the ideal gas equation,

$$\rho_v = RH\frac{e_{v,s}}{R_v T}, \tag{4.1}$$

in which R_v is the gas constant for 1 kg of water vapor in unit of J·deg^{-1} ·kg^{-1}; T and RH are the local temperature (in Kelvin) and relative humidity (in percent) of the atmosphere, respectively. The saturation water vapor pressure (in mb) $e_{v,s}$ depends only on the temperature and is given by (*Foerster*, 1997),

$$e_{v,s} = 6.1078\exp(\frac{4665.63 - 17.08T}{38.98 - T}). \tag{4.2}$$

4.2 Algorithm Developed from Model Results

4.2.1 Virtual Measurements of SSM/T2

The virtual measurements of SSM/T2, *i.e.* the brightness temperatures at all SSM/T2 channels, corresponding to the data collected by radiosondes are calculated using the radiative transfer model MWMOD. Given the atmospheric temperature and humidity profiles, the brightness temperatures at all SSM/T2 channels are calculated for a series of surface emissivities and local zenith angles. Since there were no simultaneous measurements of the ice surface temperature, the air temperature at the lowest level (normally 10 m above surface) of each profile was used as the ice surface temperature to calculate the surface emission in the model. The surface emissivities of ice are assumed to change from 0.68 to 0.92 in steps of 0.04, based on the knowledge learnt in Chapter 3. In Chapter 1 we have mentioned that SSM/T2 has 28 scan positions with 14 different scan angles. For simplicity, the simulations were not done for every scan position, instead, they were done only at 6 typical positions, with the local zenith angles of 1.7 °, 8.49 °, 18.73 °, 29.13 °, 36.22 °, and 47.26 °. As an example, the simulated brightness temperature differences between neighboring channels of SSM/T2 with the local zenith angle of 1.7 ° are shown in Figure 4.3. According to the discussions on the saturation point in Section 2.2.4, we find that the corresponding saturation points at channels 5 and 4 in this case to be about 1.5 kg/m^2 and 4.0 kg/m^2, respectively. Clearly, this saturation point is not constant, changing with surface emissivities. In Figure 4.4, the same simulated results are shown again in the plane of brightness temperature differences $T_3 - T_4$ and $T_2 - T_3$. After the biases are exactly compensated, the relationship between RCBTD η_c and total water vapor W is very close to logarithmic, as can be seen in the bottom part of this plot. Once again, the simple relationship between η_c and W, as given by Eq. (2.38) derived in Chapter 2, is demonstrated by these simulations using radiosonde soundings.

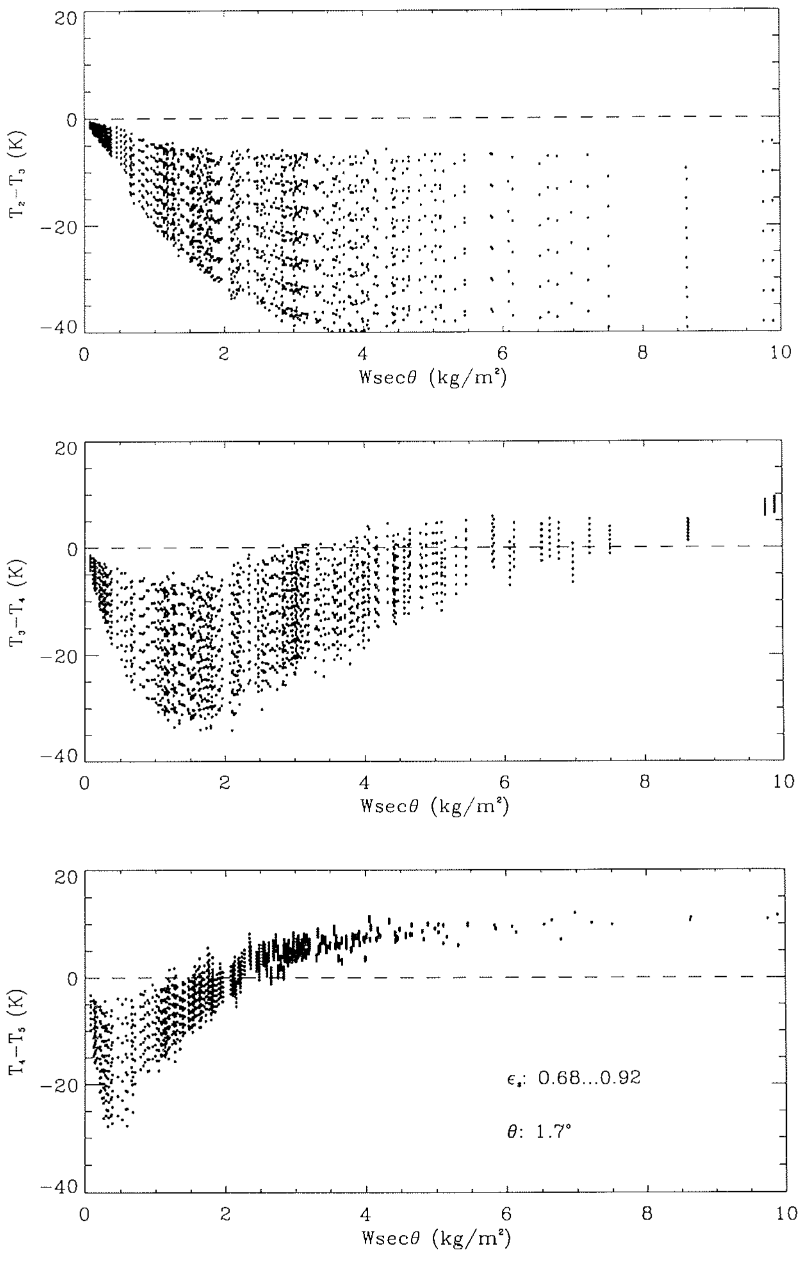

Figure 4.3: *Simulated brightness temperature differences between the neighboring channels of SSM/T2 with local zenith angle of 1.7°, using the radiosonde soundings in the regression group.*

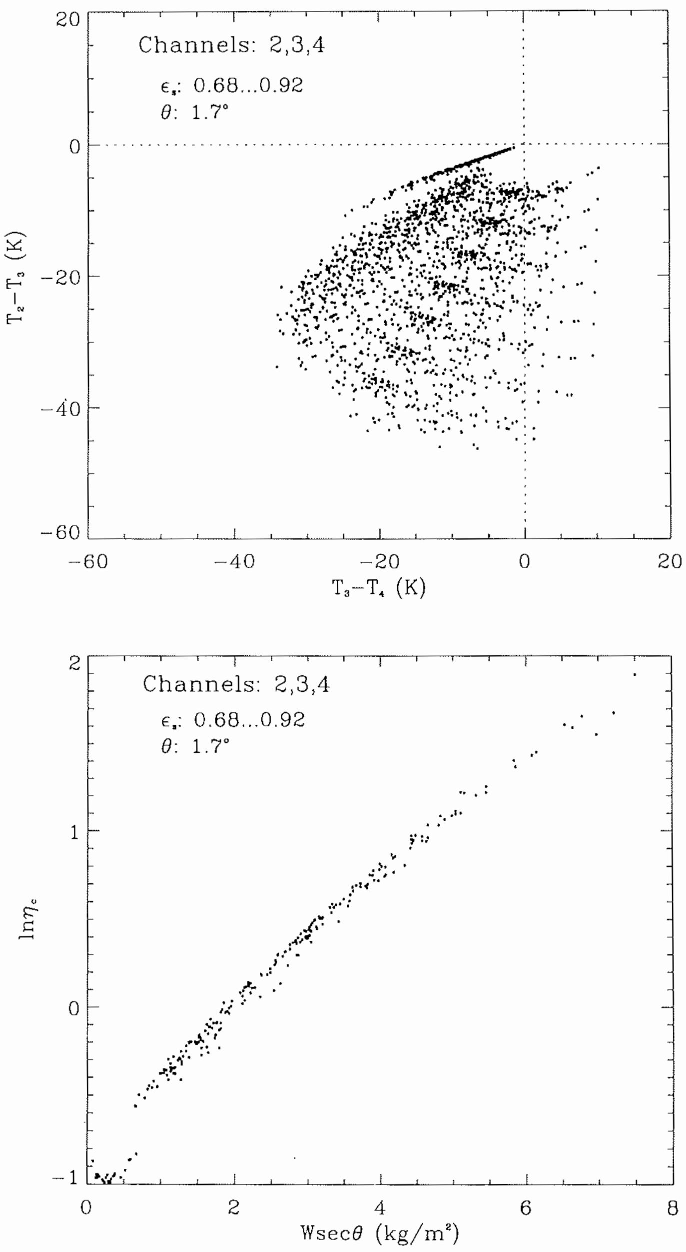

Figure 4.4: *The same results as shown in Figure 4.3 but in the plane of* $T_3 - T_4$ *and* $T_2 - T_3$ *(top) and the relationship between the RCBTD* η_c *and the total water vapor* W *when the biases are exactly compensated (bottom).*

4.2.2 Development of an Algorithm to Retrieve Water Vapor over Antarctica

The algorithm for retrieving the water vapor content of the atmosphere over Antarctica is based on the simple relationship between $\ln \eta_c$ and the total water vapor W, as discussed in Chapter 2 and again shown in the previous section. In general, however, this relationship is not linear. Referring to Figure 4.4, the relationship for the SSM/T2 channels 2, 3, and 4 is very close to a linear one in the range of $W \sec\theta$ from $1.0\,\mathrm{kg/m^2}$ to about $5.0\,\mathrm{kg/m^2}$. Therefore, a linear expression is used to relate $W \sec\theta$ with $\ln \eta_c$,

$$W \sec\theta = C_0 + C_1 \ln \eta_c. \tag{4.3}$$

The coefficients C_0 and C_1 will be determined empirically below.

Since the SSM/T2 channels have different sensitivities to water vapor and a channel can not be used if it is saturated, the algorithm should be accommodated to different ranges of the water vapor burden in the atmosphere. Whether a channel is saturated or not is judged using the saturation point defined in Section 2.2.4. Since the saturation point changes with the surface emissivity, the retrievable range for a given combination of channels will change accordingly. Normally, the combination of channels 3, 4 and 5 is used for atmospheres with total water vapor less than $1.5\,\mathrm{kg/m^2}$, and the combination of channels 2, 3 and 4 is used for atmospheres with total water vapor less than $6.0\,\mathrm{kg/m^2}$. In calculating η_c, the biases b_{ij} and b_{jk} are taken to be constants, *i.e.* $\bar{b}_{ij}$ and $\bar{b}_{jk}$,

$$\eta_c = \frac{T_i - T_j - \bar{b}_{ij}}{T_j - T_k - \bar{b}_{jk}}. \tag{4.4}$$

This not only simplifies the algorithm but also is reasonable. As already discussed in Section 2.3.2, $\bar{b}_{ij}$ and $\bar{b}_{jk}$ are the coordinates of the "focal point" F in the plane $(T_j - T_k)$ and $(T_i - T_j)$ (see Fig. 2.9), and they are determined here by minimizing the square mean distance between F and the lines determined by the brightness temperature differences with different surface emissivities, based on all the radiosonde soundings in the regression group.

In determining the constant biases, $\bar{b}_{ij}$ and $\bar{b}_{jk}$, and the coefficients C_0 and C_1 for the combination of channels 3, 4 and 5, only the simulated brightness temperatures corresponding to soundings with total water vapor less than $1.6\,\mathrm{kg/m^2}$ are used, as shown in Figure 4.5. Of course, the soundings with $T_4 - T_5$ greater than zero are excluded, since channel 5 is saturated in these cases. Following the same way, the biases and coefficients for the combination of channels 2, 3 and 4 are determined, using the brightness temperature differences that correspond to the soundings with total water vapor less than $6.0\,\mathrm{kg/m^2}$ and satisfying the condition $T_4 - T_5 < 0$ (see Fig. 4.6). Generally, the retrieval becomes worse when the total water vapor in the atmosphere becomes larger. For the combination of channels 2, 3 and 4, the retrieval becomes problematic when the atmosphere has very low water vapor burden. The reasons are that, on the one hand, the absorption of oxygen becomes important when the water vapor content in the atmosphere is very low; and on the

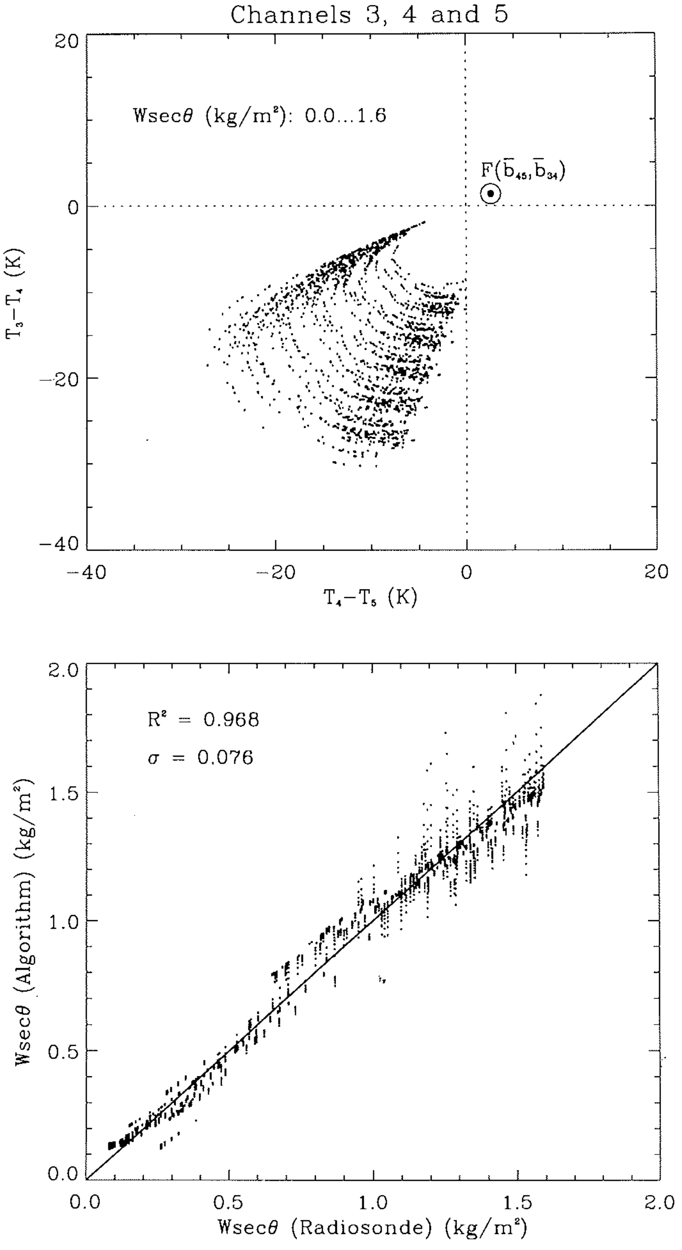

Figure 4.5: *The brightness temperature differences for the combination of channels 3, 4 and 5 over the full range of retrievals: (top) the simulated data used to determine the biases* $\bar{b}_{45}$ *and* $\bar{b}_{34}$*, and the coefficients,* C_0 *and* C_1*; (bottom) the relationship between the total water vapor derived from radiosondes and that obtained from the relation given in Eq. (4.3), for soundings in the regression group.*

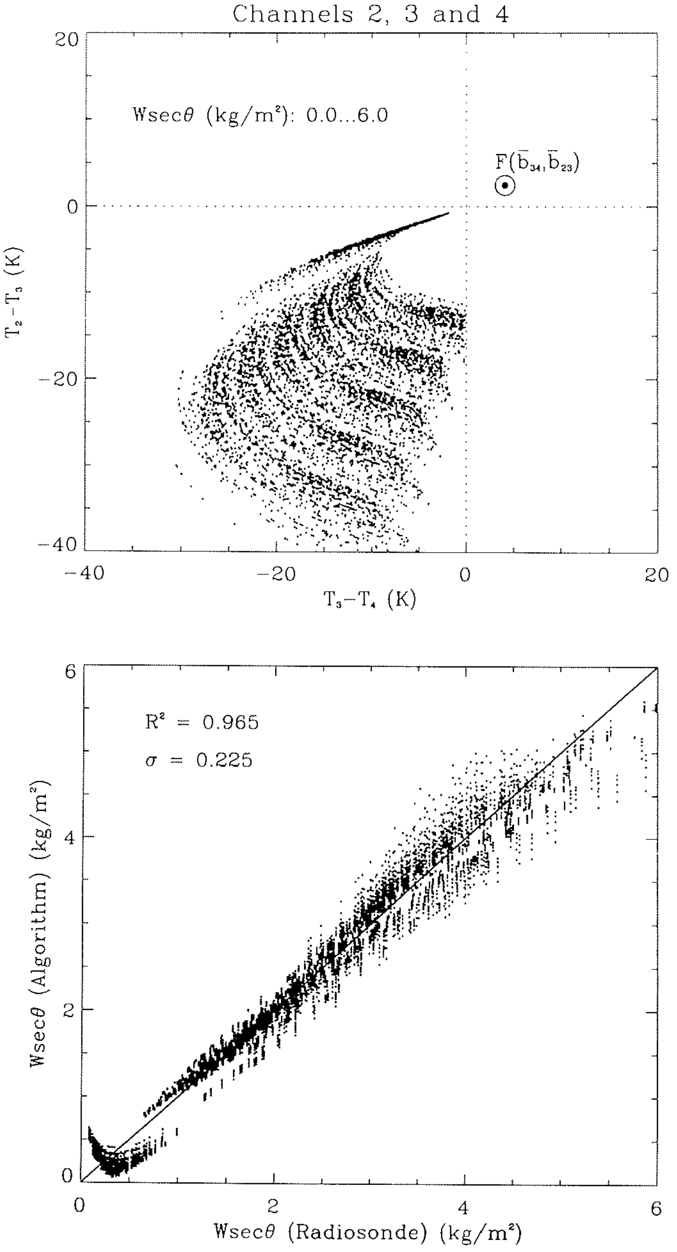

Figure 4.6: *The brightness temperature differences for the combination of channels 2, 3 and 4 over the full range of retrievals: (top) the simulated data used to determine the biases,* $\bar{b}_{34}$ *and* $\bar{b}_{23}$*, and the coefficients,* C_0 *and* C_1*; (bottom) the relationship between the total water vapor derived from radiosondes and that from the relation given in Eq. (4.3), for soundings in the regression group.*

Table 4.1: The Biases and the Coefficients for Channels 3, 4 and 5

$W \sec\theta$ (kg/m^2)	F($\bar{b}_{45}, \bar{b}_{34}$) (K)	C_0	C_1
Full Range: [0.0· · ·1.5]	(2.556, 1.370)	0.689	0.723
Subrange 1: [0.0· · ·0.5]	(1.831, 0.901)	0.685	0.690
Subrange 2: [0.5· · ·1.0]	(1.378, 0.343)	0.671	0.565
Subrange 3: [1.0· · ·1.5]	(3.380, 3.027)	0.693	0.753

Table 4.2: The Biases and the Coefficients for Channels 2, 3 and 4

$W \sec\theta$ (kg/m^2)	F($\bar{b}_{34}, \bar{b}_{23}$) (K)	C_0	C_1
Full Range: [0.0· · ·6.0]	(4.066, 2.458)	2.041	2.275
Subrange 1: [1.0· · ·2.0]	(2.737, 1.980)	1.907	2.030
Subrange 2: [2.0· · ·4.0]	(5.591, 4.754)	2.010	2.316
Subrange 3: [4.0· · ·6.0]	(3.525, 0.384)	2.414	2.110

other hand, the soundings with very low water vapor content are mostly from the South Pole, where the water vapor is at a much lower temperature than in the coastal region. However, this is not a serious problem for SSM/T2, because another combination of channels can be used in cases of very low water vapor burden.

To take advantage of the highest sensitivity to water vapor provided by channel 5, channels 3, 4 and 5 are used in cases of total water vapor less than 1.5 kg/m^2; and channels 2, 3 and 4 are used for cases with $W \sec\theta$ larger than 1.5 kg/m^2. To further improve the retrieval, the full ranges of $W \sec\theta$ corresponding to each combination of channels can be divided into a few subranges, in which the biases, $\bar{b}_{ij}$ and $\bar{b}_{jk}$, and the coefficients, C_0 and C_1, are determined separately. For each combination of channels, three subranges are defined. Figures 4.7, 4.8 and 4.9 show the simulated data used to determine the biases and coefficients in the three subranges of total water vapor for the combination of channels 3, 4 and 5, and Figures 4.10, 4.11 and 4.12 show the situation for channels 2, 3 and 4. The biases and coefficients corresponding to both the full range and the subranges are given in Table 4.1 for channels 3, 4 and 5 and in Table 4.2 for channels 2, 3 and 4.

In summary, the RCBTD scheme for the total water vapor retrieval using the measurements of SSM/T2 is done in the steps as shown in Figure 4.13. (1) Calculate $\sec\theta$ and the brightness temperature differences between neighboring channels. (2) Calculate the atmospheric total water vapor $W \sec\theta$ as seen by the sensor at the local zenith angle θ using Eq. (4.3). Which combination of channels is used in the calculation is determined by examining the saturation points. If the most sensitive channel 5, is not saturated, channels 3, 4 and 5 are used. Otherwise, channels 2, 3 and 4 are used. If $T_3 - T_4 > 0$, channel 4 is saturated and the situation is classified as a pixel where water vapor cannot be retrieved using SSM/T2. In calculating $W \sec\theta$, the biases and coefficients corresponding to the full range are used at first,

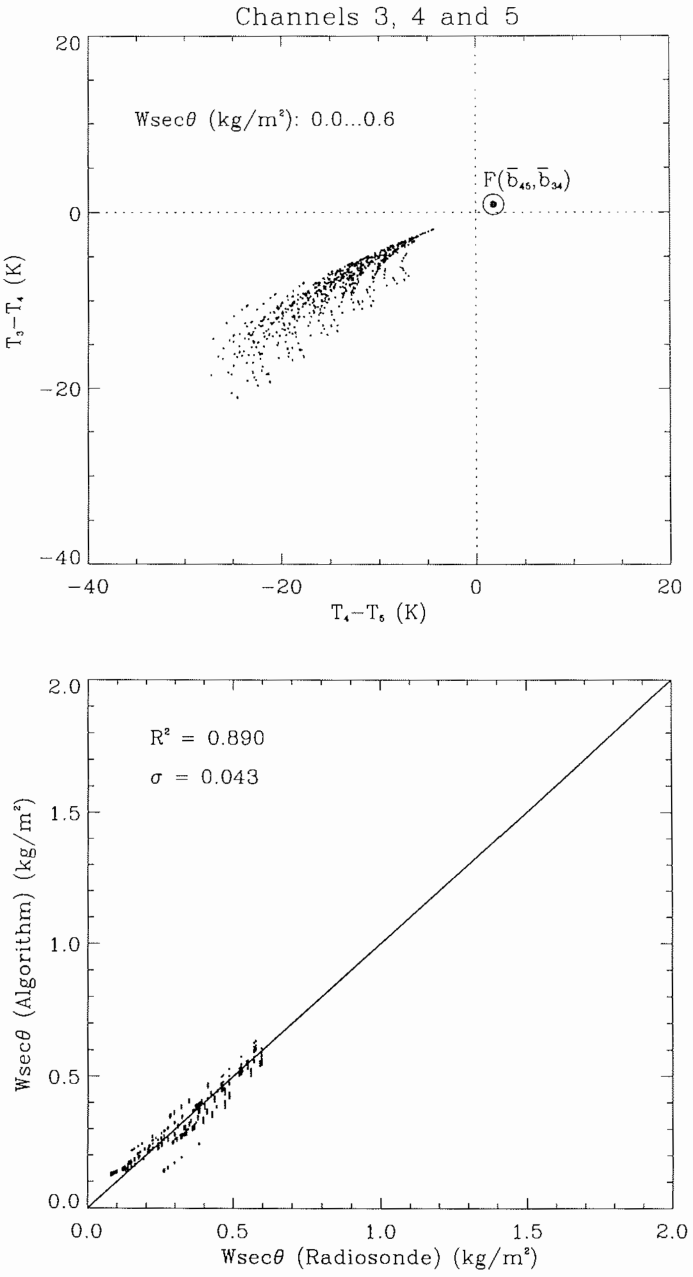

Figure 4.7: *Subrange 1 for the combination of channels 3, 4 and 5: (top) the simulated data used to determine the biases* $\bar{b}_{45}$ *and* $\bar{b}_{34}$*, and the coefficients,* C_0 *and* C_1*; (bottom) the relationship between the total water vapor derived from radiosondes and that obtained from the relation given in Eq. (4.3), for soundings in the regression group.*

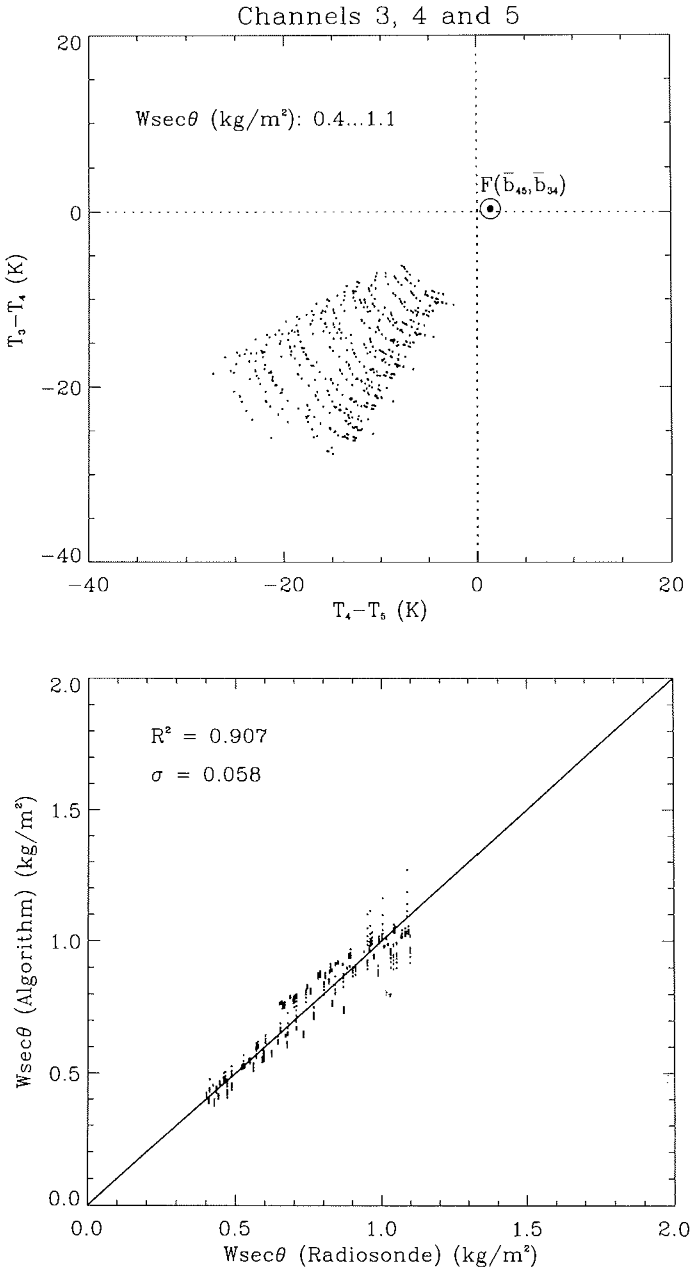

Figure 4.8: *Subrange 2 for the combination of channels 3, 4 and 5: (top) the simulated data used to determine the biases* $\bar{b}_{45}$ *and* $\bar{b}_{34}$*, and the coefficients,* C_0 *and* C_1*; (bottom) the relationship between the total water vapor derived from radiosondes and that obtained from the relation given in Eq. (4.3), for soundings in the regression group.*

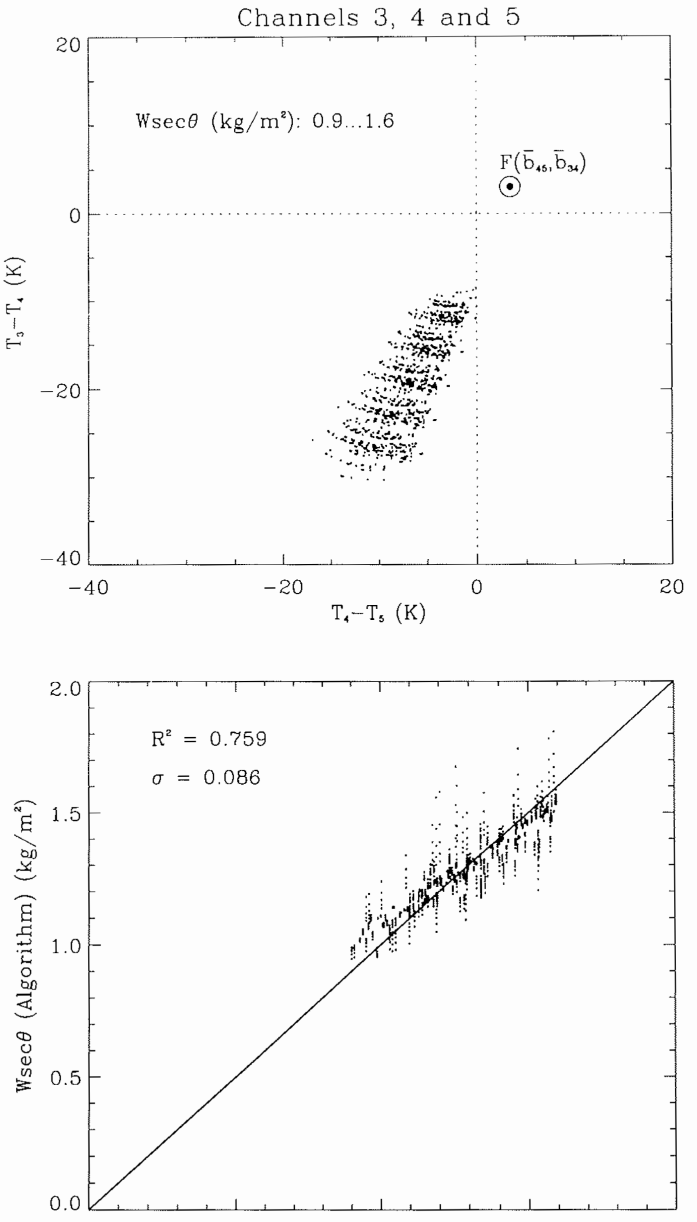

Figure 4.9: *Subrange 3 for the combination of channels 3, 4 and 5: (top) the simulated data used to determine the biases* $\bar{b}_{45}$ *and* $\bar{b}_{34}$*, and the coefficients,* C_0 *and* C_1*; (bottom) the relationship between the total water vapor derived from radiosondes and that obtained from the relation given in Eq. (4.3), for soundings in the regression group.*

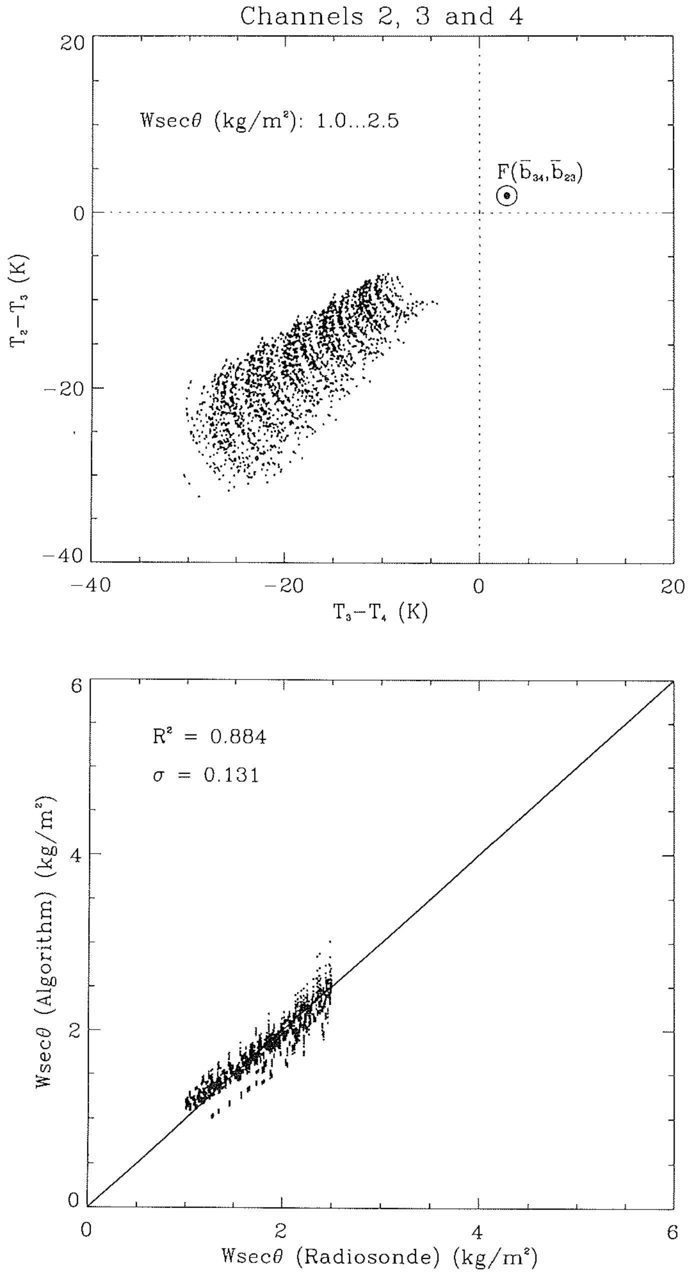

Figure 4.10: *Subrange 1 for the combination of channels 2, 3 and 4: (top) the simulated data used to determine the biases* $\bar{b}_{34}$ *and* $\bar{b}_{23}$*, and the coefficients,* C_0 *and* C_1*; (bottom) the relationship between the total water vapor derived from radiosondes and that obtained from the relation given in Eq. (4.3), for soundings in the regression group.*

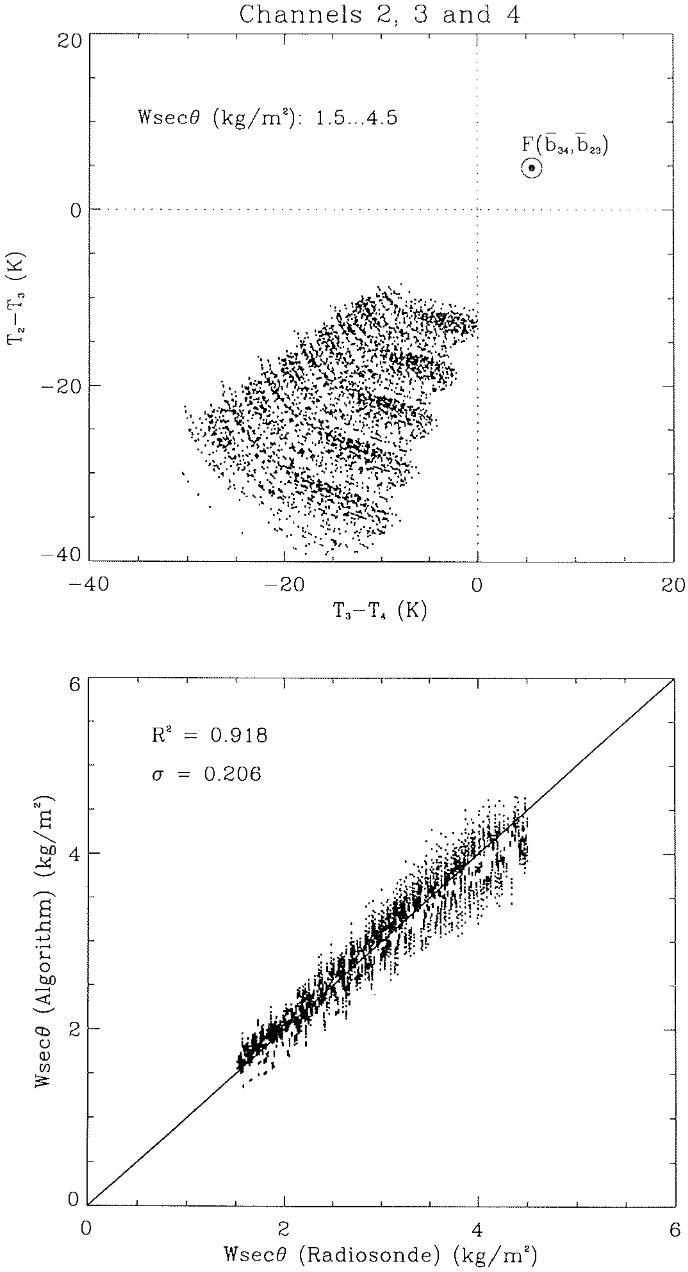

Figure 4.11: *Subrange 2 for the combination of channels 2, 3 and 4: (top) the simulated data used to determine the biases* $\bar{b}_{34}$ *and* $\bar{b}_{23}$*, and the coefficients,* C_0 *and* C_1*; (bottom) the relationship between the total water vapor derived from radiosondes and that obtained from the relation given in Eq. (4.3), for soundings in the regression group.*

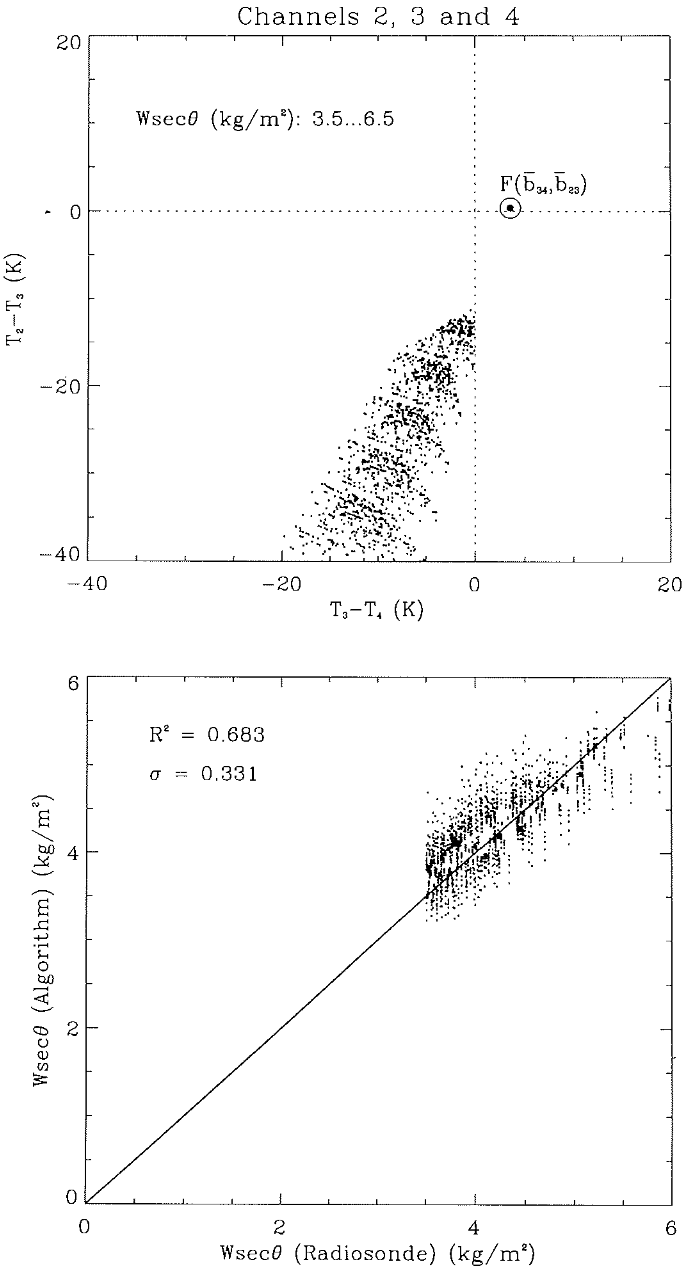

Figure 4.12: *Subrange 3 for the combination of channels 2, 3 and 4: (top) the simulated data used to determine the biases* $\bar{b}_{34}$ *and* $\bar{b}_{23}$*, and the coefficients,* C_0 *and* C_1*; (bottom) the relationship between the total water vapor derived from radiosondes and that obtained from the relation given in Eq. (4.3), for soundings in the regression group.*

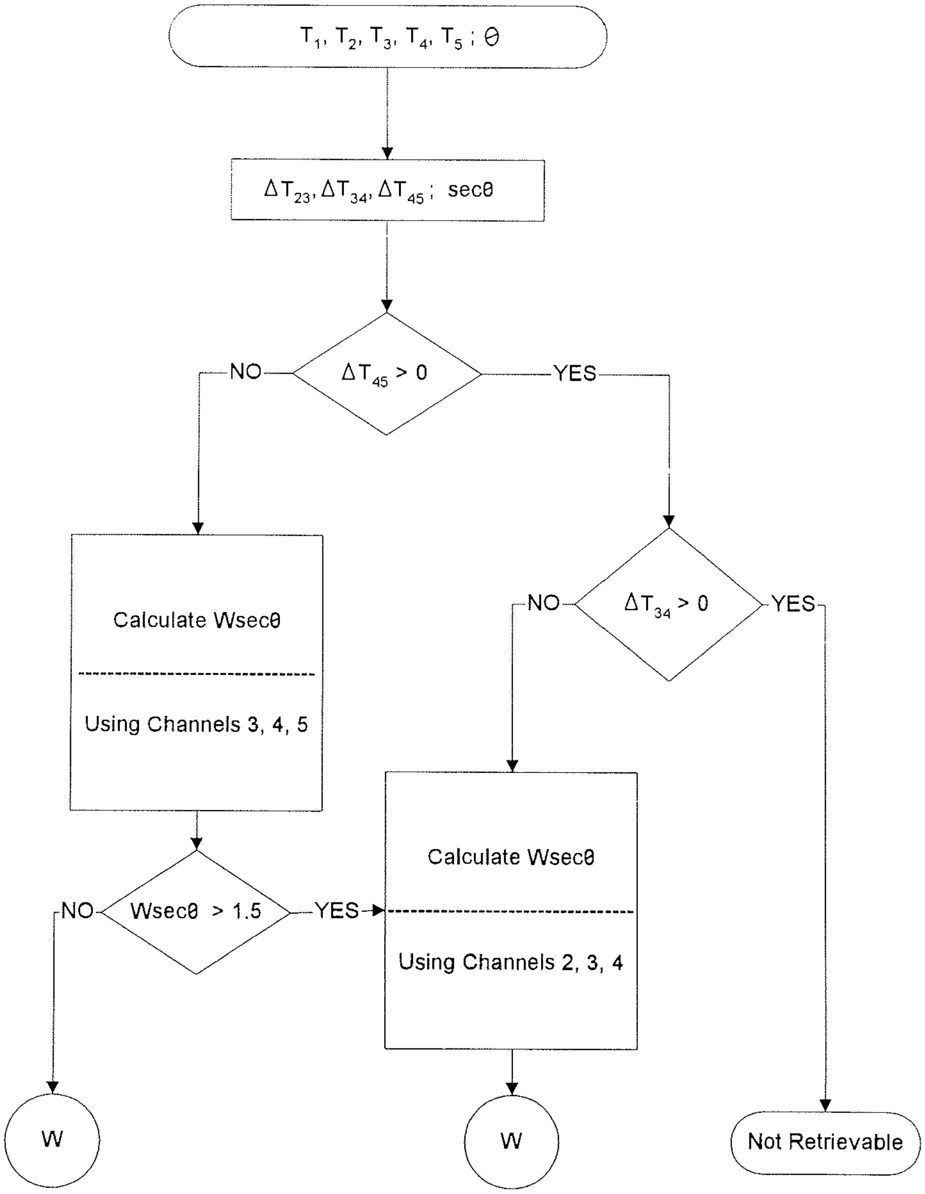

Figure 4.13: *The flow diagram of the RCBTD algorithm for total water vapor retrieval.*

then the retrieval is improved by re-doing it using the biases and the coefficients corresponding to the subrange at which $W \sec\theta$ lies. (3) Calculate W using the results of $W \sec\theta$ and $\sec\theta$.

4.3 Error Analysis and Validation

4.3.1 Error Analysis of the Algorithm

The aim of the error analysis is to provide a quantitative estimation for the retrieval errors caused by clouds and uncertainties in the modeling of gaseous absorption and in radiometric measurements . The effects of clouds will be discussed in the next section. The uncertainties of Liebe's model, which is used in MWMOD to calculate the oxygen and water vapor absorption, are taken to be insignificant. Hence, just the effects of the uncertainties in radiometric measurements are considered in the following.

Due to the limited bandwidth, limited integration time and imperfect calibration, the measurements of SSM/T2 contain uncertainties. Since the same cold and warm loads are used to calibrate all SSM/T2 channels, the uncertainties of these channels are to some extent correlated. However, just the brightness temperature differences are needed in the algorithm, therefore, the uncertainty due to an imperfect calibration is strongly reduced. Referring to the NET of SSM/T2 channels in Table 1.1, the uncertainty of the brightness temperature differences between two neighboring channels is conservatively assumed to be Gaussian noise with a standard deviation of 1.0 K; and the uncertainties of $T_i - T_j$ and $T_j - T_k$ are taken to be uncorrelated. Under these conditions, the root-mean-square error of the algorithm, *i.e.* the sensitivity of the algorithm to radiometric errors is calculated and shown in Figure 4.14. Clearly, the smaller the brightness temperature differences between neighboring channels, the larger the retrieval error. The brightness temperature difference becomes small in the following three cases: (1) the water vapor content in the atmosphere approaches zero, (2) the atmosphere is so humid that one of the used channels approaches saturation, and (3) the surface emissivity is large. Consequently, it is reasonable to use different combinations of channels for different ranges of total water vapor, by taking advantage of the different sensitivities of SSM/T2 channels to water vapor.

4.3.2 Validation of the Algorithm

To validate the algorithm, the radiosonde soundings in the test group are used to simulate the measurements of SSM/T2. In retrieving the total water vapor, the steps shown in Figure 4.13 are exactly followed. For clarity, only the results with local zenith angle of 1.7° and 47.26°, which are the minimum and maximum of the local zenith angle respectively, are given here. Figure 4.15 compares the values of $W \sec\theta$ retrieved by the algorithm and obtained from radiosondes, when the surface emissivity changes from 0.68 to 0.92. As the total water vapor in the atmosphere

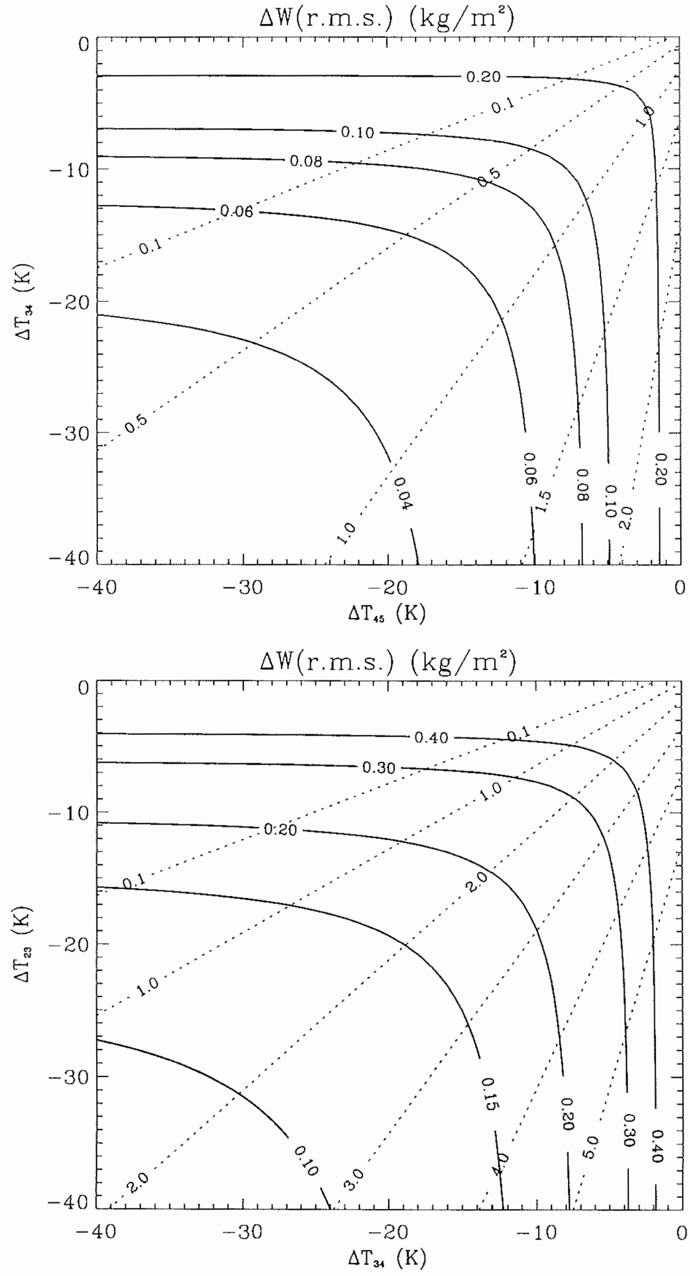

Figure 4.14: *The retrieval errors (r.m.s.) (solid lines) of the algorithm for 1.0 K (r.m.s.) uncertainty in the brightness temperature differences, in cases of using channels 3, 4 and 5 (top) and using channels 2, 3 and 4 (bottom). The dashed lines represent contours of the total water vapor.*

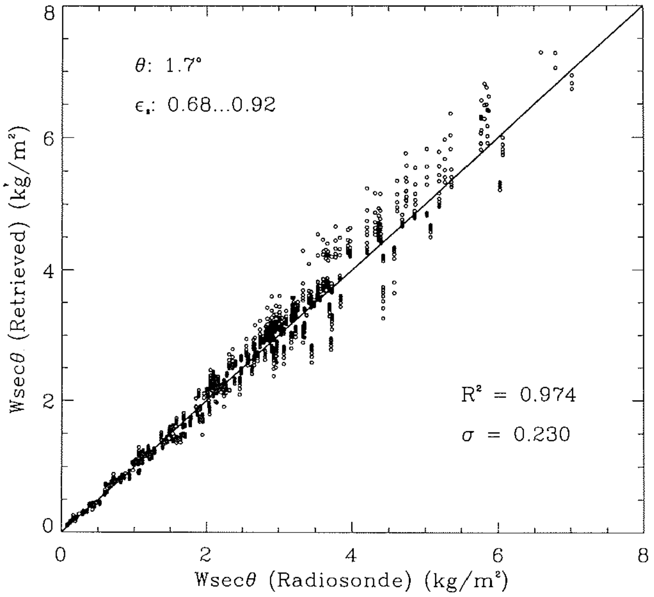

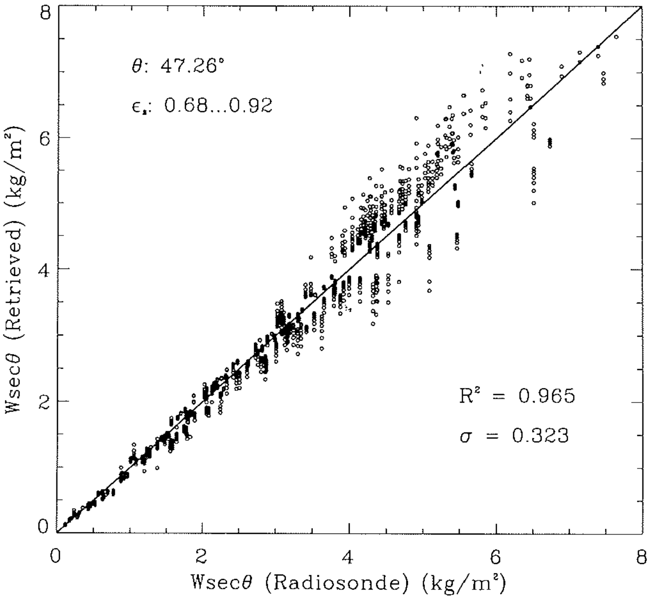

Figure 4.15: *Comparison of the total water vapor from radiosonde soundings and retrieved using simulated brightness temperatures of SSM/T2, with the surface emissivity in the range of 0.68· · ·0.92. The top plot shows the results with local zenith angle of 1.7° and the bottom plot shows the results at 47.26°.*

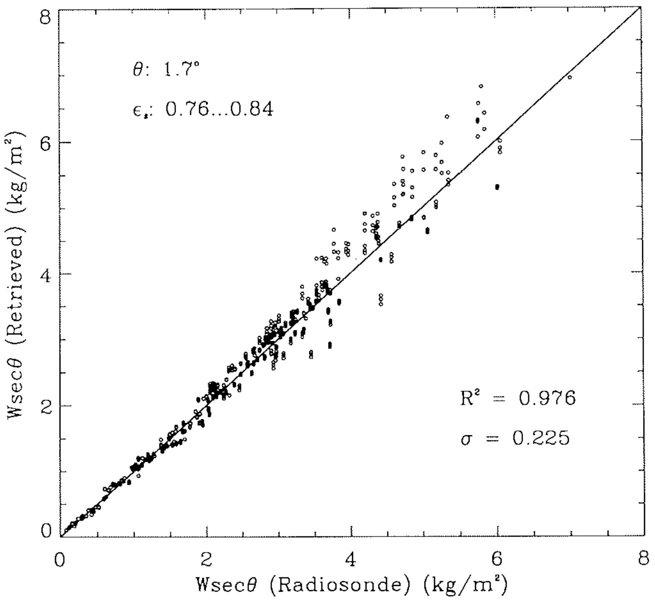

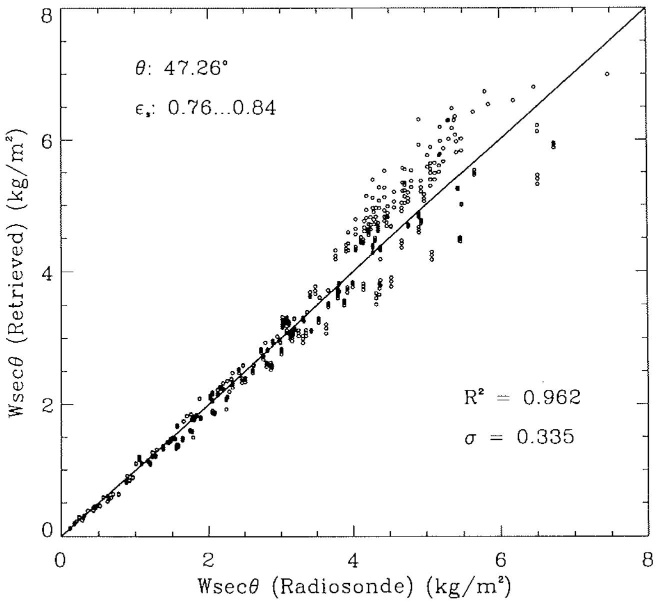

Figure 4.16: *Comparison of the total water vapor from radiosonde soundings and retrieved using simulated brightness temperatures of SSM/T2, with the surface emissivity in the range of 0.76· · ·0.84. The top plot shows the results with local zenith angle of 1.7° and the bottom plot shows the results at 47.26°.*

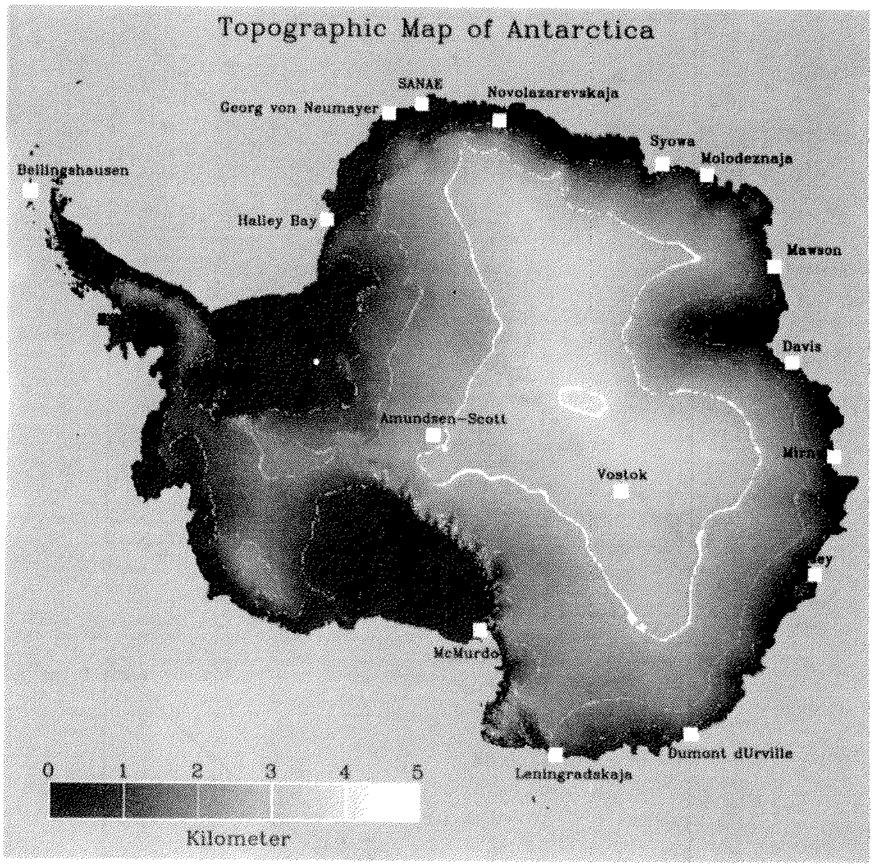

Figure 4.17: *The locations of the Antarctic stations, where the seasonal mean of total water vapor is compared with that retrieved from SSM/T2 data.*

increases, the retrieval error increases, as expected by the theoretical analysis in Chapter 2. If the retrievals are restricted to a smaller range of surface emissivities, from 0.76 to 0.88, as shown in Figure 4.16, no significant improvements are observed, indicating that the vertical structure of the atmosphere is the dominant factor to cause errors in the retrieval.

To further validate the algorithm, the seasonal means of the total water vapor measured by radiosondes at Antarctic stations are compared with the retrievals using SSM/T2 data. The spatial distribution of the 16 stations is shown in Figure 4.17. Most of these stations are located along the Antarctic coast. The seasonal means at these stations are obtained from radiosonde data in the time periods from 1988 to 1990 and from 1980 to 1982 (*Connolley and King*, 1993). Due to the limited amount of available satellite data, only the results in the austral winter (June, July and August) are analyzed: and the results of total water vapor derived from SSM/T2 data are collected in June and July of 1995. In the comparison, SSM/T2

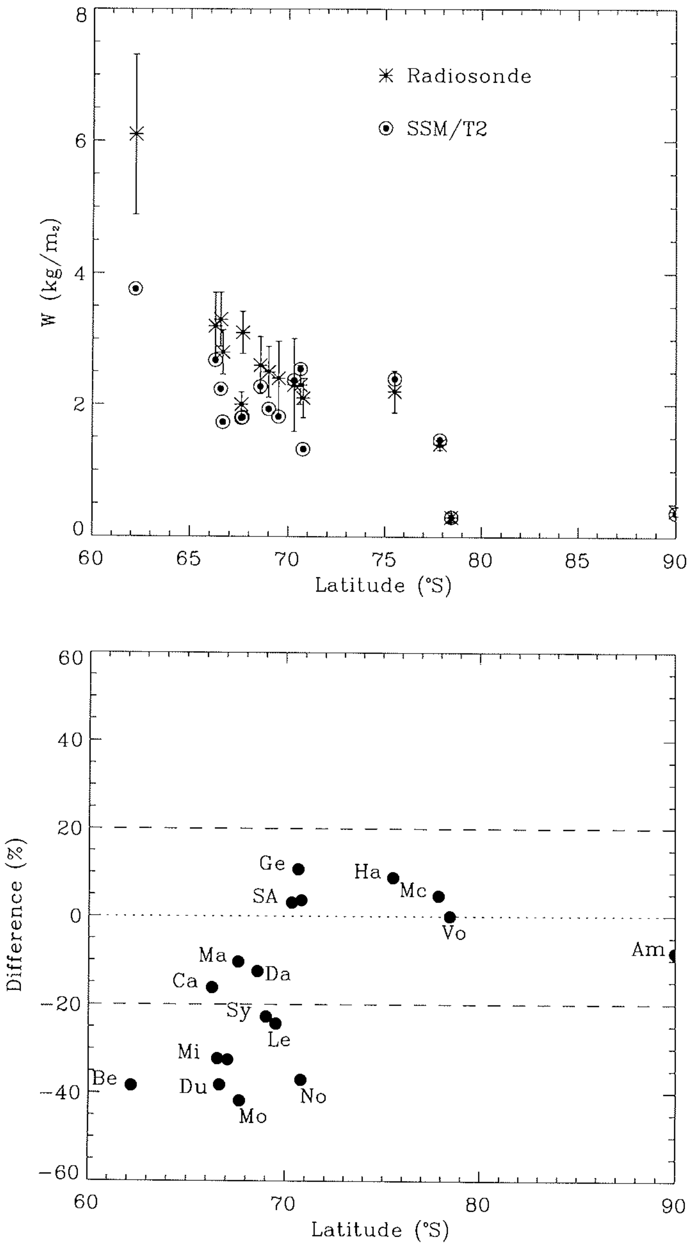

Figure 4.18: *Comparison of the seasonal mean (in Antarctic winter, June, July and August) of the total water vapor from radiosonde and from SSM/T2 at 16 Antarctic stations. In the bottom plot, the two letters near each point are the first two letters of the station name.*

results are averages in an area of $200 \times 200\,\text{km}^2$ around the stations. As shown in Figure 4.18, the general trend of atmospheric water vapor with the latitude is reproduced by the SSM/T2 measurements. The general underestimation of the SSM/T2 results with decreasing latitude is related to the fact that the retrieval using SSM/T2 data is only done for cases of total water vapor less than $6.0\,\text{kg/m}^2$ and the cases with $W \sec\theta$ larger than this value or with water clouds are classified as not retrievable, and therefore the retrieval results at these pixels are taken as missing data. Referring to the bottom plot in Figure 4.18, the relative differences between radiosonde results and SSM/T2 measurements are less than 20% at 9 out of the 16 stations. At 5 of the 7 remaining stations, which are operated by Russia, a so called "goldbeater's skin" humidity sensor is used, which is known to measure water vapor values approximately 10% too high at low humidities (*Connolley and King*, 1993). This and the fact that humidity sensors at low temperatures are not very reliable might explain at least part of the differences.

4.4 Effects of Clouds on the Retrieval

4.4.1 Clouds over Antarctica

Clouds are disturbing the retrieval of water vapor content in the atmosphere. Before analyzing their effects on the RCBTD algorithm, some basic features of Antarctic clouds are summarized here.

The cloud distribution at high southern latitudes has been investigated during the International Satellite Cloud Climatology Project (ISCCP) (*King and Turner*, 1997). Results (see Figure 4.19) indicate that the zone of greatest cloud covers occurs over the ocean area near the ice edge, where synoptic-scale weather systems are most active. North and south of this band the amount of cloud decreases, relatively little cloud cover is found over the interior of the continent. The distribution of cloud types in Antarctica is also dependent on the latitude. At latitudes higher than 70°S over the continental plateau, cirrus is the most common type of clouds. Along the Antarctic coast at about 70°S, cirrus and altostratus are found in about equal amounts. The most striking feature of cloud type distribution is the large amount of stratus close to 60°S, which is associated with the large number of depressions at this latitude and is a feature of all seasons. Compared with the large amount of satellite images and human observations on cloud amount and cloud types, there are very little *in situ* measurements of microphysical parameters of clouds in Antarctica. Only some measurements using radiometersondes at the south pole (*Stone*, 1993) and using lidar at the French Dumont d'Urville station (*Del Guasta et al.*, 1993) provided valuable information on the cloud extent and on the physical phase of water and the ice crystal habit in the Antarctic clouds at the continental interior and at the coastal region. Because of the low temperature the clouds over the continent are composed of small ice particle, with ice contents from about $0.0003\,\text{g/m}^3$ to $0.006\,\text{g/m}^3$, and contain little or no liquid water. They are moderately thick, on average, extending to heights greater than 3 km above the top of the surface-based inversion layer. Overall, the clouds observed at the South Pole

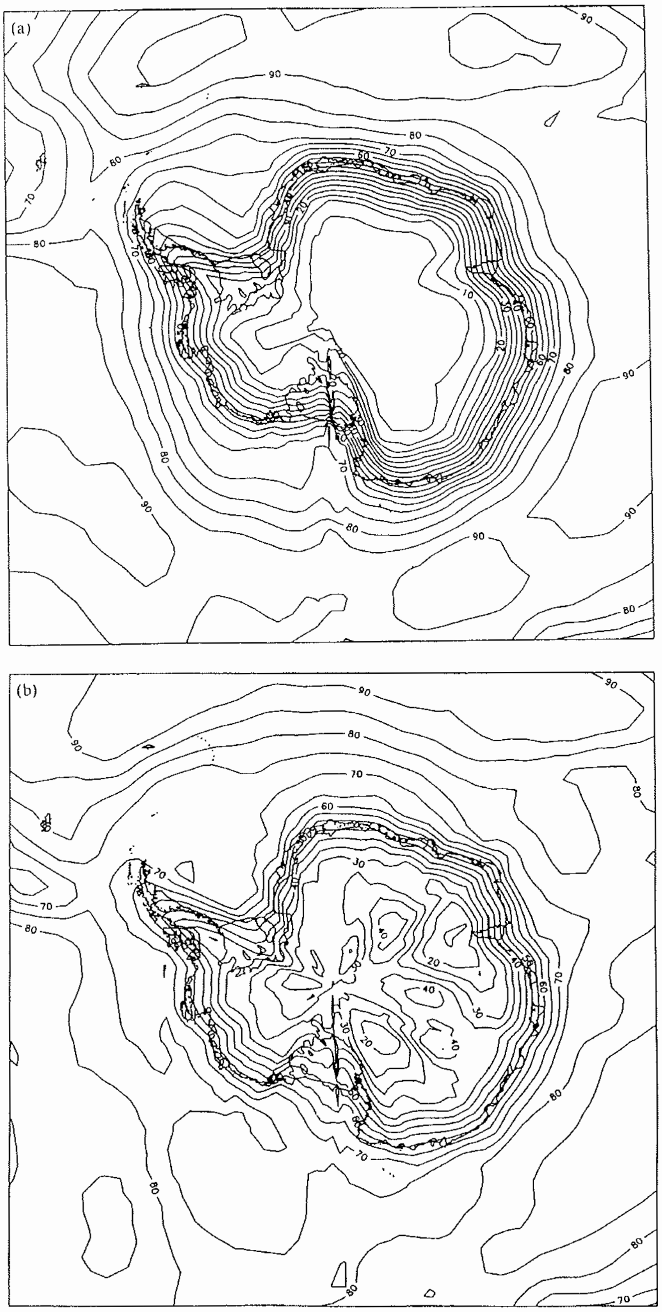

Figure 4.19: *Mean cloud amount (percent) from the International Satellite Cloud Climatology Project (ISCCP): (a) Summer; (b) Winter. (From King and Turner [1997])*

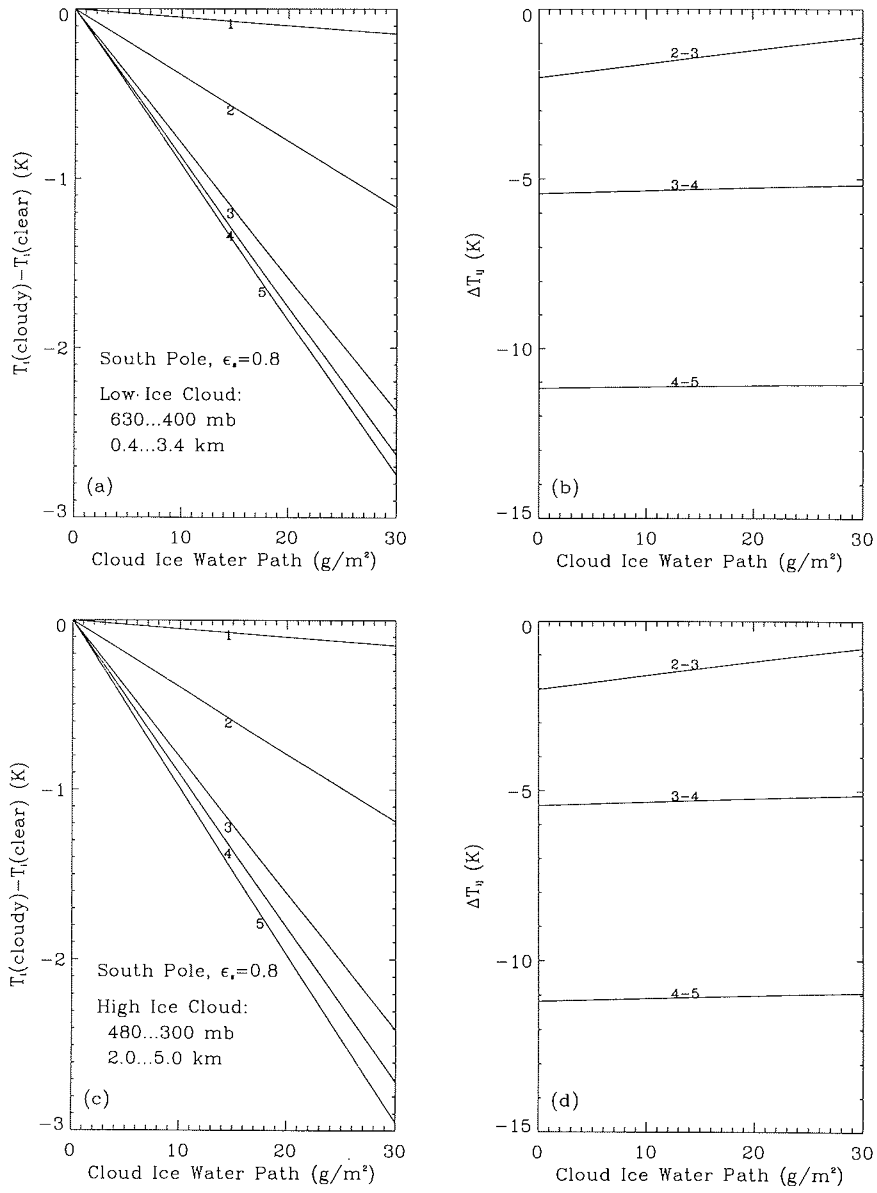

Figure 4.20: *The influence of ice clouds over the Antarctic plateau on the brightness temperature T_i and on the brightness temperature difference ΔT_{ij} for low clouds ((a) and (b)) and high clouds ((c) and (d)).*

are similar to the high altitude cirrus found at mid-latitude. In the coastal region clouds are relatively warm and contain a significant amount of liquid water droplets. The statistics based on lidar data showed that the high clouds at the coast are thicker than those found at mid-latitudes (~3,000 m). The uniformity of depolarization of the lidar return signal suggested that there are no dramatical changes in the ice crystal shape and the size distribution in the deep clouds that had temperatures below −40°C.

4.4.2 Effects of Ice and Water Clouds

The effects of clouds on the total water vapor retrieval using the RCBTD method are examined through model simulations based on the unfortunately limited knowledge on Antarctic clouds. The drop-size distribution of cirrostratus clouds at mid-latitudes given by *Ulaby et al.* [1981] is used in the simulation of Antarctic ice clouds. Compared with the inferred effective radii of Antarctic ice clouds, which are varied between about 4 μm and 16 μm, the model of *Ulaby et al.*, which is a modified Gamma distribution with a mode radius of 40 μm, overestimates the sizes of ice crystals in Antarctic ice clouds. The simulated effects of ice clouds on the brightness temperatures and the brightness temperature differences are shown in Figure 4.20. Two types of clouds are examined, representing the typical situations of low and high ice clouds. The scattering of ice crystals generally decreases the measured brightness temperatures at SSM/T2 channels, by more than 2 K at the 183.31 GHz channels when the ice water path of the cloud reaches 30 g/m^2. However, the effect of ice clouds on the brightness temperature differences between neighboring channels is not large, especially at the three channels near 183.31 GHz. The changes of ΔT_{34} and ΔT_{45} are less than 0.5 K for ice water path lower than 30 g/m^2. Such a change is even smaller than the uncertainties in the SSM/T2 measurements. As shown earlier, the total water vapor over the Antarctic plateau is expected to be less than 1.5 kg/m^2 throughout the year, allowing to use the three channels near 183.31 GHz for the retrievals in this region. Therefore, the effect of ice clouds on the retrieval over the Antarctic plateau can be neglected. But, the effects of ice clouds in the coastal region can be significant, because the ice water path of clouds is expected to be larger. Furthermore, in coastal regions, channels 2, 3 and 4 have to be used in the retrieval due to larger water vapor amounts in the atmosphere; and since ΔT_{23} is more strongly influenced by ice clouds than ΔT_{34} and ΔT_{45}, as shown in Figure 4.20(b) and (d), the total water vapor will be significantly underestimated in coastal regions when strong ice clouds appear. Figure 4.21 shows an example. The underestimation of the total water vapor due to ice clouds is large, changing from 0.20 kg/m^2 to 0.75 kg/m^2 as the surface emissivity increases from 0.65 to 0.90, for an atmosphere with a total water vapor of only 1.73 kg/m^2.

The influence of water clouds on the RCBTD scheme will be investigated in the next step. Normally, the measured brightness temperature increases distinctly with the increase of liquid water amount in the cloud due to increased emissions of the atmosphere if the effect of scattering is negligible, except at saturated channels. Consequently, the absolute value of brightness temperature differences between neighboring channels decreases significantly with the increase of cloud liquid wa-

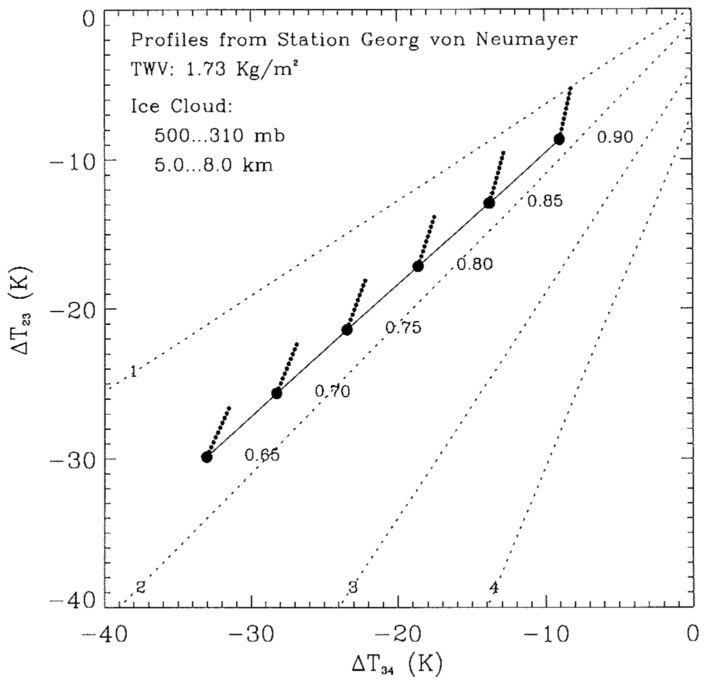

Figure 4.21: *The effects of ice cloud on the retrieval of total water vapor near the Antarctic coast. The large, full circles represent the values for clear sky at different surface emissivities. The small, full circles indicate the changes when the cloud ice amount increases from zero to 60 g/m^2. The dashed lines represent contours of constant total water vapor.*

ter (see Fig. 4.22). However, the change of brightness temperature differences due to water cloud has negligible effects on the total water vapor retrieval using the RCBTD method, because the variations of ΔT_{34} and ΔT_{23} with increasing cloud liquid water is along the line of constant total water vapor, as shown in Figure 4.23. Obviously, the effect of water clouds to the RCBTD scheme is very similar to that of a changing surface emissivity. This is a unique feature of the RCBTD method. The key element in this method is the quantity RCBTD η_c, as defined in Eq. (2.43),

$$\eta_c = \frac{\Delta T_{ij} - b_{ij}}{\Delta T_{jk} - b_{jk}}.$$

By substituting the relation between ΔT_{ij} and $\Delta T_{0,ij}$ in Eq (2.32) and the expression of $\Delta T_{0,ij}$ in Eq. (2.23) into the above equation, η_c takes the form of

$$\eta_c = \frac{e^{-2\tau_{0,j}\sec\theta} - e^{-2\tau_{0,i}\sec\theta}}{e^{-2\tau_{0,k}\sec\theta} - e^{-2\tau_{0,j}\sec\theta}}. \tag{4.5}$$

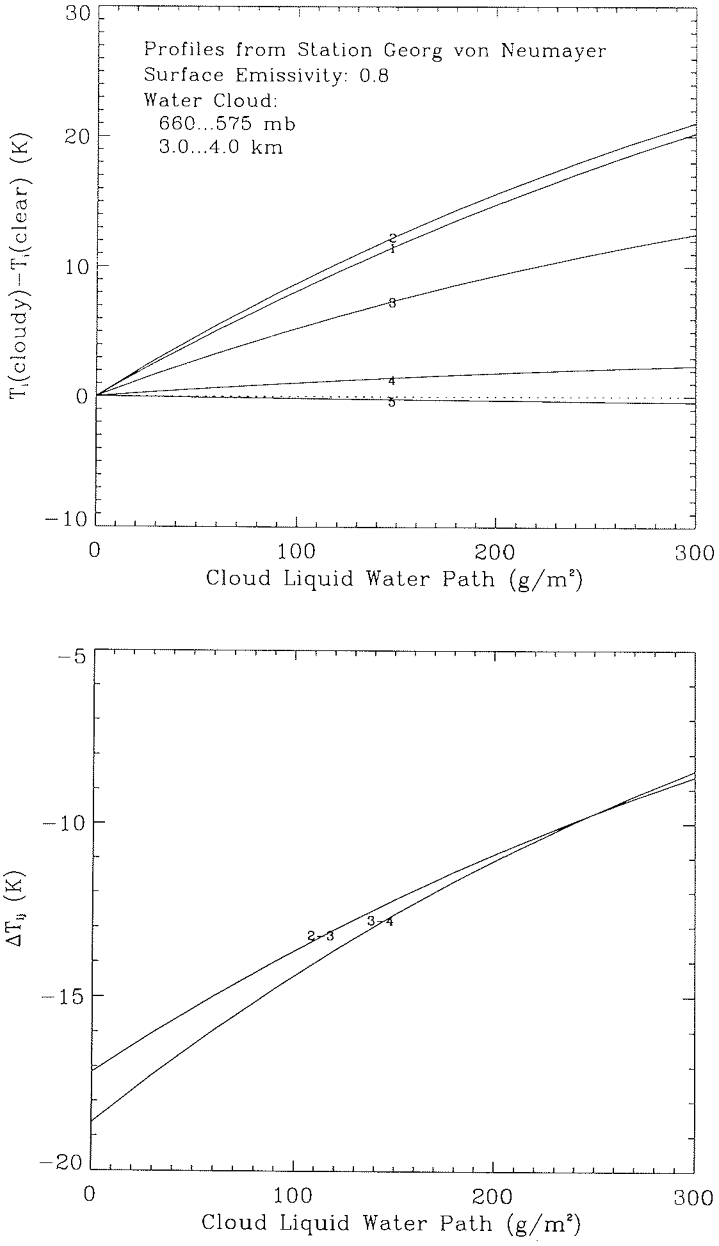

Figure 4.22: *The effects of water clouds on the brightness temperature* T_i *(top) and on the brightness temperature difference* ΔT_{ij} *(bottom).*

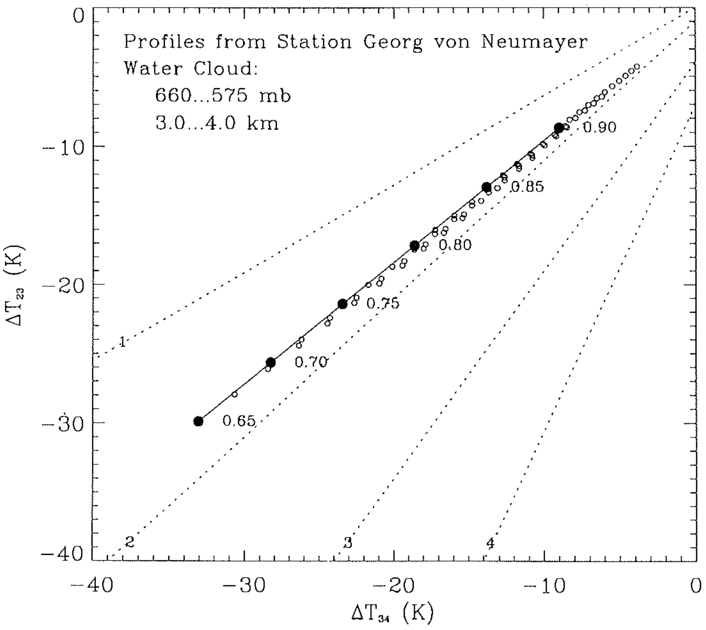

Figure 4.23: *The effect of water cloud in the plane of* ΔT_{34} *and* ΔT_{23}*, corresponding to the simulated results in Figure 4.22. The full circles represent the clear sky conditions and the small open circles represent the situations of water clouds.*

The quantities $\tau_{0,i}$, $\tau_{0,j}$ and $\tau_{0,k}$ are the total opacities of the atmosphere in the direction of nadir at channels i, j and k, respectively. They represent the total absorption of all the atmospheric constituents, in gaseous form and hydrometeors. Since the center frequencies of these channels are very close to each other, the absorptions due to liquid water droplets at the three channels are nearly equal. As a results, the liquid water absorption term can be reduced from the fraction expression of η_c. Of course, this analysis is only valid when the most sensitive one in the three channels is not saturated due to the liquid water absorption.

In fact, the absorption and the scattering of liquid water droplets change with frequencies, which will have some effects on the retrievals. Figure 4.24 shows the simulated results using typical profiles of the atmosphere in the Weddell Sea. In this simulation, water clouds with different base heights and thicknesses are considered. The cloud liquid water content of the clouds changes from 0 to $0.3\,\mathrm{g/m^3}$, with the maximum liquid water path to be $0.6\,\mathrm{kg/m^2}$ for the cloud extending from 1 to 3 km. Clearly, the existence of water clouds causes the RCBTD scheme to slightly overestimate the total water vapor in the atmosphere; and this error increases with the cloud liquid water path but decreases with surface emissivity. In all cases, the errors induced by water clouds are less than 10% when the cloud liquid water path is lower than $0.3\,\mathrm{kg/m^2}$. In conclusion, the effects of water clouds on the retrieval

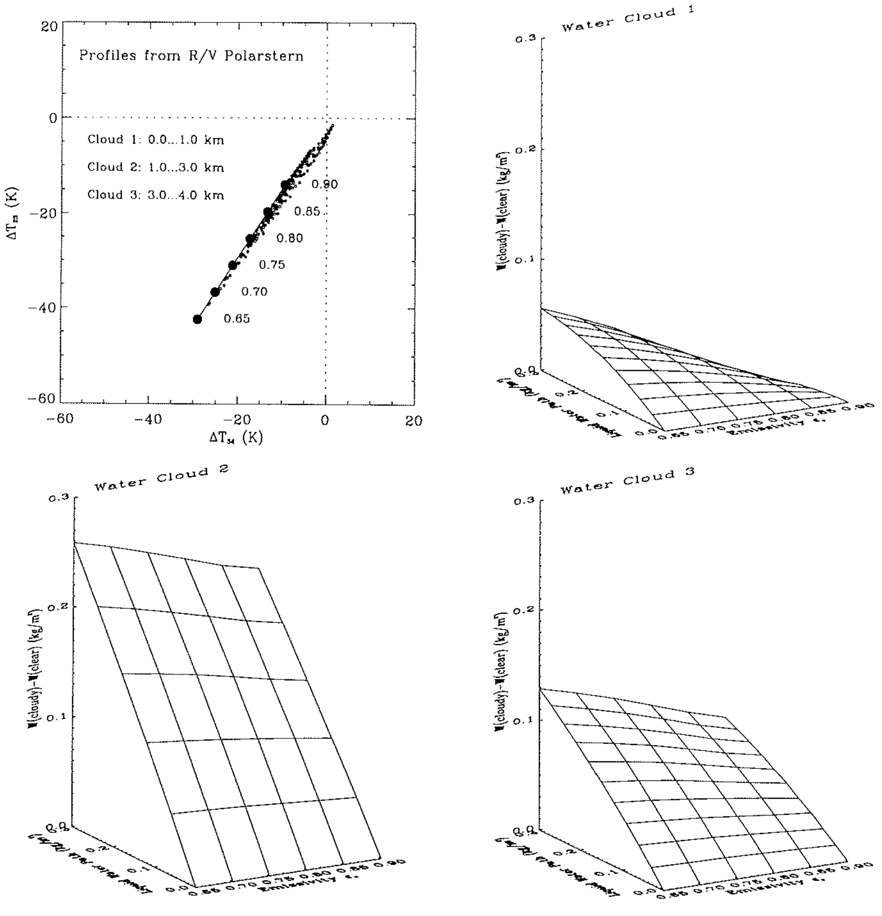

Figure 4.24: *The effects of water clouds at different levels. Cloud 1, 2 and 3 represent the typical situations of low, medium and high clouds, respectively. The total water vapor corresponding to the used profiles is 2.68 kg/m²*.

of atmospheric water vapor using the RCBTD scheme are expected to be small, as long as the liquid water content in clouds are not producing saturation in one of the three channels.

Chapter 5

Application and Future Development

As an application of the proposed RCBTD method, the characteristics of the water vapor distribution in Antarctica are analyzed based on the total water vapor derived from SSM/T2 data. The future developments to improve the retrieval accuracy and to expand the retrievable range of water vapor are discussed in the last section of this chapter.

5.1 Atmospheric Water Vapor in Antarctica

The RCBTD method is very suitable for retrieving the total water vapor amount of the atmosphere over ice covered polar regions, using the measurements performed by the water vapor sounder, SSM/T2, at frequencies near 183.31 GHz. The independence of the ratio of compensated brightness temperature differences, η_c, on the surface emissivity ϵ_s minimizes the influence of the surface emission when retrieving the total water vapor in the atmosphere. It has also been shown that clouds do not pose a serious problem for the retrieval scheme. These unique features of RCBTD method enables us to obtain information on total water vapor over Antarctica on a daily scale, since the polar-orbiting satellites of the DMSP series pass over polar regions 14–15 times every day and thereby provide a full coverage of Antarctica.

Figures 5.1 and 5.2 show examples of the average retrieved total water vapor over Antarctica. The seasonal variation of water vapor content in the atmosphere is clearly visible. In the short austral summer, from November to January, the Antarctic atmosphere contains significantly more water vapor than in other seasons. This is related to the high air temperatures in summer. Over the elevated plateau of East Antarctica the total water vapor is much lower than over the coastal regions and ice shelves. The Antarctic peninsula is one of the regions with large water vapor burden in Antarctica throughout the year, a result of the relatively warm and moist circumpolar westerlies. Unfortunately, only a limited amount of SSM/T2 data is available. In addition to the data at the 12 days presented in Figs. 5.1 and 5.2, three batches of data are available, two days in September of 1992

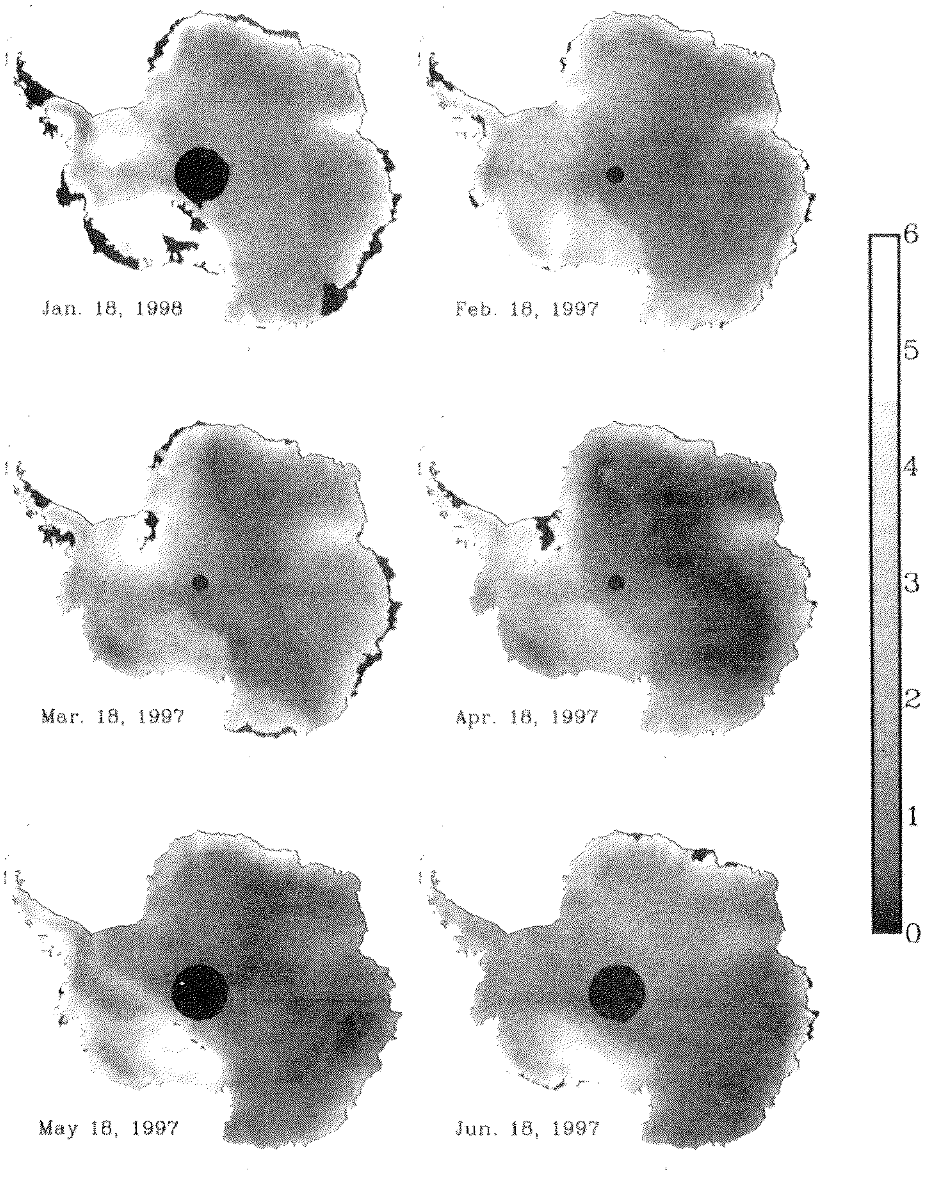

Figure 5.1: *Daily averaged total water vapor (in* kg/m^2*) over Antarctica (January to June).*

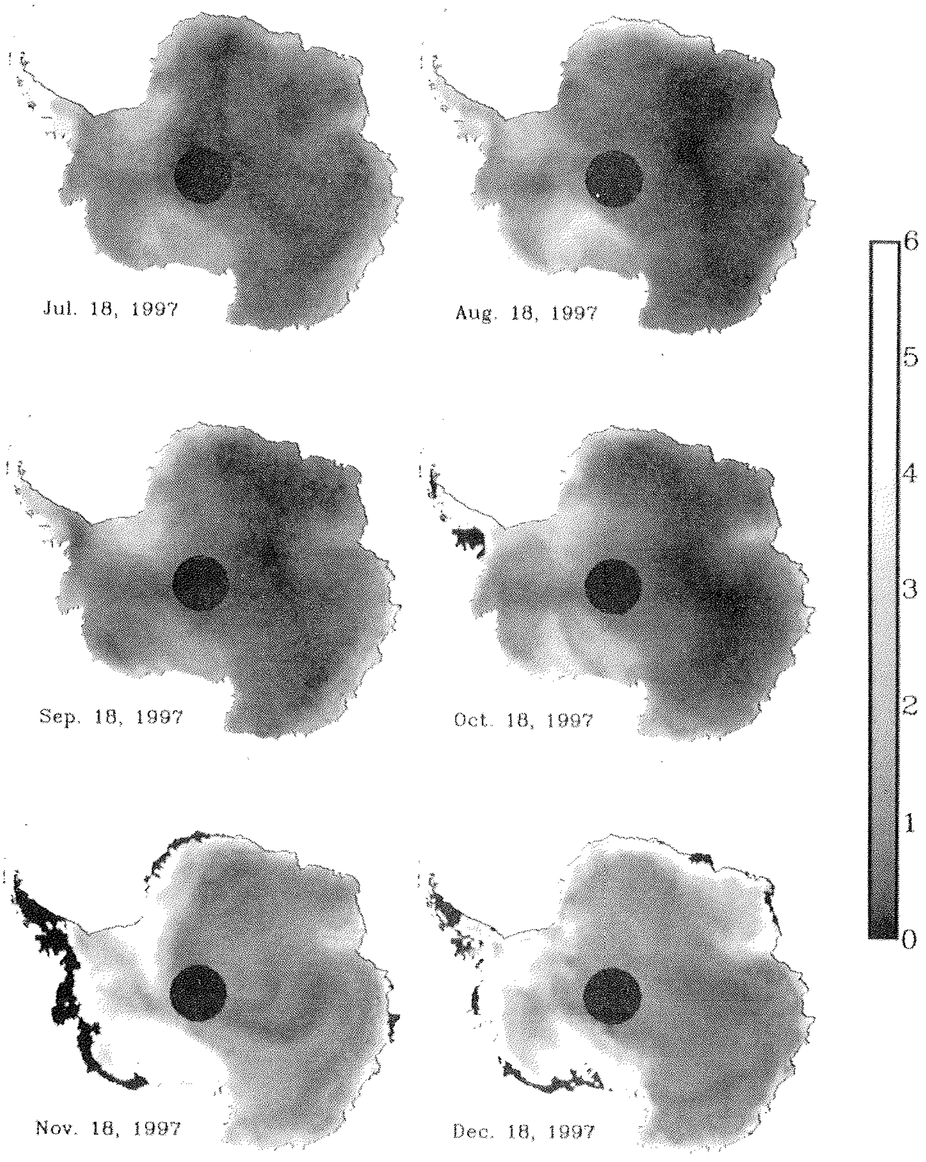

Figure 5.2: *Daily averaged total water vapor (in* kg/m^2*) over Antarctica (July to December).*

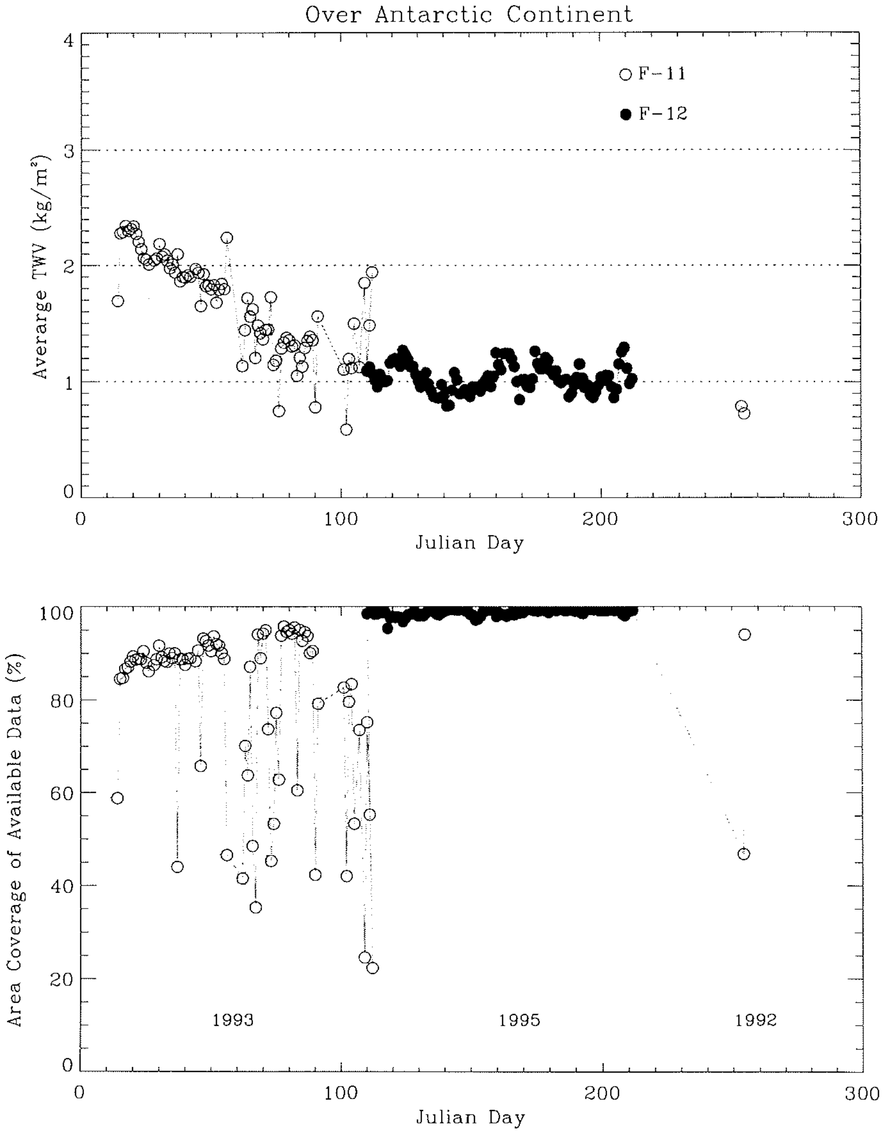

Figure 5.3: *The averaged total water vapor over the entire Antarctic continent (top) and the area coverage of available SSM/T2 data (bottom) versus the Julian day.*

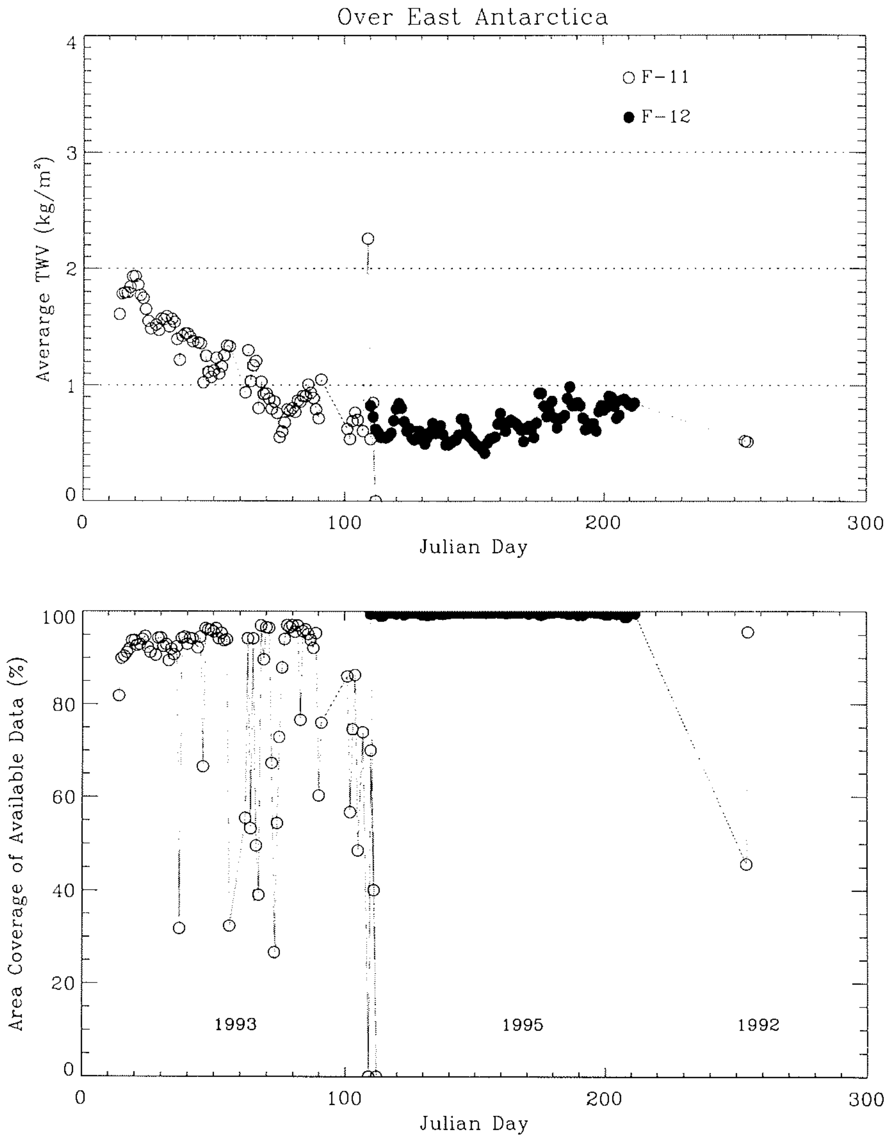

Figure 5.4: *The averaged total water vapor over the East Antarctic continent (top) and the area coverage of available SSM/T2 data (bottom) versus the Julian day.*

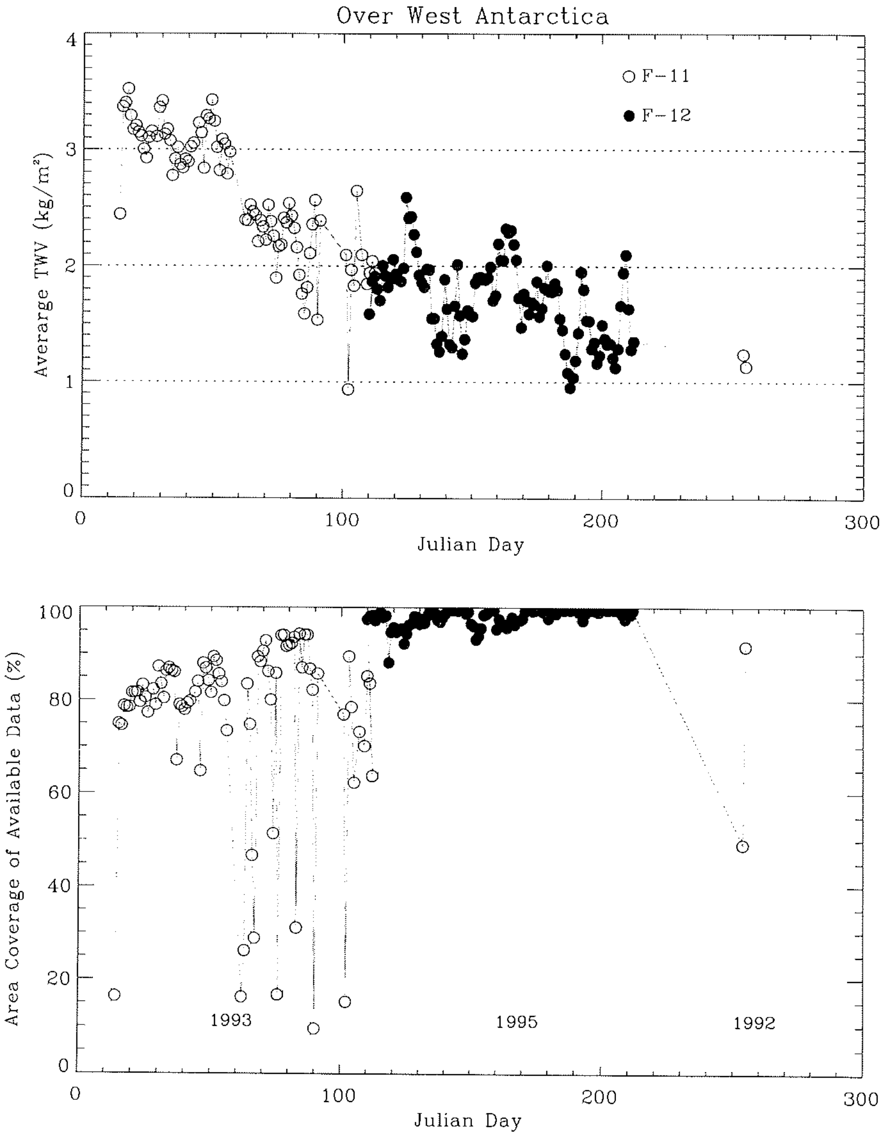

Figure 5.5: *The averaged total water vapor over the West Antarctic continent (top) and the area coverage of available SSM/T2 data (bottom) versus the Julian day.*

(F-11 spacecraft), from mid-January to the end of April of 1993 (F-11 spacecraft), and from mid-April to the end of July of 1995 (F-12 spacecraft) . Since the data spread over several years and there are large gaps, it is difficult to reach valid conclusions just using this data set. But, the general trend of Antarctic water vapor distribution can still be obtained. Figures 5.3, 5.4 and 5.5 show the average total water vapor over the whole Antarctic continent, East Antarctica and West Antarctica, respectively. Generally, the water vapor content in the atmosphere starts to decrease at about the end of January as the austral summer begins to lapse. This trend continues till about the beginning of April. Later, there is no significant trend at least until the end of July. The day-to-day variation of average total water vapor over West Antarctica is significantly larger than over East Antarctica, an indication that the physical process associated with precipitation and water vapor transport to the continent is much more active in West Antarctica than in East Antarctica. A remarkable feature is that, over West Antarctica, the total amount of water vapor in the atmosphere is greater than over East Antarctica throughout most of the time period of the available satellite data (see Fig. 5.6), compared with the fact that West Antarctica comprises only 35% of the total area of the entire Antarctic continent.

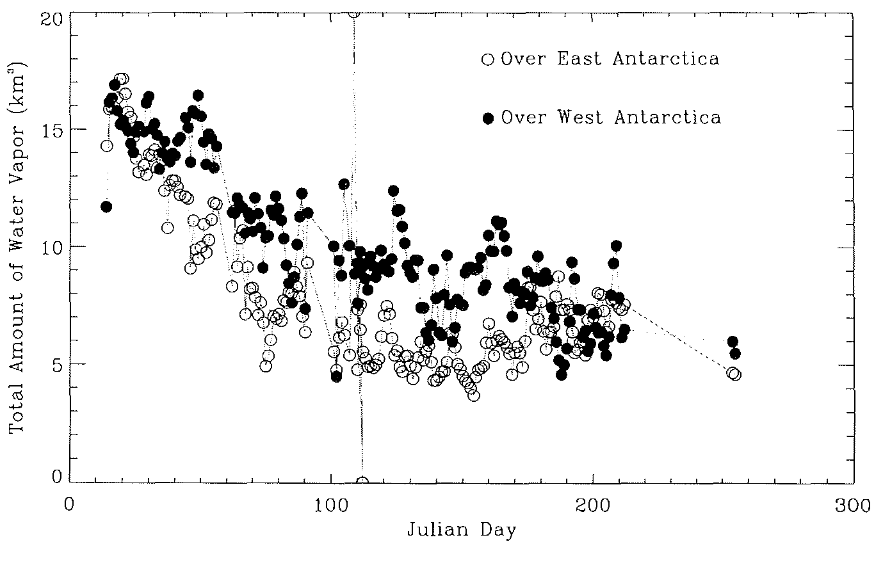

Figure 5.6: *The total amount of water vapor in the Atmosphere over East and West Antarctica. Note, 1 km*^{3} *of water equals* 10^{12} *kg.*

5.2 Future Developments

With the RCBTD method it becomes possible to determine the atmospheric water vapor content in polar regions from space. However, more work is needed. First of all, the algorithm has to be further validated through direct comparisons between instantaneous measurements of SSM/T2 and those of other instruments like radiosonde and ground-based microwave radiometers. Comparing the daily averaged total water vapor retrieved from SSM/T2 data with the results from the European Center for Medium Range Weather Forecasts (ECMWF) may be another way to validate the algorithm. In addition, the influences of clouds, especially strong ice clouds, need to be examined quantitatively. Finally, a more detailed knowledge of the emission properties of ice at the SSM/T2 frequencies can reduce the errors introduced into the retrieval process.

Another important subject in the future is to extend the retrieval range of water vapor. The high sensitivities of the 183.31 GHz channels to water vapor have limited the retrievals to cases with total water vapor burden less than $\sim 6.0\,\mathrm{kg/m^2}$. Over sea ice, the atmosphere is much humid than over the Antarctic continent and over pack ice. In regions near sea ice edges, the total water vapor can reach up to $10\,\mathrm{kg/m^2}$. In these cases, channels with a lower sensitivity to water vapor have to be used. However, due to the considerable differences between the surface emissivities of sea ice at 91.655 GHz and at 150 GHz, the 91.655 GHz channel of SSM/T2 can not be used successfully. Another approach might be to use the SSM/I instrument flown simultaneously with SSM/T2. SSM/I has both vertically and horizontally polarized channels at 85.5 GHz, which is very close to 91.655 GHz. The synergy of SSM/T2 and SSM/I should be further explored, although the two instruments have different resolution, polarization and scan geometry (*Wessel and Boucher*, 1998). Furthermore, it might also be an advantage to incorporate the measurements of the Special Sensor Microwave/Temperature (SSM/T1), because it can provide the information on the average air temperature in the troposphere.

Appendix A

Radiative Transfer Model MWMOD

The microwave radiative transfer simulation program MWMOD (MicroWave MODel) was originally developed by *Simmer* [1994]. Recently, this model was further enhanced by incorporating a sea ice simulation package based on a program developed by Grenfell (*Fuhrhop et al.*, 1998). The enhanced version of MWMOD allows the study of microwave signatures for polar regions including the effects of sea ice, ocean and atmosphere.

Detailed descriptions of how to use MWMOD can been found in the user manual (*Fuhrhop and Simmer*, 1996). Below, just the most important points related to the simulations done in this thesis using MWMOD are summarized.

- MWMOD frequency selection. The user can set the desired frequencies in the input file in section IAPGEN following the parameter "FRE". If the calculation is desired to be done within a frequency band, MWMOD can be programmed to run at a series of frequencies with a user defined stepsize. All calculations presented in this dissertation were done at the center frequencies of the SSM/T2 channels. The satellite viewing angle can also be specified in this section using parameters "IANG" and "ANG".

- MWMOD calculates the surface emission using the parameters given in sections ENVOCE and IAPOCE for oceans, and in sections ENVICE and IAPICE for sea ice. This procedure can be simplified by just setting the ground surface temperature and the ground surface reflectivity in sections ENVOCE and IAPOCE. By setting "IREF=1" in section IAPOCE, the ground surface is taken to be specular.

- The atmospheric temperature, humidity and pressure profiles can be set internally or read from an external file, which is determined by the parameter "IATMOS" in section ENVATM. MWMOD includes standard atmospheric profiles; but, it also allows to use profiles provided by the user. The atmospheric profiles can be interpolated at user defined layers by selecting the parameter "IMESH". This feature is useful when clouds are included in the calculation.

- By setting the parameter "IHYDFIX" to 1 in section ENVATM, clouds can be introduced into the calculation according to the parameters given in section FIXED CLOUDS. Cloud top and bottom heights are controlled by the parameters "ICT" and "ICB"; the phase of hydrometeors in clouds is controlled by parameter "PHASE"; and the water content of clouds can be specified by "LWH". The different types of clouds are simulated using the dropsize distribution models supported by MWMOD. In studying the effects of polar clouds on SSM/T2 channels, the models of *Ulaby et al.* [1981] for midlatitude cirrostratus and stratus were used for polar ice and low altitude water clouds, respectively; the model of *Chylek and Ramaswamy* [1982] for altostratus was used for high altitude water clouds in polar regions.

- MWMOD can calculate brightness temperatures or weighting functions, which are controlled by the parameter "IOPT" in section RADTRA. The scattering effect of hydrometeors can be included or excluded in the calculation through selecting the parameter "ISCAT". The scattering effect was always taken into account in the simulations presented in this thesis.

A Sample Input File of MWMOD

```
*************************************************************************
 R T M W      input specifications
 IPR   =  1
 NMOD1=   1 NMOD2= 156 NMODD=   1
*************************************************************************
* E N V G E N  input specifications
* Part 1 : Input for ENVATM
* Part 2 : Input for ENVOCE
* Part 3 : Input for ENVICE
*************************************************************************
 E N V A T M    input specifications
 IPR   =  1 IRUN  =  1
 ITEM  =  0 PO=1000.00 TO=   3.15 GAMT= 6.50 ZTINV=10.0 DTO   = 1.00
 IATMOS=  1 IPROF=   1 FILE     =../simu/ssmt2/input/polar.dat
 IWV   =  0 RHS=010.00 PCO=  1.00 PWV= 05.00
 ITOP  =  0
 IPBL  =  0 HPBL=2.000 TP= 273.00 GPBL= 3.00 QPBL= 2.00
 IHYDAN=  0 IHYDFX=  1 RHCL= 85.0
 IMESH =  2 NNZL  =100 FZ=  0.000 DZ=  0.100
 ENDG
 ZMESH
 ZM =
   0.000   0.030   0.060   0.100   0.400   0.700   1.000   1.500
   2.000   2.500   3.000   3.500   4.000   4.500   5.000   5.500
   6.000   6.500   7.000   7.500   8.000   8.500   9.000   9.500
```

```
  10.000  11.000  12.000  13.000  14.000  15.000  16.000  17.000
  18.000  19.000  20.000  25.000  30.000  40.000  50.000
 ENDG

 PROFILE
 NL    = 18
 Z     =
   0.000   0.300   1.000   2.000   3.000   3.760   4.000   5.000
   6.000   7.000   8.000   9.000   9.930  10.000  11.000  12.000
  13.000  14.000  15.000
 P     =
 -99.999 -99.999 -99.999 -99.999 -99.999 -99.999 -99.999 -99.999
 -99.999 -99.999 -99.999 -99.999 -99.999 -99.999 -99.999 -99.999
 -99.999 -99.999 -99.999
 TL    =
 290.000 287.600 284.800 280.700 276.500 273.100 271.900 267.100
 262.000 256.500 250.600 244.200 238.000 237.400 229.400 221.400
 221.400 221.400 221.400
 RHL   =
  49.200 100.000 100.000 100.000 100.000 100.000 100.000 100.000
 100.000 100.000 100.000 100.000 100.000   5.600   6.500   5.200
   2.700   1.400
 ENDG
************************************************************************
 FIXED CLOUDS
 NCL   =  1
# ICT ICB     LWH LWHT PHASEF XSECT PHASE SIZEDIS
   30  11  00.300    1      4     2     1      12
 ENDG
************************************************************************
 E N V O C E   input specifications
 IPR   =  1 IRUN  =  0
 SAL= 33.00 WND= 14.00 SST=273.15 DST=  0.00 IWND  =  0 ISST  = 0
 ENDG
************************************************************************
 E N V I C E       input specifications
 IPR   =  1 IRUN  =  0
 IICE  =  0 ICEPRO=  1 FILE  =..
 ENDG
************************************************************************
 ICEPROFILE
 NLICE = 13
#      Z       T    RHO   DSN   FWFR     DG DBUB    SI THETB       BRAT   N
  -2.500  269.9  1.000  0.00  1.000   0.00  0.0  32.0   0.0  0.000E+00   1
  -1.580  266.1  0.870  0.00  0.000  10.00  1.2   3.0  24.0  0.250E-04   2
  -1.020  265.7  0.870  0.00  0.000  10.00  1.2   2.4  24.0  0.250E-04   3
  -0.970  265.4  0.890  0.00  0.000  10.00  1.2   1.9  24.0  0.250E-04   4
  -0.870  265.1  0.890  0.00  0.000  10.00  1.2   1.4  24.0  0.250E-04   5
  -0.770  264.8  0.895  0.00  0.000  10.00  1.2   1.2  24.0  0.250E-04   6
```

```
  -0.630  264.5  0.895  0.00  0.000  10.00  1.2   0.7  24.0  0.250E-04   7
  -0.460  264.1  0.895  0.00  0.000  10.00  1.2   0.3  24.0  0.250E-04   8
  -0.380  263.7  0.895  0.00  0.000  10.00  1.2   0.1  24.0  0.250E-04   9
  -0.200  263.5  0.728  3.00  0.000   0.00  3.0   0.0  54.7  0.100E+01  10
  -0.150  263.3  0.460  6.00  0.000   0.00  5.0   0.0  54.7  0.100E+01  11
  -0.100  263.1  0.100  6.00  0.000   0.00  1.2   0.0   0.0  0.100E+01  12
  -0.000  263.1  0.100  6.00  0.000   0.00  1.2   0.0   0.0  0.100E+01  13
 ENDG
*************************************************************************
* I A P G E N input specifications                                      *
* Part 1 : Input for IAPATM                                             *
* Part 2 : Input for IAPOCE                                             *
* Part 3 : Input for IAPICE                                             *
*************************************************************************
 I A P G E N    input specifications
 IPR    =  1 IRUN   =  1
 IFRE   =  1 NFRE   =  5 FN= 00.000 DN= 00.000
 IANG   =  2 NANG   =  3 FA= 01.700 DA= 00.000
 FRE    =
 91.655  150.00  176.31  180.31  182.31
 ANG    =
 01.700  08.490  18.730  29.130  36.220  47.260
 ENDG
*************************************************************************
 I A P A T M     input specifications
 IPR    =  1 IRUN   =  1
 MODHYM=  2 IPHAMA=  2
 TWV=001.00 TO2=001.00 THY=001.00
 ENDG
*************************************************************************
 I A P O C E   input specifications
 IPR    =  1 IFLAG =  1
 IREF   =  1 IEPSIL= -2 FEPV=0.100 DEPV=0.050 FEPH=0.250 DEPH=0.050
 IFOAM =  4
 ENDG
 REFV
 0.024 0.026 0.035 0.033 0.500 0.500 0.500 0.500 0.500 0.500
 ENDG
 REFH
 0.060 0.060 0.060 0.051 0.500 0.500 0.500 0.500 0.500 0.500
 ENDG
*************************************************************************
 I A P I C E   input specifications
 IPR    =  1 IFLAG =  0
 ITEMIS=  6 IELEV =  6 TEMPE = 273.13
 IIREF =  1
 ENDG
 EMISTEMP
 272.13 271.13 270.13 269.13
```

```
 ENDG
****************************************************************************
 R A D T R A   input specifications
 IPR   =  1 IRUN  =  1
 IOPT  =  1 IWFT  = 11 ISCAT = 1 IPHAC = 1 IPHA  = 2 TBSP= 2.70 DMX=0.010
 ICOV  =  0 COVI  = 0.00
****************************************************************************
```

References

Aerojet GenCorp. *Retrieval of Relative Humidity Profiles from the SSM/T1, SSM/T2 and SSM/I System*, 1987. Report to the Department of the Air Force.

Aerojet GenCorp. *System Summary Report for the SSM/T2 Water Vapor Profiling Sensor Hardware Segment*, 1990. Report to the Department of the Air Force.

AGU. *Water Vapor in the Climate System*, 1995. Special Report.

Alishouse, J. C., Sinder, J. B., Westwater, E. R., Swift, C. T., Ruf, C. S., Snyder, S. A., Vongsathorn, J., and Ferraro, R. R., Determination of Cloud Liquid Water Content Using the SSM/I. *IEEE Transactions on Geoscience and Remote Sensing*, **28**(5), 817–821, 1990.

Bauer, A., Godon, M., Carlier, J., and Gamache, R. R., Continuum in the Windows of the Water Vapor Spectrum: Absorption of H_2O-Ar at 239 GHz and Linewidth Calculations. *J. Quant. Spectrosc. Radiat. Transfer*, **59**(3–5), 273–285, 1998.

Bauer, P., and Schluessel, P., Rainfall, Total Water, Ice Water, and Water Vapor Over Sea From Polarized Microwave Simulations and Special Sensor Microwave/Imager Data. *Journal of Geophysical Research*, **98**(D11), 20,737–20,759, 1993.

Bromwich, D. H., Estimates of Antarctic Precipitation. *Nature*, **343**, 627–629, 1990.

Brussaard, G., and Watson, P. A., *Atmospheric Modeling and Millimeter Wave Propagation*. Chapman and Hall, 1995.

Buehler, S., *The Impact of Continuum Emissions in the mm and Sub-mm Spectral Range*. IUP, University of Bremen, 1996. Final Report to ESA.

Cabrera-Mercader, C. R., and Staelin, D. H., Passive Microwave Relative Humidity Retrievals Using Feedforward Neural Networks. *IEEE Transactions on Geoscience and Remote Sensing*, **33**(6), 1324–1328, 1995.

Chang, A. T. C., Gloersen, P., and Schmugge, T., Microwave Emission from Snow and Glacier Ice. *Journal of Glaciology*, **16**, 23–39, 1976.

Chang, A. T. C., and Wilheit, T. T., Remote Sensing of Atmospheric Water Vapor, Liquid Water, and Wind Speed at the Ocean Surface by Passive Microwave Techniques from the Nimbus-5 Satellite. *Radio Science*, **14**(5), 793–802, 1979.

Chedin, A., Scott, N. A., Cheruy, F., and Tourier, B., The Advanced-3I Method for the Processing of Next Generation Sounder Observations. In A. Chedin, M. T. C., and Scott, N. A., editors, *High Spectral Resolution Infrared Remote Sensing for Earth's Weather and Climate Studies*, pages 63–83. 1993.

Chylek, P., and Ramaswamy, V., Simple Approximation for Infrared Emissivity of Water Clouds. *Journal of Atmospheric Science*, **39**, 171–177, 1982.

Comiso, J. C., Grenfell, T. C., Bell, D. L., Lange, M. A., and Ackley, S. F., Passive Microwave *in situ* Observations of Winter Weddell Sea Ice. *Journal of Geophysical Research*, **94**(C8), 10,891–10,905, 1989.

Comiso, J. C., Sea Ice Effective Microwave Emissivities from Satellite Passive Microwave and Infrared Observations. *Journal of Geophysical Research*, **88**(C12), 7686–7704, 1983.

Comiso, J. C., Surface Temperatures in the Polat Regions from Nimbus-7 Temperature Humidity Infrared Radiometer. *Journal of Geophysical Research*, **99**(C3), 5181–5200, 1994.

Connolley, W. M., and King, J. C., Atmospheric Water Vapor Transport to Antarctica Inferred from Radiosonde Data. *Q. J. R. Meteorol. Soc.*, **119**, 325–342, 1993.

Curry, J. A., Ardeel, C. D., and Tian, L., Liquid Water Content and Precipitation Characteristics of Stratiform Clouds as Inferred from Satellite Microwave Measurements. *J. Geophys. Res.*, **95**, 16,659–16,671, 1990.

Eichen, H., Lange, A., Hubberten, H.-W., and Wadhams, P., Characteristics and Distribution Patterns of Snow and Meteoric Ice in the Weddell Sea and Their Contribution to the Mass Balance of Sea Ice. *Ann. Geophysicae*, **12**, 82–93, 1994.

Felde, G. W., and Pickle, J. D., Retrieval of 91 and 150 GHz Surface Emissivities. *Journal of Geophysical Research*, **100**(D10), 20,855–20,866, 1995.

Foerster, A., Methoden zur Wiedererkenung von Wasserdampfprofilen aus Radiosonden Daten in Satellitendaten. Master's thesis, IUP, University of Bremen, 1997.

Fuhrhop, R., Simmer, C., Schrader, M., Heygster, G., Johnsen, K.-P., and Schluessel, P., Study of Passive Remote Sensing of the Atmosphere and the Surface Ice. *Report from the Institute of Oceanography, University of Kiel*, **297**, 1997.

Fuhrhop, R., Grenfell, T. C., Heygster, G., Johnsen, K.-P., Schluessel, P., Schrader, M., and Simmer, C., A Combined Radiative Transfer Model for Sea Ice, Open Water, and Atmosphere. *Radio Science*, **33**(2), 303–316, 1998.

Fuhrhop, R., and Ruprecht, E., An Improved Total Precipitable Water Algorithm for Cloudy Situations. In Solimini, D., editor, *Microwave Radiometry and Remote Sensing of the Environment*, pages 165–173. 1995.

Fuhrhop, R., and Simmer, C., *MWMOD User Manual.* Version 1.10, 1996.

Gasiewski, A. J., Microwave Radiation Transfer in Hydrometeors. In Janssen, M. A., editor, *Atmospheric Remote Sensing by Microwave Radiometry*, pages 91–143. 1993.

Gibbins, C. J., Improved Algorithms for the Determination of Specific Attenuation at Sea Level by Dry Air and Water Vapor, in the Frequency Range 1-350 GHz. *Radio Science*, **21**(6), 949–954, 1986.

Giovinetto, M. B., Yamazaki, K., Wendler, G., and Bromwich, D. H., Atmospheric Net Transport of Water Vapor and Latent Heat across 60°S. *Journal of Geophysical Research*, **102**(D10), 11,171–11,179, 1997.

Greenwald, T. J., Stephens, G. L., Haar, T. H. V., and Jackson, D. L., A Physical Retrieval of Cloud Liquid Water Over the Global Oceans Using Special Sensor Microwave/Imager (SSM/I) Observations. *Journal of Geophysical Research*, **98**(D10), 18,471–18,488, 1993.

Grenfell, T. C., Comiso, J. C., Lange, M. A., Eicken, H., and Wensnahan, M. R., Passive Microwave Observations of the Weddell Sea during Austral Winter and Early Spring. *Journal of Geophysical Research*, **99**(C5), 9995–10,010, 1994.

Grody, N. C., Remote Sensing of Atmospheric Water Content From Satellites Using Microwave Radiometry. *IEEE Transactions on Antennas and Propagation*, **AP-24**(2), 155–162, 1976.

Guasta, M. D., Morandi, M., Stefanutti, L., Brechet, J., and Piquad, J., One Year of Cloud Data from Dumont d'Urville (Antarctica): 1. General Overview of Geometrical and Optical Properties. *Journal of Geophysical Research*, **98**(D10), 18,575–18,587, 1993.

Guissard, A., and Sobieski, P., A Simplified Radiative Transfer Equation for Application in Ocean Microwave Remote Sensing. *Radio Science*, **29**(4), 881–894, 1994.

Hall, D. K., and Martinec, J., *Remote Sensing of Ice and Snow*. Chapman and Hall, 1985.

Hewison, T. J., and English, S. J., Results of a Microwave Airborne Campaign over Snow and Ice. *submitted to IEEE Transaction on Geoscience and Remote Sensing*, 1998.

Johnsen, K.-P., Darovskikh, A., Heygster, G., and Wiesmann, A., Microwave Measurements of Sea Ice in the Kara and Laptev Sea. *IEEE International Geoscience and Remote Sensing Symposium Proceedings*, **4**, 1675–1677, 1997.

Kakar, R. K., Retrieval of Clear Sky Moisture Profiles Using the 183 GHz Water Vapor Line. *Journal of Climate and Applied Meteorology*, **22**, 1282–1983, 1983.

Key, J. R., Schweiger, A. J., and Stone, R. S., Expected Uncertainty in Satellite-derived Estimates of the Surface Radiation Budget at High Latitudes. *Journal of Geophysical Research*, **102**(C7), 15,837–15,847, 1997.

Key, J., and Haefliger, M., Arctic Ice Surface Temperature Retrieval from AVHRR Thermal Channels. *Journal of Geophysical Research*, **97**(D5), 5885–5893, 1992.

King, J. C., and Turner, J., *Antarctic Meteorology and Climatology*. Cambridge University Press, 1997.

Klein, L. A., and Swift, C. T., An Improved Model for the Dielectric Constant of Sea Water at Microwave Frequencies. *IEEE Transactions on Antenna and Propagation*, **25**(1), 104–111, 1977.

Kramer, H. J., *Observation of the Earth and Its Environment*. Springer, 1996.

Kuo, C. C., Staelin, D. H., and Rosenkranz, P. W., Statistical Iterative Schem for Estimating Atmospheric Relative Humidity Profiles. *IEEE Transactions on Geoscience and Remote Sensing*, **32**(2), 254–260, 1994.

Liebe, H. J., MPM—An Atmospheric Millimeter-Wave Propagation Model. *International Journal of Infared and Millimeter Waves*, **10**(6), 631–650, 1989.

Liu, W. T., Tang, W., and Wentz, F. J., Precipitable Water and Surface Humidity over Global Oceans from Special Sensor Microwave Image and European Center for Medium Range Weather Forecasts. *Journal of Geophysical Research*, **97**(C2), 2251–2264, 1992.

Maslanik, J., and Key, J., Comparison and Integration of Ice-pack Temperatures Derived from AVHRR and Passive Microwave Imagery. *Annals of Glaciology*, **17**, 372–378, 1993.

Massom, R., and Comiso, J. C., The Classification of Arctic Sea Ice Types and the Determination of Surface Temperature Using Advanced Very High Resolution Radiometer Data. *Journal of Geophysical Research*, **99**(C3), 5200–5218, 1994.

Prabhakara, C., Chang, H. D., and Chang, A. T. C., Remote Sensing of Precipitable Water over the Oceans from Nimbus-7 Microwave Measurements. *J. Appl. Meteorol.*, **21**, 59–68, 1982.

Price, J. C., Quantitative Aspects of Remote Sensing in the Thermal Infrared. In Asrar, G., editor, *Theory and Applications of Optical Remote Sensing*, pages 578–603. 1989.

Robinson, I. S., *Satellite Oceanography.* Ellis Horwood Limited, 1985.

Rosenkranz, P. W., Staelin, D. H., and Grody, N. C., Typhoon June (1975) Viewed by a Scanning Microwave Spectrometer. *Journal of Geophysical Research*, **83**(C4), 1857–1868, 1978.

Rossow, W. R., Remote Sensing of Atmospheric Water Vapor. In Raschke, E., editor, *Radiation and Water in the Climate System*, pages 175–191. 1996.

Ruprecht, E., and Jung, T., Anwendung neuronaler Netze zur Ableitung hydrometeorologischer Parameter. *Arbeitsbricht von HYPAM*, pages 131–144, 1997.

Schaerer, G., and Wilheit, T. T., A Passive Microwave Technique for Profiling of Atmospheric Water Vapor. *Radio Science*, **14**(3), 371–375, 1979.

Schluessel, P., and Emery, W. J., Atmospheric Water Vapor over Oceans from SSM/I Measurements. *Int. J. Remote Sensing*, **11**(5), 753–766, 1990.

Schlueter, N., and Markus, T., Cloud Masking with Satellite Infrared Images over Polar Oceans. *IEEE International Geoscience and Remote Sensing Symposium Proceedings*, **2**, 1247–1249, 1996.

Schwerdtfeger, W., *Weather and Climate of the Antarctic.* Elsevier Science Publishers B. V., 1984.

Simmer, C., *Satellitenfernerkundung hydrologischer Parameter der Atmosphaere mit Mikrowellen.* Verlag Dr. Kovac, 1994.

Staelin, D. H., Kunzi, K. F., Pettyjohn, R. L., Poon, R. K. L., Wilcox, R. W., and Waters, J. W., Remote Sensing of Atmospheric Water Vapor and Liquid Water with the Nimbus 5 Microwave Spectrometer. *J. Appl. Meteorol.*, **15**, 15,1204–15,1214, 1976.

Stone, R. S., Properties of Austral Winter Clouds Derived from Radiometric Profiles at the South Pole. *Journal of Geophysical Research*, **98**(D7), 12,961–12,971, 1993.

Tjemkes, S. A., Stephens, G. L., and Jackson, D. L., Spaceborne Observation of Columnar Water Vapor: SSMI Observations and Algorithm. *Journal of Geophysical Research*, **96**(D6), 10,941–10,954, 1991.

TOVS Working Group. *A Report on the Eighth International TOVS Study Conference*, 1995. Gueenstown, New Zealand.

Troy, B. E., Hollinger, J. P., Lerner, R. M., and Wisler, M. M., Measurement of the Microwave Properties of Sea Ice at 90 GHz and Lower Frequencies. *Journal of Geophysical Research*, **86**(C5), 4283–4289, 1981.

Ulaby, F. T., Moore, R. K., and Fung, A. K., *Microwave Remote Sensing: Active and Passive.* Artech House, Inc., 1981.

Wang, J. R., King, J. L., Wilheit, T. T., Szejwach, G., Gesell, L. H., Nieman, R. A., Niver, D. S., Krupp, B. M., and Gagliano, J. A., Profiling Atmospheric Water Vapor by Microwave Radiometry. *Journal of Climate and Applied Meteorology*, **22**, 779–788, 1983.

Wang, J. R., Wilheit, T. T., and Chang, L. A., Retrieval of Total Precipitable Water Using Radiometric Measurements Near 92 and 183 GHz. *Journal of Applied Meteorology*, **28**, 146–154, 1989.

Wang, J. R., Boncyk, W. C., and Sharma, A. K., Water Vapor Profiling over Ocean Surface from Airborne 90 and 183 GHz Radiometric Measurements Under Clear and Cloudy Conditions. *IEEE Transactions on Geoscience and Remote Sensing*, **31**(4), 853–858, 1993.

Wang, J. R., Racette, P., and Chang, A., Profiling of Atmospheric Water Vapor with the Millimeter-wave Imaging Radiometer. In Solimini, D., editor, *Microwave Radiometry and Remote Sensing of the Environment*, pages 33–41. 1995.

Wang, J. R., Racette, P., and Chang, A., MIR Measurements of Atmospheric Water Vapor Profiles. *IEEE Transactions on Geoscience and Remote Sensing*, **35**(2), 212–223, 1997a.

Wang, J. R., Racette, P., Triesky, M. E., Browell, E. V., Ismail, S., and Chang, L. A., Simultaneous Measurements of Water Vapor Profiles from Airborne MIR and LASE. *IEEE International Geoscience and Remote Sensing Symposium Proceedings*, **4**, 1969–1971, 1997b.

Wang, J. R., and Chang, L. A., Retrieval of Water Vapor Profiles from Microwave Radiometric Measurement near 90 and 183 GHz. *J. Appl. Meteorol.*, **29**(10), 1006–1013, 1990.

Wessel, J. E., and D. Boucher, J., Comparison between Cross-Track and Conical Scanning Microwave Window Channels near 90 GHz. *IEEE Transactions on Geoscience and Remote Sensing*, **36**(1), 16–24, 1998.

Westwater, E. R., Ground-based Microwave Remote Sensing of Meteorological Variables. In Janssen, M. A., editor, *Atmospheric Remote Sensing by Microwave Radiometry*, pages 145–213. 1993.

Wilheit, T. T., and Hutchison, K. D., Water Vapor Profile Retrievals from SSM/T2 Data Constrained by Infrared-based Cloud Parameters. *Int. J. Remote Sensing*, **18**(15), 3263–3277, 1997.

Wilheit, T. T., An Algorithm for Retrieving Water Vapor Profiles in Clear and Cloudy Atmospheres from 183 GHz Radiometric Measurements: Simulation Studies. *Journal of Applied Meteorology*, **29**, 508–515, 1990.

Yu, Y., Rothrock, D. A., and Lindsay, R. W., Accuracy of Sea Ice Temperature Derived from the Advanced Very High Resolution Radiometer. *Journal of Geophysical Research*, **100**(C3), 4525–4532, 1995.

Zwally, H. J., Microwave Emissivity and Accumulation Rate of Polar Firn. *Journal of Glaciology*, **18**(79), 195–215, 1977.

Folgende Hefte der Reihe „Berichte zur Polarforschung“ sind bisher erschienen:

• **Sonderheft Nr. 1/1981** – „Die Antarktis und ihr Lebensraum“
Eine Einführung für Besucher – Herausgegeben im Auftrag von SCAR

Heft Nr. 1/1982 – „Die Filchner-Schelfeis-Expedition 1980/81“
zusammengestellt von Heinz Kohnen

• **Heft-Nr. 2/1982** – „Deutsche Antarktis-Expedition1980/81 mit FS ‚Meteor‘“
First International BIOMASS Experiment (FIBEX) – Liste der Zooplankton- und Mikronektonnetzfänge
zusammengestellt von Norbert Klages.

Heft Nr. 3/1982 – „Digitale und analoge Krill-Echolot-Rohdatenerfassung an Bord des Forschungsschiffes ‚Meteor‘“ (im Rahmen von FIBEX 1980/81, Fahrtabschnitt ANT III), von Bodo Morgenstern

Heft Nr. 4/1982 – „Filchner-Schelfeis-Expedition 1980/81“
Liste der Planktonfänge und Lichtstärkemessungen
zusammengestellt von Gerd Hubold und H. Eberhard Drescher

• **Heft Nr. 5/1982** – "Joint Biological Expedition on RRS 'John Biscoe', February 1982"
by G. Hempel and R. B. Heywood

• **Heft Nr. 6/1982** – „Antarktis-Expedition 1981/82 (Unternehmen ‚Eiswarte‘)“
zusammengestellt von Gode Gravenhorst

Heft Nr. 7/1982 – „Marin-Biologisches Begleitprogramm zur Standorterkundung 1979/80 mit MS ‚Polarsirkel‘ (Pre-Site Survey)“ – Stationslisten der Mikronekton- und Zooplanktonfänge sowie der Bodenfischerei
zusammengestellt von R. Schneppenheim

Heft Nr. 8/1983 – "The Post-Fibex Data Interpretation Workshop"
by D. L. Cram and J.-C. Freytag with the collaboration of J. W. Schmidt, M. Mall, R. Kresse, T. Schwinghammer

* **Heft Nr. 9/1983** – "Distribution of some groups of zooplankton in the inner Weddell Sea in summer 1979/80"
by I. Hempel, G. Hubold, B. Kaczmaruk, R. Keller, R. Weigmann-Haass

Heft Nr. 10/1983 – „Fluor im antarktischen Ökosystem“ – DFG-Symposium November 1982
zusammengestellt von Dieter Adelung

Heft Nr. 11/1983 – "Joint Biological Expedition on RRS 'John Biscoe', February 1982 (II)"
Data of micronecton and zooplankton hauls, by Uwe Piatkowski

Heft Nr. 12/1983 – „Das biologische Programm der ANTARKTIS-I-Expedition 1983 mit FS ‚Polarstern‘“
Stationslisten der Plankton-, Benthos- und Grundschleppnetzfänge und Liste der Probennahme an Robben und Vögeln, von H. E. Drescher, G. Hubold, U. Piatkowski, J. Plötz und J. Voß

• **Heft Nr. 13/1983** – „Die Antarktis-Expedition von MS ‚Polarbjörn‘ 1982/83“ (Sommerkampagne zur Atka-Bucht und zu den Kraul-Bergen), zusammengestellt von Heinz Kohnen

• **Sonderheft Nr. 2/1983** – „Die erste Antarktis-Expedition von FS ‚Polarstern‘ (Kapstadt, 20. Januar 1983 – Rio de Janeiro, 25. März 1983)“, Bericht des Fahrtleiters Prof. Dr. Gotthilf Hempel

Sonderheft Nr. 3/1983 – „Sicherheit und Überleben bei Polarexpeditionen“
zusammengestellt von Heinz Kohnen

* **Heft Nr. 14/1983** – „Die erste Antarktis-Expedition (ANTARKTIS I) von FS ‚Polarstern‘ 1982/83“
herausgegeben von Gotthilf Hempel

Sonderheft Nr. 4/1983 – "On the Biology of Krill *Euphausia superba*" – Proceedings of the Seminar and Report of the Krill Ecology Group, Bremerhaven 12.–16. May 1983, edited by S. B. Schnack

Heft Nr. 15/1983 – "German Antarctic Expedition 1980/81 with FRV 'Walther Herwig' and RV 'Meteor'" – First International BIOMASS Experiment (FIBEX) – Data of micronekton and zooplankton hauls
by Uwe Piatkowski and Norbert Klages

Sonderheft Nr. 5/1984 – "The observatories of the Georg von Neumayer Station", by Ernst Augstein

Heft Nr. 16/1984 – "FIBEX cruise zooplankton data"
by U. Piatkowski, I. Hempel and S. Rakusa-Suszczewski

Heft Nr. 17/1984 – „Fahrtbericht (cruise report) der ‚Polarstern‘-Reise ARKTIS I, 1983“
von E. Augstein, G. Hempel und J. Thiede

Heft Nr. 18/1984 – „Die Expedition ANTARKTIS II mit FS ‚Polarstern‘ 1983/84“,
Bericht von den Fahrtabschnitten 1, 2 und 3, herausgegeben von D. Fütterer

Heft Nr. 19/1984 – „Die Expedition ANTARKTIS II mit FS ‚Polarstern‘ 1983/84“,
Bericht vom Fahrtabschnitt 4, Punta Arenas–Kapstadt (Ant-II/4), herausgegeben von H. Kohnen

Heft Nr. 20/1984 – „Die Expedition ARKTIS II des FS ‚Polarstern‘ 1984, mit Beiträgen des FS ‚Valdivia‘ und des Forschungsflugzeuges ‚Falcon 20‘ zum Marginal Ice Zone Experiment 1984 (MIZEX)“
von E. Augstein, G. Hempel, J. Schwarz, J. Thiede und W. Weigel

Heft Nr. 21/1985 – "Euphausiid larvae in plankton samples from the vicinity of the Antarctic Peninsula, February 1982" by Sigrid Marschall and Elke Mizdalski

Heft Nr. 22/1985 – "Maps of the geographical distribution of macrozooplankton in the Atlantic sector of the Southern Ocean" by Uwe Piatkowski

Heft Nr. 23/1985 – „Untersuchungen zur Funktionsmorphologie und Nahrungsaufnahme der Larven des Antarktischen Krills *Euphausia superba* Dana“ von Hans-Peter Marschall

Heft Nr. 24/1985 – „Untersuchungen zum Periglazial auf der König-Georg-Insel Südshetlandinseln/ Antarktika. Deutsche physiogeographische Forschungen in der Antarktis. – Bericht über die Kampagne 1983/84" von Dietrich Barsch, Wolf-Dieter Blümel, Wolfgang Flügel, Roland Mäusbacher, Gerhard Stablein, Wolfgang Zick

* **Heft-Nr. 25/1985** – „Die Expedition ANTARKTIS III mit FS ‚Polarstern' 1984/1985" herausgegeben von Gotthilf Hempel.

***Heft-Nr. 26/1985** – "The Southern Ocean"; A survey of oceanographic and marine meteorological research work by Hellmer et al.

Heft Nr. 27/1986 – „Spätpleistozäne Sedimentationsprozesse am antarktischen Kontinentalhang vor Kapp Norvegia, östliche Weddell-See" von Hannes Grobe

Heft Nr. 28/1986 – „Die Expedition ARKTIS III mit ‚Polarstern' 1985" mit Beiträgen der Fahrtteilnehmer, herausgegeben von Rainer Gersonde

* **Heft Nr. 29/1986** – „5 Jahre Schwerpunktprogramm ‚Antarktisforschung' der Deutschen Forschungsgemeinschaft." Rückblick und Ausblick. Zusammengestellt von Gotthilf Hempel, Sprecher des Schwerpunktprogramms

Heft Nr. 30/1986 – "The Meteorological Data of the Georg-von-Neumayer-Station for 1981 and 1982" by Marianne Gube and Friedrich Obleitner

Heft Nr. 31/1986 – „Zur Biologie der Jugendstadien der Notothenioidei (Pisces) an der Antarktischen Halbinsel" von A. Kellermann

Heft Nr. 32/1986 – „Die Expedition ANTARKTIS IV mit FS ‚Polarstern' 1985/86" mit Beiträgen der Fahrtteilnehmer, herausgegeben von Dieter Fütterer

Heft Nr. 33/1987 – „Die Expedition ANTARKTIS-IV mit FS ‚Polarstern' 1985/86 – Bericht zu den Fahrtabschnitten ANT-IV/3–4" von Dieter Karl Fütterer

Heft Nr. 34/1987 – „Zoogeographische Untersuchungen und Gemeinschaftsanalysen an antarktischem Makroplankton" von U. Piatkowski

Heft Nr. 35/1987 – „Zur Verbreitung des Meso- und Makrozooplanktons in Oberflächenwasser der Weddell See (Antarktis)" von E. Boysen-Ennen

Heft Nr. 36/1987 – „Zur Nahrungs- und Bewegungsphysiologie von *Salpa thompsoni* und *Salpa fusiformis*" von M. Reinke

Heft Nr. 37/1987 – "The Eastern Weddell Sea Drifting Buoy Data Set of the Winter Weddell Sea Project (WWSP)" 1986 by Heinrich Hoeber und Marianne Gube-Lehnhardt

Heft Nr. 38/1987 – "The Meteorological Data of the Georg von Neumayer Station for 1983 and 1984" by M. Gube-Lenhardt

Heft Nr. 39/1987 – „Die Winter-Expedition mit FS ‚Polarstern' in die Antarktis (ANT V/1–3)" herausgegeben von Sigrid Schnack-Schiel

Heft Nr. 40/1987 – "Weather and Synoptic Situation during Winter Weddell Sea Project 1986 (ANT V/2) July 16–September 10, 1986" by Werner Rabe

Heft Nr. 41/1988 – „Zur Verbreitung und Ökologie der Seegurken im Weddellmeer (Antarktis)" von Julian Gutt

Heft Nr. 42/1988 – "The zooplankton community in the deep bathyal and abyssal zones of the eastern North Atlantic" by Werner Beckmann

Heft Nr. 43/1988 – "Scientific cruise report of Arctic Expedition ARK IV/3" Wissenschaftlicher Fahrtbericht der Arktis-Expedition ARK IV/3, compiled by Jörn Thiede

Heft Nr. 44/1988 – "Data Report for FV 'Polarstern' Cruise ARK IV/1, 1987 to the Arctic and Polar Fronts" by Hans-Jürgen Hirche

Heft Nr. 45/1988 – „Zoogeographie und Gemeinschaftsanalyse des Makrozoobenthos des Weddellmeeres (Antarktis)" von Joachim Voß

Heft Nr. 46/1988 – "Meteorological and Oceanographic Data of the Winter-Weddell-Sea Project 1986 (ANT V/3)" by Eberhard Fahrbach

Heft Nr. 47/1988 – „Verteilung und Herkunft glazial-mariner Gerölle am Antarktischen Kontinentalrand des östlichen Weddellmeeres" von Wolfgang Oskierski

Heft Nr. 48/1988 – „Variationen des Erdmagnetfeldes an der GvN-Station" von Arnold Brodscholl

* **Heft Nr. 49/1988** – „Zur Bedeutung der Lipide im antarktischen Zooplankton" von Wilhelm Hagen

Heft Nr. 50/1988 – „Die gezeitenbedingte Dynamik des Ekström-Schelfeises, Antarktis" von Wolfgang Kobarg

Heft Nr. 51/1988 – „Ökomorphologie nototheniider Fische aus dem Weddellmeer, Antarktis" von Werner Ekau

Heft Nr. 52/1988 – „Zusammensetzung der Bodenfauna in der westlichen Fram-Straße" von Dieter Piepenburg

* **Heft Nr. 53/1988** – „Untersuchungen zur Ökologie des Phytoplanktons im südöstlichen Weddellmeer (Antarktis) im Jan./Febr. 1985" von Eva-Maria Nöthig

Heft Nr. 54/1988 – „Die Fischfauna des östlichen und südlichen Weddellmeeres: geographische Verbreitung, Nahrung und trophische Stellung der Fischarten" von Wiebke Schwarzbach

Heft Nr. 55/1988 – "Weight and length data of zooplankton in the Weddell Sea in austral spring 1986 (Ant V/3)" by Elke Mizdalski

Heft Nr. 56/1989 – "Scientific cruise report of Arctic expeditions ARK IV/1, 2 & 3" by G. Krause, J. Meincke und J. Thiede

Heft Nr. 57/1989 – „Die Expedition ANTARKTIS V mit FS ‚Polarstern' 1986/87"
Bericht von den Fahrtabschnitten ANT V/4–5 von H. Miller und H. Oerter

* **Heft Nr. 58/1989** – „Die Expedition ANTARKTIS VI mit FS ‚Polarstern' 1987/88"
von D. K. Fütterer

Heft Nr. 59/1989 – „Die Expedition ARKTIS V/1a, 1b und 2 mit FS ‚Polarstern' 1988"
von M. Spindler

Heft Nr. 60/1989 – „Ein zweidimensionales Modell zur thermohalinen Zirkulation unter dem Schelfeis"
von H. H. Hellmer

Heft Nr. 61/1989 – „Die Vulkanite im westlichen und mittleren Neuschwabenland,
Vestfjella und Ahlmannryggen, Antarktika" von M. Peters

* **Heft-Nr. 62/1989** – "The Expedition ANTARKTIS VII/1 and 2 (EPOS I) of RV 'Polarstern'
in 1988/89", by I. Hempel

Heft Nr. 63/1989 – „Die Eisalgenflora des Weddellmeeres (Antarktis): Artenzusammensetzung und Biomasse
sowie Ökophysiologie ausgewählter Arten" von Annette Bartsch

Heft Nr. 64/1989 – "Meteorological Data of the G.-v.-Neumayer-Station (Antarctica)" by L. Helmes

Heft Nr. 65/1989 – „Expedition Antarktis VII/3 in 1988/89" by I. Hempel, P. H. Schalk, V. Smetacek

Heft Nr. 66/1989 – „Geomorphologisch-glaziologische Detailkartierung
des arid-hochpolaren Borgmassivet, Neuschwabenland, Antarktika" von Karsten Brunk

Heft-Nr. 67/1990 – „Identification key and catalogue of larval Antarctic fishes",
edited by Adolf Kellermann

Heft-Nr. 68/1990 – „The Expediton Antarktis VII/4 (Epos leg 3) and VII/5 of RV 'Polarstern' in 1989",
edited by W. Arntz, W. Ernst, I. Hempel

Heft-Nr. 69/1990 – „Abhängigkeiten elastischer und rheologischer Eigenschaften des Meereises vom
Eisgefüge", von Harald Hellmann

Heft-Nr. 70/1990 – „Die beschalten benthischen Mollusken (Gastropoda und Bivalvia) des
Weddellmeeres, Antarktis", von Stefan Hain

Heft-Nr. 71/1990 – „Sedimentologie und Paläomagnetik an Sedimenten der Maudkuppe (Nordöstliches
Weddellmeer)", von Dieter Cordes.

Heft-Nr. 72/1990 – „Distribution and abundance of planktonic copepods (Crustacea) in the Weddell Sea
in summer 1980/81", by F. Kurbjeweit and S. Ali-Khan

Heft-Nr. 73/1990 – „Zur Frühdiagenese von organischem Kohlenstoff und Opal in Sedimenten des südlichen
und östlichen Weddellmeeres", von M. Schlüter

Heft-Nr. 74/1990 – „Expeditionen ANTARKTIS-VIII/3 und VIII/4 mit FS ‚Polarstern' 1989"
von Rainer Gersonde und Gotthilf Hempel

Heft-Nr. 75/1991 – „Quartäre Sedimentationsprozesse am Kontinentalhang des Süd-Orkey-Plateaus im
nordwestlichen Weddellmeer (Antarktis)", von Sigrun Grünig

Heft-Nr. 76/1990 – „Ergebnisse der faunistischen Arbeiten im Benthal von King George Island
(Südshetlandinseln, Antarktis)", von Martin Rauschert

Heft-Nr. 77/1990 – „Verteilung von Mikroplankton-Organismen nordwestlich der Antarktischen Halbinsel
unter dem Einfluß sich ändernder Umweltbedingungen im Herbst", von Heinz Klöser

Heft-Nr. 78/1991 – „Hochauflösende Magnetostratigraphie spätquartärer Sedimente arktischer
Meeresgebiete", von Norbert R. Nowaczyk

Heft-Nr. 79/1991 – „Ökophysiologische Untersuchungen zur Salinitäts- und Temperaturtoleranz
antarktischer Grünalgen unter besonderer Berücksichtigung des ß-Dimethylsulfoniumpropionat
(DMSP) - Stoffwechsels", von Ulf Karsten

Heft-Nr. 80/1991 – „Die Expedition ARKTIS VII/1 mit FS ‚Polarstern' 1990",
herausgegeben von Jörn Thiede und Gotthilf Hempel

Heft-Nr. 81/1991 – „Paläoglaziologie und Paläozeanographie im Spätquartär am Kontinentalrand des
südlichen Weddellmeeres, Antarktis", von Martin Melles

Heft-Nr. 82/1991 – „Quantifizierung von Meereseigenschaften: Automatische Bildanalyse von
Dünnschnitten und Parametrisierung von Chlorophyll- und Salzgehaltsverteilungen", von Hajo Eicken

Heft-Nr. 83/1991 – „Das Fließen von Schelfeisen - numerische Simulationen
mit der Methode der finiten Differenzen", von Jürgen Determann

Heft-Nr. 84/1991 – „Die Expedition ANTARKTIS-VIII/1-2, 1989 mit der Winter Weddell Gyre Study
der Forschungsschiffe „Polarstern" und „Akademik Fedorov", von Ernst Augstein,
Nikolai Bagriantsev und Hans Werner Schenke

Heft-Nr. 85/1991 – „Zur Entstehung von Unterwassereis und das Wachstum und die Energiebilanz
des Meereises in der Atka Bucht, Antarktis", von Josef Kipfstuhl

Heft-Nr. 86/1991 – „Die Expedition ANTARKTIS-VIII mit „FS Polarstern" 1989/90. Bericht vom
Fahrtabschnitt ANT-VIII / 5", von Heinz Miller und Hans Oerter

Heft-Nr. 87/1991 – "Scientific cruise reports of Arctic expeditions ARK VI / 1-4 of RV "Polarstern"
in 1989", edited by G. Krause, J. Meincke & H. J. Schwarz

Heft-Nr. 88/1991 – „Zur Lebensgeschichte dominanter Copepodenarten (*Calanus finmarchicus,
C. glacialis, C. hyperboreus, Metridia longa)* in der Framstraße", von Sabine Diel

Heft-Nr. 89/1991 – „Detaillierte seismische Untersuchungen am östlichen Kontinentalrand des Weddell-Meeres vor Kapp Norvegia, Antarktis“, von Norbert E. Kaul

Heft-Nr. 90/1991 – „Die Expedition ANTARKTIS-VIII mit FS „Polarstern“ 1989/90. Bericht von den Fahrtabschnitten ANT-VIII/6-7“, herausgegeben von Dieter Karl Fütterer und Otto Schrems

Heft-Nr. 91/1991 – “Blood physiology and ecological consequences in Weddell Sea fishes (Antarctica)“, by Andreas Kunzmann

Heft-Nr. 92/1991 – „Zur sommerlichen Verteilung des Mesozooplanktons im Nansen-Becken, Nordpolarmeer“, von Nicolai Mumm

Heft-Nr. 93/1991 – „Die Expedition ARKTIS VII mit FS „Polarstern“, 1990. Bericht vom Fahrtabschnitt ARK VII/2“, herausgegeben von Gunther Krause

Heft-Nr. 94/1991 – „Die Entwicklung des Phytoplanktons im östlichen Weddellmeer (Antarktis) beim Übergang vom Spätwinter zum Frühjahr“, von Renate Scharek

Heft-Nr. 95/1991 – „Radioisotopenstratigraphie, Sedimentologie und Geochemie jungquartärer Sedimente des östlichen Arktischen Ozeans“, von Horst Bohrmann

Heft-Nr. 96/1991 – „Holozäne Sedimentationsentwicklung im Scoresby Sund, Ost-Grönland“, von Peter Marienfeld

Heft-Nr. 97/1991 – „Strukturelle Entwicklung und Abkühlungsgeschichte der Heimefrontfjella (Westliches Dronning Maud Land/Antarktika)“, von Joachim Jacobs

Heft-Nr. 98/1991 – „Zur Besiedlungsgeschichte des antarktischen Schelfes am Beispiel der Isopoda (Crustacea, Malacostraca)“, von Angelika Brandt

Heft-Nr. 99/1992 – “The Antarctic ice sheet and environmental change: a three-dimensional modelling study“, by Philippe Huybrechts

* **Heft-Nr. 100/1992** – „Die Expeditionen ANTARKTIS IX/1-4 des Forschungsschiffes „Polarstern“ 1990/91“, herausgegeben von Ulrich Bathmann, Meinhard Schulz-Baldes, Eberhard Fahrbach, Victor Smetacek und Hans-Wolfgang Hubberten

Heft-Nr. 101/1992 – „Wechselbeziehungen zwischen Schwermetallkonzentrationen (Cd, Cu, Pb, Zn) im Meewasser und in Zooplanktonorganismen (Copepoda) der Arktis und des Atlantiks“, von Christa Pohl

Heft-Nr. 102/1992 – „Physiologie und Ultrastruktur der antarktischen Grünalge *Prasiola crispa* ssp. *antarctica* unter osmotischem Streß und Austrocknung“, von Andreas Jacob

Heft-Nr. 103/1992 – „Zur Ökologie der Fische im Weddelmeer“, von Gerd Hubold

Heft-Nr. 104/1992 – „Mehrkanalige adaptive Filter für die Unterdrückung von multiplen Reflexionen in Verbindung mit der freien Oberfläche in marinen Seismogrammen“, von Andreas Rosenberger

Heft-Nr. 105/1992 – „Radiation and Eddy Flux Experiment 1991 *(REFLEX I)*“, von Jörg Hartmann, Christoph Kottmeier und Christian Wamser

Heft-Nr. 106/1992 – „Ostracoden im Epipelagial vor der Antarktischen Halbinsel - ein Beitrag zur Systematik sowie zur Verbreitung und Populationsstruktur unter Berücksichtigung der Saisonalität“, von Rüdiger Kock

Heft-Nr. 107/1992 – „ARCTIC ‘91: Die Expedition ARK-VIII/3 mit FS „Polarstern“ 1991“, von Dieter K. Fütterer

Heft-Nr. 108/1992 – „Dehnungsbeben an einer Störungszone im Ekström-Schelfeis nördlich der Georg-von-Neumayer Station, Antarktis. – Eine Untersuchung mit seismologischen und geodätischen Methoden”, von Uwe Nixdorf.

Heft-Nr. 109/1992 – „Spätquartäre Sedimentation am Kontinentalrand des südöstlichen Weddellmeeres, Antarktis”, von Michael Weber.

Heft-Nr. 110/1992 – „Sedimentfazies und Bodenwasserstrom am Kontinentalhang des nordwestlichen Weddellmeeres”, von Isa Brehme.

Heft-Nr. 111/1992 – „Die Lebensbedingungen in den Solekanälchen des antarktischen Meereises”, von Jürgen Weissenberger.

Heft-Nr. 112/1992 – „Zur Taxonomie von rezenten benthischen Foraminiferen aus dem Nansen Becken, Arktischer Ozean“, von Jutta Wollenburg.

Heft-Nr. 113/1992 – „Die Expedition ARKTIS VIII/1 mit FS "Polarstern“ 1991“, herausgegeben von Gerhard Kattner.

* **Heft-Nr. 114/1992** – „Die Gründungsphase deutscher Polarforschung, 1865-1875“, von Reinhard A. Krause.

Heft-Nr. 115/1992 – „Scientific Cruise Report of the 1991 Arctic Expedition ARK VIII/2 of RV "Polarstern" (EPOS II)", by Eike Rachor.

Heft-Nr. 116/1992 – „The Meteorological Data of the Georg-von-Neumayer-Station (Antarctica) for 1988, 1989, 1990 and 1991", by Gert König-Langlo.

Heft-Nr. 117/1992 – „Petrogenese des metamorphen Grundgebirges der zentralen Heimefrontfjella (westliches Dronning Maud Land / Antarktis)", von Peter Schulze.

Heft-Nr. 118/1993 – „Die mafischen Gänge der Shackleton Range / Antarktika: Petrographie, Geochemie, Isotopengeochemie und Paläomagnetik", von Rüdiger Hotten.

* **Heft-Nr. 119/1993** – „Gefrierschutz bei Fischen der Polarmeere”, von Andreas P.A. Wöhrmann.

* **Heft-Nr. 120/1993** – „East Siberian Arctic Region Expedition '92: The Laptev Sea - its Significance for Arctic Sea-Ice Formation and Transpolar Sediment Flux", by D. Dethleff, D. Nürnberg, E. Reimnitz, M. Saarso and Y. P. Sacchenko. – „Expedition to Novaja Zemlja and Franz Josef Land with RV.'Dalnie Zelentsy'", by D. Nürnberg and E. Groth.

* **Heft-Nr. 121/1993** – „Die Expedition ANTARKTIS X/3 mit FS 'Polarstern' 1992", herausgegeben von Michael Spindler, Gerhard Dieckmann und David Thomas.

Heft-Nr. 122/1993 – „Die Beschreibung der Korngestalt mit Hilfe der Fourier-Analyse: Parametrisierung der morphologischen Eigenschaften von Sedimentpartikeln", von Michael Diepenbroek.

* **Heft-Nr. 123/1993** – „Zerstörungsfreie hochauflösende Dichteuntersuchungen mariner Sedimente", von Sebastian Gerland.

Heft-Nr. 124/1993 – „Umsatz und Verteilung von Lipiden in arktischen marinen Organismen unter besonderer Berücksichtigung unterer trophischer Stufen", von Martin Graeve.

Heft-Nr. 125/1993 – „Ökologie und Respiration ausgewählter arktischer Bodenfischarten", von Christian F. von Dorrien.

Heft-Nr. 126/1993 – „Quantitative Bestimmung von Paläoumweltparametern des Antarktischen Oberflächenwassers im Spätquartär anhand von Transferfunktionen mit Diatomeen", von Ulrich Zielinski

Heft-Nr. 127/1993 – „Sedimenttransport durch das arktische Meereis: Die rezente lithogene und biogene Materialfracht", von Ingo Wollenburg.

Heft-Nr. 128/1993 – „Cruise ANTARKTIS X/3 of RV 'Polarstern': CTD-Report", von Marek Zwierz.

Heft-Nr. 129/1993 – „Reproduktion und Lebenszyklen dominanter Copepodenarten aus dem Weddellmeer, Antarktis", von Frank Kurbjeweit

Heft-Nr. 130/1993 – „Untersuchungen zu Temperaturregime und Massenhaushalt des Filchner-Ronne-Schelfeises, Antarktis, unter besonderer Berücksichtigung von Anfrier- und Abschmelzprozessen", von Klaus Grosfeld

Heft-Nr. 131/1993 – „Die Expedition ANTARKTIS X/5 mit FS 'Polarstern' 1992", herausgegeben von Rainer Gersonde

Heft-Nr. 132/1993 – „Bildung und Abgabe kurzkettiger halogenierter Kohlenwasserstoffe durch Makroalgen der Polarregionen", von Frank Laturnus

Heft-Nr. 133/1994 – "Radiation and Eddy Flux Experiment 1993 *(REFLEX II)*", by Christoph Kottmeier, Jörg Hartmann, Christian Wamser, Axel Bochert, Christof Lüpkes, Dietmar Freese and Wolfgang Cohrs

* **Heft-Nr. 134/1994** – "The Expedition ARKTIS-IX/1", edited by Hajo Eicken and Jens Meincke

Heft-Nr. 135/1994 – „Die Expeditionen ANTARKTIS X/6-8", herausgegeben von Ulrich Bathmann, Victor Smetacek, Hein de Baar, Eberhard Fahrbach und Gunter Krause

Heft-Nr. 136/1994 – „Untersuchungen zur Ernährungsökologie von Kaiserpinguinen *(Aptenodytes forsteri)* und Königspinguinen *(Aptenodytes patagonicus)*", von Klemens Pütz

* **Heft-Nr. 137/1994** – „Die känozoische Vereisungsgeschichte der Antarktis", von Werner U. Ehrmann

Heft-Nr. 138/1994 – „Untersuchungen stratosphärischer Aerosole vulkanischen Ursprungs und polarer stratosphärischer Wolken mit einem Mehrwellenlängen-Lidar auf Spitzbergen *(79° N, 12° E)*", von Georg Beyerle

Heft-Nr. 139/1994 – „Charakterisierung der Isopodenfauna (Crustacea, Malacostraca) des Scotia-Bogens aus biogeographischer Sicht: Ein multivariater Ansatz", von Holger Winkler.

Heft-Nr. 140/1994 – „Die Expedition ANTARKTIS X/4 mit FS 'Polarstern' 1992", herausgegeben von Peter Lemke

Heft-Nr. 141/1994 – „Satellitenaltimetrie über Eis – Anwendung des GEOSAT-Altimeters über dem Ekströmisen, Antarktis", von Clemens Heidland

Heft-Nr. 142/1994 – "The 1993 Northeast Water Expedition. Scientific cruise report of RV'Polarstern' Arctic cruises ARK IX/2 and 3, USCG 'Polar Bear' cruise NEWP and the NEWLand expedition", edited by Hans-Jürgen Hirche and Gerhard Kattner

Heft-Nr. 143/1994 – „Detaillierte refraktionsseismische Untersuchungen im inneren Scoresby Sund Ost-Grönland", von Notker Fechner

Heft-Nr. 144/1994 – „Russian-German Cooperation in the Siberian Shelf Seas: Geo-System Laptev Sea", edited by Heidemarie Kassens, Hans-Wolfgang Hubberten, Sergey M. Pryamikov und Rüdiger Stein

* **Heft-Nr. 145/1994** – „The 1993 Northeast Water Expedition. Data Report of RV 'Polarstern' Arctic Cruises IX/2 and 3", edited by Gerhard Kattner and Hans-Jürgen Hirche.

Heft-Nr. 146/1994 – "Radiation Measurements at the German Antarctic Station Neumayer 1982-1992", by Torsten Schmidt and Gert König-Langlo.

Heft-Nr. 147/1994 – „Krustenstrukturen und Verlauf des Kontinentalrandes im Weddell Meer / Antarktis", von Christian Hübscher.

Heft-Nr. 148/1994 – "The expeditions NORILSK/TAYMYR 1993 and BUNGER OASIS 1993/94 of the AWI Research Unit Potsdam", edited by Martin Melles.

** **Heft-Nr. 149/1994** – "Die Expedition ARCTIC' 93. Der Fahrtabschnitt ARK-IX/4 mit FS 'Polarstern' 1993", herausgegeben von Dieter K. Fütterer.

Heft-Nr. 150/1994 – "Der Energiebedarf der Pygoscelis-Pinguine: eine Synopse", von Boris M. Culik.

Heft-Nr. 151/1994 – „Russian-German Cooperation: The Transdrift I Expedition to the Laptev Sea", edited by Heidemarie Kassens and Valeriy Y. Karpiy.

Heft-Nr. 152/1994 – „Die Expedition ANTARKTIS-X mit FS 'Polarstern' 1992. Bericht von den Fahrtabschnitten / ANT-X / 1a und 2", herausgegeben von Heinz Miller.

Heft-Nr. 153/1994 – "Aminosäuren und Huminstoffe im Stickstoffkreislauf polarer Meere", von Ulrike Hubberten.

Heft-Nr. 154/1994 – "Regional und seasonal variability in the vertical distribution of mesozooplankton in the Greenland Sea", by Claudio Richter.

Heft-Nr. 155/1995 – "Benthos in polaren Gewässern", herausgegeben von Christian Wiencke und Wolf Arntz.

Heft-Nr. 156/1995 – "An adjoint model for the determination of the mean oceanic circulation, air-sea fluxes und mixing coefficients", by Reiner Schlitzer.

Heft-Nr. 157/1995 – "Biochemische Untersuchungen zum Lipidstoffwechsel antarktischer Copepoden", von Kirsten Fahl.

** **Heft-Nr. 158/1995** – "Die Deutsche Polarforschung seit der Jahrhundertwende und der Einfluß Erich von Drygalskis", von Cornelia Lüdecke.

Heft-Nr. 159/1995 – The distribution of $\partial^{18}O$ in the Arctic Ocean: Implications for the freshwater balance of the halocline and the sources of deep and bottom waters", by Dorothea Bauch.

* **Heft-Nr. 160/1995** – "Rekonstruktion der spätquartären Tiefenwasserzirkulation und Produktivität im östlichen Südatlantik anhand von benthischen Foraminiferenvergesellschaftungen", von Gerhard Schmiedl.

Heft-Nr. 161/1995 – "Der Einfluß von Salinität und Lichtintensität auf die Osmolytkonzentrationen, die Zellvolumina und die Wachstumsraten der antarktischen Eisdiatomeen *Chaetoceros* sp. und *Navicula* sp. unter besonderer Berücksichtigung der Aminosäure Prolin", von Jürgen Nothnagel.

Heft-Nr. 162/1995 – "Meereistransportiertes lithogenes Feinmaterial in spätquartären Tiefseesedimenten des zentralen östlichen Arktischen Ozeans und der Framstraße", von Thomas Letzig.

Heft-Nr. 163/1995 – "Die Expedition ANTARKTIS-XI/2 mit FS "Polarstern" 1993/94", herausgegeben von Rainer Gersonde.

Heft-Nr. 164/1995 – "Regionale und altersabhängige Variation gesteinsmagnetischer Parameter in marinen Sedimenten der Arktis", von Thomas Frederichs.

Heft-Nr. 165/1995 – "Vorkommen, Verteilung und Umsatz biogener organischer Spurenstoffe: Sterole in antarktischen Gewässern", von Georg Hanke.

Heft-Nr. 166/1995 – "Vergleichende Untersuchungen eines optimierten dynamisch-thermodynamischen Meereismodell mit Beobachtungen im Weddellmeer", von Holger Fischer.

Heft-Nr. 167/1995 – "Rekonstruktionen von Paläo-Umweltparametern anhand von stabilen Isotopen und Faunen-Vergesellschaftungen planktischer Foraminiferen im Südatlantik", von Hans-Stefan Niebler

Heft-Nr. 168/1995 – "Die Expedition ANTARKTIS XII mit FS 'Polarstern' 1993/94. Bericht von den Fahrtabschnitten ANT XII/1 und 2", herausgegeben von Gerhard Kattner und Dieter Karl Fütterer.

Heft-Nr. 169/1995 – "Medizinische Untersuchung zur Circadianrhythmik und zum Verhalten bei Überwinterern auf einer antarktischen Forschungsstation", von Hans Wortmann.

Heft-Nr. 170/1995 – DFG-Kolloquium: Terrestrische Geowissenschaften - Geologie und Geophysik der Antarktis.

Heft-Nr. 171/1995 – "Strukturentwicklung und Petrogenese des metamorphen Grundgebirges der nördlichen Heimefrontfjella (westliches Dronning Maud Land/Antarktika)", von Wilfried Bauer.

Heft-Nr. 172/1995 – "Die Struktur der Erdkruste im Bereich des Scoresby Sund, Ostgrönland: Ergebnisse refraktionsseismischer und gravimetrischer Untersuchungen", von Holger Mandler.

Heft-Nr. 173/1995 – "Paläozoische Akkretion am paläopazifischen Kontinentalrand der Antarktis in Nordvictorialand – P-T-D-Geschichte und Deformationsmechanismen im Bowers Terrane", von Stefan Matzer.

Heft-Nr. 174/1995 – "The Expedition ARKTIS-X/2 of RV 'Polarstern' in 1994", edited by Hans-W. Hubberten.

Heft-Nr. 175/1995 – "Russian-German Cooperation: The Expedition TAYMYR 1994", edited by Christine Siegert and Dmitry Bolshiyanov.

Heft-Nr. 176/1995 – "Russian-German Cooperation: Laptev Sea System", edited by Heidemarie Kassens, Dieter Piepenburg, Jörn Thiede, Leonid Timokhov, Hans-Wolfgang Hubberten and Sergey M. Priamikov.

Heft-Nr. 177/1995 – "Organischer Kohlenstoff in spätquartären Sedimenten des Arktischen Ozeans: Terrigener Eintrag und marine Produktivität", von Carsten J. Schubert.

Heft-Nr. 178/1995 – "Cruise ANTARKTIS XII/4 of RV 'Polarstern' in 1995: CTD-Report", by Jüri Sildam.

Heft-Nr. 179/1995 – "Benthische Foraminiferenfaunen als Wassermassen-, Produktions- und Eisdriftanzeiger im Arktischen Ozean", von Jutta Wollenburg.

Heft-Nr. 180/1995 – "Biogenopal und biogenes Barium als Indikatoren für spätquartäre Produktivitätsänderungen am antarktischen Kontinentalhang, atlantischer Sektor", von Wolfgang J. Bonn.

Heft-Nr. 181/1995 – "Die Expedition ARKTIS X/1 des Forschungsschiffes ‚Polarstern' 1994", herausgegeben von Eberhard Fahrbach.

Heft-Nr. 182/1995 – "Laptev Sea System: Expeditions in 1994", edited by Heidemarie Kassens.

Heft-Nr. 183/1996 – "Interpretation digitaler Parasound Echolotaufzeichnungen im östlichen Arktischen Ozean auf der Grundlage physikalischer Sedimenteigenschaften", von Uwe Bergmann.

Heft-Nr. 184/1996 – "Distribution and dynamics of inorganic nitrogen compounds in the troposphere of continental, coastal, marine and Arctic areas", by María Dolores Andrés Hernández.

Heft-Nr. 185/1996 – "Verbreitung und Lebensweise der Aphroditiden und Polynoiden (Polychaeta) im östlichen Wedde meer und im Lazarevmeer (Antarktis)", von Michael Stiller.

Heft-Nr. 186/1996 – "Reconstruction of Late Quaternary environmental conditions applying the natural radionuclides ^{230}Th, ^{10}Be, ^{231}Pa and ^{238}U: A study of deep-sea sediments from the eastern sector of the Antrctic Circumpolar Current System", by Martin Frank.

Heft-Nr. 187/1996 – "The Meteorological Data of the Neumayer Station (Antarctica) for 1992, 1993 and 1994", by Gert König-Langlo and Andreas Herber.

Heft-Nr. 188/1996 – "Die Expedition ANTARKTIS-XI/3 mit FS 'Polarstern' 1994", herausgegeben von Heinz Miller und Hannes Grobe.

Heft-Nr. 189/1996 – "Die Expedition ARKTIS-VII/3 mit FS 'Polarstern' 1990", herausgegeben von Heinz Miller und Hannes Grobe.

Heft-Nr. 190/1996 – “Cruise report of the Joint Chilean-German-Italian Magellan 'Victor Hensen' Campaign in 1994”, edited by Wolf Arntz and Matthias Gorny.

Heft-Nr. 191/1996 – “Leitfähigkeits- und Dichtemessung an Eisbohrkernen”, von Frank Wilhelms.

Heft-Nr. 192/1996 – “Photosynthese-Charakteristika und Lebensstrategie antarktischer Makroalgen”, von Gabriele Weykam.

Heft-Nr. 193/1996 – “Heterogene Raktionen von N_2O_5 und HBr und ihr Einfluß auf den Ozonabbau in der polaren Stratosphäre”, von Sabine Seisel.

Heft-Nr. 194/1996 – “Ökologie und Populationsdynamik antarktischer Ophiuroiden (Echinodermata)”, von Corinna Dahm.

Heft-Nr. 195/1996 – “Die planktische Foraminifere *Neogloboquadrina pachyderma* (Ehrenberg) im Weddellmeer, Antarktis”, von Doris Berberich.

Heft-Nr. 196/1996 – “Untersuchungen zum Beitrag chemischer und dynamischer Prozesse zur Variabilität des stratosphärischen Ozons über der Arktis”, von Birgit Heese.

Heft-Nr. 197/1996 – “The Expedition ARKTIS-XI/2 of 'Polarstern' in 1995”, edited by Gunther Krause.

Heft-Nr. 198/1996 – “Geodynamik des Westantarktischen Riftsystems basierend auf Apatit-Spaltspuranalysen“, von Frank Lisker.

Heft-Nr. 199/1996 – “The 1993 Northeast Water Expedition. Data Report on CTD Measurements of RV 'Polarstern' Cruises ARKTIS IX/2 and 3“, by Gereon Budéus and Wolfgang Schneider.

Heft-Nr. 200/1996 – “Stability of the Thermohaline Circulation in analytical and numerical models“, by Gerrit Lohmann.

Heft-Nr. 201/1996 – “Trophische Beziehungen zwischen Makroalgen und Herbivoren in der Potter Cove (King George-Insel, Antarktis)“, von Katrin Iken.

Heft-Nr. 202/1996 – “Zur Verbreitung und Respiration ökologisch wichtiger Bodentiere in den Gewässern um Svalbard (Arktis)“, von Michael K. Schmid.

Heft-Nr. 203/1996 – “Dynamik, Rauhigkeit und Alter des Meereises in der Arktis - Numerische Untersuchungen mit einem großskaligen Modell“, von Markus Harder.

Heft-Nr. 204/1996 – “Zur Parametrisierung der stabilen atmosphärischen Grenzschicht über einem antarktischen Schelfeis“, von Dörthe Handorf.

Heft-Nr. 205/1996 – “Textures and fabrics in the GRIP ice core, in relation to climate history and ice deformation“, by Thorsteinn Thorsteinsson.

Heft-Nr. 206/1996 – “Der Ozean als Teil des gekoppelten Klimasystems: Versuch der Rekonstruktion der glazialen Zirkulation mit verschieden komplexen Atmosphärenkomponenten“, von Kerstin Fieg.

Heft-Nr. 207/1996 – “Lebensstrategien dominanter antarktischer Oithonidae (Cyclopoida, Copepoda) und Oncaeidae (Poecilostomatoida, Copepoda) im Bellingshausenmeer“, von Cornelia Metz.

Heft-Nr. 208/1996 – “Atmosphäreneinfluß bei der Fernerkundung von Meereis mit passiven Mikrowellenradiometern“, von Christoph Oelke.

Heft-Nr. 209/1996 – “Klassifikation von Radarsatellitendaten zur Meereiserkennung mit Hilfe von Line-Scanner-Messungen“, von Axel Bochert.

Heft-Nr. 210/1996 – “Die mit ausgewählten Schwämmen (Hexactinellida und Demospongiae) aus dem Weddellmeer, Antarktis, vergesellschaftete Fauna“, von Kathrin Kunzmann.

Heft-Nr. 211/1996 – “Russian-German Cooperation: The Expediton TAYMYR 1995 and the Expedition KOLYMA 1995“, by Dima Yu. Bolshiyanov and Hans-W. Hubberten.

Heft-Nr. 212/1996 – “Surface-sediment composition and sedimentary processes in the central Arctic Ocean and along the Eurasian Continental Margin“, by Ruediger Stein, Gennadij I. Ivanov, Michael A. Levitan, and Kirsten Fahl.

Heft-Nr. 213/1996 – “Gonadenentwicklung und Eiproduktion dreier *Calanus*-Arten (Copepoda): Freilandbeobachtungen, Histologie und Experimente“, von Barbara Niehoff.

Heft-Nr. 214/1996 – “Numerische Modellierung der Übergangszone zwischen Eisschild und Eisschelf“, von Christoph Mayer.

Heft-Nr. 215/1996 – “Arbeiten der AWI-Forschungsstelle Potsdam in Antarktika, 1994/95“, herausgegeben von Ulrich Wand.

Heft-Nr. 216/1996 – “Rekonstruktion quartärer Klimaänderungen im atlantischen Sektor des Südpolarmeeres anhand von Radiolarien“, von Uta Brathauer.

Heft-Nr. 217/1996 – “Adaptive Semi-Lagrange-Finite-Elemente-Methode zur Lösung der Flachwassergleichungen: Implementierung und Parallelisierung“, von Jörn Behrens.

Heft-Nr. 218/1997 – “Radiation and Eddy Flux Experiment 1995 (REFLEX III)“, by Jörg Hartmann, Axel Bochert, Dietmar Freese, Christoph Kottmeier, Dagmar Nagel and Andreas Reuter.

Heft-Nr. 219/1997 – “Die Expedition ANTARKTIS-XII mit FS 'Polarstern' 1995. Bericht vom Fahrtabschnitt ANT-XII/3“, herausgegeben von Wilfried Jokat und Hans Oerter.

Heft-Nr. 220/1997 – “Ein Beitrag zum Schwerefeld im Bereich des Weddellmeeres, Antarktis. Nutzung von Altimetermessungen des GEOSAT und ERS-1”, von Tilo Schöne.

Heft-Nr. 221/1997 – “Die Expeditionen ANTARKTIS-XIII/1-2 des Forschungsschiffes 'Polarstern' 1995/96“, herausgegeben von Ulrich Bathmann, Mike Lucas und Victor Smetacek.

Heft-Nr. 222/1997 – “Tectonic Structures and Glaciomarine Sedimentation in the South-Eastern Weddell Sea from Seismic Reflection Data”, by László Oszkó.

Heft-Nr. 223/1997 – "Bestimmung der Meereisdicke mit seismischen und elektromagnetisch-induktiven Verfahren", von Christian Haas.

Heft-Nr. 224/1997 – "Troposphärische Ozonvariationen in Polarregionen", von Silke Wessel.

Heft-Nr. 225/1997 – "Biologische und ökologische Untersuchungen zur kryopelagischen Amphipodenfauna des arktischen Meereises", von Michael Poltermann.

Heft-Nr. 226/1997 – "Scientific Cruise Report of the Arctic Expedition ARK-XI/1 of RV 'Polarstern' in 1995", edited by Eike Rachor.

Heft-Nr. 227/1997 – "Der Einfluß kompatibler Substanzen und Kyroprotektoren auf die Enzyme Malatdehydrogenase (MDH) und Glucose-6-phosphat-Dehydrogenase (G6P-DH) aus Acrosiphonia arcta (Chlorophyta) der Arktis", von Katharina Kück.

Heft-Nr. 228/1997 – "Die Verbreitung epibenthischer Mollusken im chilenischen Beagle-Kanal", von Katrin Linse.

Heft-Nr. 229/1997 – "Das Mesozooplankton im Laptevmeer und östlichen Nansen-Becken - Verteilung und Gemeinschaftsstrukturen im Spätsommer", von Hinrich Hanssen.

Heft-Nr. 230/1997 – "Modell eines adaptierbaren, rechnergestützten, wissenschaftlichen Arbeitsplatzes am Alfred-Wegener-Institut für Polar- und Meeresforschung", von Lutz-Peter Kurdelski.

Heft-Nr. 231/1997 – "Zur Ökologie arktischer und antarktischer Fische: Aktivität, Sinnesleistungen und Verhalten", von Christopher Zimmermann.

Heft-Nr. 232/1997 – "Persistente clororganische Verbindungen in hochantarktischen Fischen", von Stephan Zimmermann.

Heft-Nr. 233/1997 – "Zur Ökologie des Dimethylsulfoniumpropionat (DMSP)-Gehaltes temperierter und polarer Phytoplanktongemeinschaften im Vergleich mit Laborkulturen der Coccolithophoride *Emiliania huxleyi* und derantarktischen Diatomee *Nitzschia lecointei"*, von Doris Meyerdierks.

Heft-Nr. 234/1997 – "Die Expedition ARCTIC '96 des FS 'Polarstern' (ARK XII) mit der Arctic Climate System Study (ACSYS)", von Ernst Augstein und den Fahrtteilnehmern.

Heft-Nr. 235/1997 – "Polonium-210 und Blei-219 im Südpolarmeer: Natürliche Tracer für biologische und hydrographische Prozesse im Oberflächenwasser des Antarktischen Zirkumpolarstroms und des Weddellmeeres", von Jana Friedrich.

Heft-Nr. 236/1997 – "Determination of atmospheric trace gas amounts and corresponding natural isotopic rations by means of ground-based FTIR spectroscopy in the high Arctic", by Arndt Meier.

Heft-Nr. 237/1997 – "Russian-German Cooperation: The Expedition TAYMYR / SEVERNAYA ZEMLYA 1996", edited by Martin Melles, Birgit Hagedorn and Dmitri Yu. Bolshiyanow.

Heft-Nr. 238/1997 – "Life strategy and ecophysiology of Antarctic macroalgae", by Iván M. Gómez.

Heft-Nr. 239/1997 – "Die Expedition ANTARKTIS XIII/4-5 des Forschungsschiffes 'Polarstern' 1996", herausgegeben von Eberhard Fahrbach und Dieter Gerdes.

Heft-Nr. 240/1997 – "Untersuchungen zur Chrom-Speziation im Meerwasser, Meereis und Schnee aus ausgewählten Gebieten der Arktis", von Heide Giese.

Heft-Nr. 241/1997 – "Late Quaternary glacial history and paleoceanographic reconstructions along the East Greenlar continental margin: Evidence from high-resolution records of stable isotopes and ice-rafted debris", by Seung-Il Nam

Heft-Nr. 242/1997 – "Thermal, hydrological and geochemical dynamics of the active layer at a continuous site, Taym Peninsula, Siberia", by Julia Boike.

Heft-Nr. 243/1997 – "Zur Paläoozeanographie hoher Breiten: Stellvertreterdaten aus Foraminiferen", von Andreas Mackensen.

Heft-Nr. 244/1997 – "The Geophysical Observatory at Neumayer Station, Antarctica. Geomagnetic and seismologica observations in 1995 and 1996", by Alfons Eckstaller, Thomas Schmidt, Viola Gaw, Christian Müller and Johannes Rogenhagen.

Heft-Nr. 245/1997 – "Temperaturbedarf und Biogeographie mariner Makroalgen - Anpassung mariner Makroalgen an tiefe Temperaturen", von Bettina Bischoff-Bäsmann.

Heft-Nr. 246/1997 – "Ökologische Untersuchungen zur Fauna des arktischen Meereises", von Christine Friedrich.

Heft-Nr. 247/1997 – "Entstehung und Modifizierung von marinen gelösten organischen Substanzen", von Berit Kirchh

Heft-Nr. 248/1997 – "Laptev Sea System: Expeditions in 1995", edited by Heidemarie Kassens.

Heft-Nr. 249/1997 – "The Expedition ANTARKTIS XIII/3 (EASIZ I) of RV 'Polarstern' to the eastern Weddell Sea in 19 edited by Wolf Arntz and Julian Gutt.

Heft-Nr. 250/1997 – "Vergleichende Untersuchungen zur Ökologie und Biodiversität des Mega-Epibenthos der Arktis und Antarktis", von Andreas Starmans.

Heft-Nr. 251/1997 – "Zeitliche und räumliche Verteilung von Mineralvergesellschaftungen in spätquartären Sediment des Arktischen Ozeans und ihre Nützlichkeit als Klimaindikatoren während der Glazial/Interglazial-Wechsel", von Christoph Vogt.

Heft-Nr. 252/1997 – "Solitäre Ascidien in der Potter Cove (King George Island, Antarktis). Ihre ökologische Bedeutun und Populationsdynamik", von Stephan Kühne.

Heft-Nr. 253/1997 – "Distribution and role of microprotozoa in the Southern Ocean", by Christine Klaas.

Heft-Nr. 254/1997 – "Die spätquartäre Klima- und Umweltgeschichte der Bunger-Oase, Ostantarktis", von Thomas Kulbe.

Heft-Nr. 255/1997 – "Scientific Cruise Report of the Arctic Expedition ARK-XIII/2 of RV 'Polarstern' in 1997", edited by Ruediger Stein and Kirsten Fahl.

Heft-Nr. 256/1998 – "Das Radionuklid Tritium im Ozean: Meßverfahren und Verteilung von Tritium im Südatlantik und im Weddellmeer", von Jürgen Sültenfuß.

Heft-Nr. 257/1998 – "Untersuchungen der Saisonalität von atmosphärischen Dimethylsulfid in der Arktis und Antarktis", von Christoph Kleefeld.

Heft-Nr. 258/1998 – "Bellinghausen- und Amundsenmeer: Entwicklung eines Sedimentationsmodells", von Frank-Oliver Nitsche.

Heft-Nr. 259/1998 – "The Expedition ANTARKTIS-XIV/4 of RV 'Polarstern' in 1997", by Dieter K. Fütterer.

Heft-Nr. 260/1998 – "Die Diatomeen der Laptevsee (Arktischer Ozean): Taxonomie und biogeographische Verbreitung", von Holger Cremer.

Heft-Nr. 261/1998 – "Die Krustenstruktur und Sedimentdecke des Eurasischen Beckens, Arktischer Ozean: Resultate aus seismischen und gravimetrischen Untersuchungen", von Estella Weigelt.

Heft-Nr. 262/1998 – "The Expedition ARKTIS-XIII/3 of RV 'Polarstern' in 1997", by Gunther Krause.

Heft-Nr. 263/1998 – "Thermo-tektonische Entwicklung von Oates Land und der Shackleton Range (Antarktis) basierenc auf Spaltspuranalysen", von Thorsten Schäfer.

Heft-Nr. 264/1998 – "Messungen der stratosphärischen Spurengase ClO, HCl, O_3, N_2O, H_2O und OH mittels flugzeugge tragener Submillimeterwellen-Radiometrie", von Joachim Urban.

Heft-Nr. 265/1998 – "Untersuchungen zu Massenhaushalt und Dynamik des Ronne Ice Shelfs, Antarktis", von Astrid Lambrecht.

Heft-Nr. 266/1998 – "Scientific Cruise Report of the Kara Sea Expedition of RV 'Akademik Boris Petrov' in 1997", edited by Jens Matthiessen and Oleg Stepanets.

Heft-Nr. 267/1998 – "Die Expedition ANTARKTIS-XIV mit FS 'Polarstern' 1997. Bericht vom Fahrtabschnitt ANT-XIV/3", herausgegeben von Wilfried Jokat und Hans Oerter.

Heft-Nr. 268/1998 – "Numerische Modellierung der Wechselwirkung zwischen Atmosphäre und Meereis in der arktischen Eisrandzone", von Gerit Birnbaum.

Heft-Nr. 269/1998 – "Katabatic wind and Boundary Layer Front Experiment around Greenland (KABEG '97)", by Günther Heinemann.

Heft-Nr. 270/1998 – "Architecture and evolution of the continental crust of East Greenland from integrated geophysical studies", by Vera Schlindwein.

Heft-Nr. 271/1998 – "Winter Expedition to the Southwestern Kara Sea - Investigations on Formation and Transport of Turbid Sea-Ice", by Dirk Dethleff, Peter Loewe, Dominik Weiel, Hartmut Nies, Gesa Kuhlmann, Christian Bahe and Gennady Tarasov.

Heft-Nr. 272/1998 – "FTIR-Emissionsspektroskopische Untersuchungen der arktischen Atmosphäre", von Edo Becker.

Heft-Nr. 273/1998 – "Sedimentation und Tektonik im Gebiet des Agulhas Rückens und des Agulhas Plateaus ('SETA-RAP')", von Gabriele Uenzelmann-Neben.

Heft-Nr. 274/1998 – "The Expedition ANTARKTIS XIV/2", by Gerhard Kattner.

Heft-Nr. 275/1998 – "Die Auswirkung der 'NorthEastWater'-Polynya auf die Sedimentation vor NO-Grönland und Untersuchungen zur Paläo-Ozeanographie seit dem Mittelwechsel", von Hanne Notholt.

Heft-Nr. 276/1998 – "Interpretation und Analyse von Potentialfelddaten im Weddellmeer, Antarktis: der Zerfall des Superkontinents Gondwana". von Michael Studinger.

Heft-Nr. 277/1998 – "Koordiniertes Programm Antarktisforschung". Berichtskolloquium im Rahmen des Koordinierten Programms "Antarktisforschung mit vergleichenden Untersuchungen in arktischen Eisgebieten", herausgegeben von Hubert Miller.

Heft-Nr. 278/1998 – "Messung stratosphärischer Spurengase über Ny-Ålesund, Spitzbergen, mit Hilfe eines bodengebundenen Mikrowellen-Radiometers", von Uwe Raffalski.

Heft-Nr. 279/1998 – "Arctic Paleo-River Discharge (APARD). A New Research Programme of the Arctic Ocean Science Board (AOSB)", edited by Ruediger Stein.

Heft-Nr. 280/1998 – "Fernerkundungs- und GIS-Studien in Nordostgrönland", von Friedrich Jung-Rothenhäusler.

Heft-Nr. 281/1998 – "Rekonstruktion der Oberflächenwassermassen der östlichen Laptevsee im Holozän anhand aquatischen Palynomorphen", von Martina Kunz-Pirrung.

Heft-Nr. 282/1998 – "Scavenging of ^{231}Pa and ^{230}Th in the South Atlantic: Implications for the use of the ^{231}Pa/^{230}Th ratio as a paleoproductivity proxy", by Hans-Jürgen Walter.

Heft-Nr. 283/1998 – "Sedimente im arktischen Meereis - Eintrag, Charakterisierung und Quantifizierung", von Frank Lindemann.

Heft-Nr. 284/1998 – "Langzeitanalyse der antarktischen Meereisbedeckung aus passiven Mikrowellendaten", von Christian H. Thomas.

Heft-Nr. 285/1998 – "Mechanismen und Grenzen der Temperaturanpassung beim Pierwurm *Arenicola marina* (L.)", von Angela Sommer.

Heft-Nr. 286/1998 – "Energieumsätze benthischer Filtrierer der Potter Cove (King George Island, Antarktis)", von Jens Kowalke.

Heft-Nr. 287/1998 – "Scientific Cooperation in the Russian Arctic: Research from the Barents Sea up to the Laptev Sea", edited by Eike Rachor.

Heft-Nr. 288/1998 – "Alfred Wegener. Kommentiertes Verzeichnis der schriftlichen Dokumente seines Lebens und Wirkens", von Ulrich Wutzke.

Heft-Nr. 289/1998 – "Retrieval of Atmospheric Water Vapor Content in Polar Regions Using Spaceborne Microwave Radiometry", by Jungang Miao.

* vergriffen / out of print.

** nur noch beim Autor / only from the author.